Proprioceptive Sensing for a Legged Robot

by

Pei-Chun Lin

A dissertation submitted in partial fulfillment
of the requirements for the degree of
Doctor of Philosophy
(Mechanical Engineering)
in The University of Michigan
2005

Doctoral Committee:
Professor Daniel E. Koditschek, Co-Chair
Assistant Professor Richard Brent Gillespie, Co-Chair
Research Professor Johann Borenstein
Associate Professor Arthur D. Kuo
Professor Mark R. Cutkosky, Stanford University

In memory of my grandmother

ACKNOWLEDGEMENTS

Time flies, doesn't it?

I can still clearly remember how nervous I was the day I arrived in the US to start this journey—an unforgettable experience filled with joys and tears. It is hard to believe that I have passed the tasks and reached the summit. This dissertation, the culmination of my years in graduate education, would not exist but for the support, encouragement, and contributions of many individuals.

I would first like to thank my advisor, Daniel Koditschek, for his continued guidance through this process. Over the years I have learned a great deal from him. Most importantly, he taught me how to think and deal with problems, both academic and nonacademic, from a broad perspective. I thank my co-advisor, Richard Brent Gillespie, for his valuable suggestions and ideas. He taught me how to widely utilize my knowledge of mechanical engineering, and to fuse it with new learning from electrical engineering and computer science. I also thank my committee for their input and advice. I admire their ability to understand my work quickly, point out essential problems precisely and to give excellent suggestions.

Working in Dan's group has been an intellectually rich experience, and I would especially like to thank Richard Groff and Haldun Komsuoglu for being great mentors—one brings me into the theoretical world of systems and the other guides me through various engineering tasks. I thank Joel Weingarten and Gabriel Lopes for many interesting discussions on research, and Greg Sharp for his help on the setup of the ground truth measurement system, one of the important tools utilized in my thesis work. I also thank Emilie Yane for proof reading my thesis.

I thank the staff of the ATL building for making everything run smoothly, especially Karen Alexa, Karen Coulter, Wendy Anderson, Cindy Watts and Kelly Cormier. I also thank Jim Berry for helping me solve various practical problems with his superior engineering skills.

I thank the many friends and colleagues who have helped make my time outside of lab a pleasure, Yi-Chung Tung, Sheng-Shian Li, Chih-Ting Lin, Meng-Ying Li, Hui-Ling Yen and Hsun-Hau Huang.

I thank my parents for their support on every decision I make and the life I choose, allowing me to be like a bird flying freely in the air. Most importantly, I owe my deepest gratitude to my wife Shu-Wen, who has accompanied me for 11 years and always shows her strong support no matter how difficult a situation we encounter. I feel so lucky to have such a wonderful lifetime parter. She is the love of my life.

TABLE OF CONTENTS

LIST OF TABLES

LIST OF FIGURES

Figure

LIST OF APPENDICES

APPENDIX

NOTATION

Fields

$\mathcal{D}$	Displacement field
$\mathcal{F}$	Force field
$\mathcal{S}$	Strain field
$\mathcal{E}$	Energy field

Mapping Functions ($\mathcal{M}$)

$\mathcal{M}_{SD}$	from strain field to displacement field
$\mathcal{M}_{SF}$	from strain field to force field
$\mathcal{M}_{DF}$	from displacement field to force field
$\mathcal{M}_{SD\_4Bar}$	from strain field to displacement field (specialized for the 4-bar leg on RHex)

Coordinate Frames / Planes

$\mathcal{W}$	World coordinate frame
$\mathcal{T}_i$	(i^{th}) Tripod coordinate frame
$\mathcal{B}$	Body coordinate frame
$\mathcal{C}$	Leg clamp coordinate frame
$\mathbf{w}_i$	Basis vectors of world coordinate frame
$\mathbf{t}_i$	Basis vectors of tripod coordinate frame
$\mathbf{b}_i$	Basis vectors of body coordinate frame
$\mathbf{p}_{\mathcal{B}}$	Coordinates of a point in body coordinate frame
$\mathbf{s}$	Coordinates of toe in body coordinate frame
$\mathcal{L}$	Leg motion plane
$\mathcal{P}$	Ground plane
$\mathcal{S}$	Support triangle plane on the ground plane, $\mathcal{P}$

State

r	General expression for displacement (scalar)
$\mathbf{r}$	General expression for displacement (vector)
ω	General expression for angular velocity (vector)
$\mathbf{a}$	General expression for linear acceleration (vector)
r_x	Center of mass displacement in lateral direction
r_y	Center of mass displacement in fore/aft direction
r_z	Center of mass displacement in vertical direction
α	Body orientation, pitch
β	Body orientation, roll
γ	Body orientation, yaw

Functions (f)

f_{RMSE}	Root mean squared error
f_{NRMSE}	Percentage root mean squared error
f_{ρ}	Coplanar measure
f_b	from leg strain to body pose (equal to $f_{bodypose}$)
f_a	from linear acceleration (12-axis accelerometer suite) to linear acceleration
f_r	from linear acceleration (12-axis accelerometer suite) to angular acceleration
f_w	from linear acceleration (12-axis accelerometer suite) to angular velocity
f_{gyro}	from gyroscope reading to angular velocity

Coordinate Transformations ($\mathcal{N}$)

$\mathcal{N}_{\mathcal{B}_i \mathcal{W}}$	Rigid transformation from body coordinate frame in the i$^{\text{th}}$ tripod stance to world coordinate frame
$\mathcal{N}_{\mathcal{B}_i \mathcal{T}_i}$	Rigid transformation from body coordinate frame to tripod coordinate frame in the i$^{\text{th}}$ tripod stance
$\mathcal{N}_{\mathcal{T}_i \mathcal{T}_j}$	Rigid transformation from i$^{\text{th}}$ tripod coordinate frame to j$^{\text{th}}$ tripod coordinate frame
$\mathcal{N}_{\mathcal{C}_i \mathcal{B}}$	Rigid transformation from i$^{\text{th}}$ leg clamp coordinate frame to body coordinate frame

Matrix Operations (M)

$\mathbf{M}_{\mathcal{B}_i\mathcal{W}}$	Rotation matrix from body coordinate frame in the i^{th} tripod stance to world coordinate frame
$\mathbf{M}_{\mathcal{B}\mathcal{T}}$	Rotation matrix from body coordinate frame to toe coordinate frame in the i^{th} tripod stance

(Extended) Kalman Filter

$\mathbf{x}$	State
$\mathbf{u}$	Input
$\mathbf{y}$	Output
$\mathbf{z}$	Sensor measurement
Φ	Linearized plant matrix
Γ	Linearized input matrix
$\mathbf{H}$	Linearized measurement matrix
$\mathbf{w}$	Plant noise
$\mathbf{v}$	Measurement noise
$\mathcal{E}$	Estimation
$\mathbf{Q}$	Model error covariance
$\mathbf{R}$	Measurement error covariance
$\mathbf{P}$	State error covariance
$\mathbf{K}$	Kalman gain
$\mathbf{J}$	Jacobian operator

Leg Modeling

M_l	Mass matrix
I_r	Inertia matrix
D_l	Damping matrix (linear state)
D_r	Damping matrix (rotational state)
K_l	Stiffness matrix (linear state)
K_r	Stiffness matrix (rotational state)
$\mathbf{f}_{l\_i}$	External force acting on the i^{th} M_l
τ_{r_i}	External torque acting on the i^{th} I_r
ϕ_e	Energy function
x_{l_i}	Leg state (displacement) on the i^{th} M_l
x_{o_i}	Leg state (orientation) on the i^{th} I_r

Leg Sensor

$\mathbf{f}_G$	Ground reaction force, equal to $\begin{bmatrix} f_n & f_f \end{bmatrix}^T$
f_n	Normal ground reaction force
f_f	Tangent ground reaction force (friction force)
f_{r_x}, f_{r_y}	Reaction forces from motor shaft
f_s	Static friction force
f_k	Kinetic friction force
τ_m	Motor torque
$\mathbf{d}_C$	Toe displacement in cartesian coordinate, equal to $\begin{bmatrix} d_y & d_z \end{bmatrix}^T$
$\mathbf{d}_P$	Toe displacement in polar coordinate, equal to $\begin{bmatrix} l & \phi \end{bmatrix}^T$
θ	Orientation of motor shaft
ϵ	Strain

Body Pose Computation

$\mathbf{e}_i$	Unit edge vectors in support triangle plane, $\mathcal{S}$
ν	Walking distance in a single trial
$\lvert\Delta\nu_l\rvert$	Error of walking distance in a single trial (sensory RHex)
$\lvert\Delta\nu_d\rvert$	Error of walking distance in a single trial (sensorless RHex)
$\lvert\Delta\nu_w\rvert$	Error of walking distance in a single trial (wheeled RHex)
κ	Percentage error of walking distance in a single trial

Miscellaneous

t	Time
Δt	Time difference
μ_s	Coefficient of static friction
μ_k	Coefficient of kinetic friction

ABSTRACT

This thesis provides a methodology of sensory system development for a hexapod robot, working toward the development of dynamic behaviors utilizing feedback controllers.

We develop an approach to utilizing strain gauges together with a simple data driven phenomenological model that simultaneously delivers information of leg touchdown, leg configuration, and ground reaction force suitable for robots with compliant legs. The strain gauges are implemented and models are constructed on two versions of RHex robot compliant legs. Leg configuration is further evaluated under realistic robot operating conditions by means of a high speed visual ground truth system.

We then introduce a continuous time 6 degree of freedom (DOF) body pose estimator for a walking hexapod robot. Our algorithm uses six leg configurations together with prior knowledge of the ground and robot kinematics to compute instantaneous estimates of the body pose. We implement this estimation procedure on RHex and evaluate the performance of this algorithm at widely varying body speeds and over dramatically different ground conditions by means of a 6 DOF vision-based ground truth measurement system (GTMS). We also compare the odometry performance to that of sensorless schemes—both legged as well as on a wheeled version of the robot—using GTMS measurements of traversed distance.

Finally, we report on a hybrid 12-dimensional full body state estimator for a jogging hexapod robot on level terrain with regularly alternating ground contact and aerial phases of motion. We use a repeating sequence of dynamical models switched in and out of an Extended Kalman Filter to fuse measurements from a body pose sensor and inertial sensors. Our inertial measurement unit supplements the traditionally paired 3-axis gyroscope/accelerometer with a set of three additional 3-axis accelerometer suites, thereby providing additional angular acceleration measurement (inertia torque), avoiding the need for localization of the accelerometer at the center of mass on the robot's body, and simplifying installation and calibration. We implement this estimation procedure offline, using data extracted from numerous repeated runs of RHex and evaluate its performance with reference to GTMS, also comparing the relative performance of different fusion approaches implemented via different model sequences.

CHAPTER 1

Introduction

It is both fascinating and instructive to study the evolution of earth's animals in response to the highly diversified and changing environment. Animals develop particular forms and mechanisms with high dynamical mobility in order to survive in their specific and localized habitats. Though each animal's appearance and behavior vary significantly, they share a similar fundamental "structure" comprised of myriad sensors and usually a smaller number of actuators—usually less than a couple hundred. Viewed at a very small scale, the environment is complex and changes rapidly over time, requiring animals to have enough sensors to acquire environmental information (visual, audio, smell, etc), to cope with their interaction with the environment (tactility, taste, etc), and to understand their own physical situation (balance, pain, etc). Viewed at a larger scale, the structure of the environment changes little over the span of an animal's lifetime, allowing for a fixed morphology (skeletal structure and actuators) to locomote over this environment.

The methodology of locomotion has a dramatic change with the advent of human civilization. During the last two centuries, humans have had the desire to increase their mobility (both manned and unmanned) by utilizing artificial devices. The major approach in human history to accomplish this goal is to "prepare" the environment by changing the landscape (usually by flattening it). For example, a car on a paved road, a train on railroad tracks, jeeps with improved mobility for off-road travel, and more recently, small wheeled robots in semi-structured environments. These wheel-based vehicles significantly enlarge the domain of locomotion for humans and are considered one of the major achievements of a five-thousand year civilization. In this case, sensors are much less important than actuators since the environment is made to be uniform, lowering the necessity of motion adjustment by sensory feedback control. However, it would be a difficult and endless task to "prepare" the whole environment since the geometrical surface of the earth is highly irregular and the terrain badly broken. Not to mention the possible future colonization of other planets which are also likely to have rough surfaces. One of the variants of a wheeled vehicle, capable of engaging rough terrain, is a track vehicle. However, its ability to traverse over broken terrain is still limited while its power consumption is comparably large to standard wheeled vehicles.

Apart from the challenge of developing devices with the ability to fly, a more generic approach one can chose to increase mobility is the design of artificial devices capable of traveling on rough and broken terrain, most likely, legged robots[1]. The best starting point lies in understanding how an animal locomotes [Muy57, DFF+00], since at this point we do not fully understand how to design complex actuation structures suitable for generalized locomotion. At the same time, we are also not at the point of being able to fully mimic animals to create "artificial animals". On the sensor side, current technology is not capable of delivering millions of reliable sensors in a compact package. On the actuator side, although we may be able to assemble hundreds of them to mimic animal shape[2], in general, the resulting robot does not have the same mobility since the power density of artificial devices is still much lower than that of animals. In addition, even if we accomplished both, integrating them to generate effective dynamic motion like animals is still an unsolved problem. More technically, unlike the wheel-based vehicles/robots that perform smoothly in plane motion (3 degree of freedom, DOF), the legged robots move in all 6 DOF in 3-D Euclidean space, thereby facing many more challenges of stability and dynamic-related issues. These challenges inevitably require a large set of sensors for feedback control in order to successfully behave dynamically in large domains. Section 2.1 briefly describes various methodologies used to approach the challenging problem of developing a legged robot with dynamical mobility.

1.1 Research Approaches to Legged Robot Design

The traditional approach to developing legged robots begins by mimicking live creatures like insects or mammals to construct the essential robot form as well as to design the basic moving mechanism[3]. As we have pointed out in the last section, the power density of commercially available actuators is still too low compared to what animals have. For this reason, in robot design the DOF of each leg is necessarily reduced to 3–5 in order to provide the simplest mobility, more specifically, walking without any dynamics[4] involved. In this approach the robot is designed to have a template[5] that can effectively be compared toto an animal with the tradeoff of limited mobility to quasi-static motion in the first stage of design, progressing toward dynamic locomotion once the technology provides better actuators and

[1]Hybrid leg-track or leg-wheel vehicles/robots [GBPB04] are other feasible solutions that try to utilize the advantages of both systems. In this approach, understanding subsystems is usually the first step toward a successful hybrid, which directly follows the necessity of exploring the leg system.

[2]For example, many current humanoid robots have comparable number of degree of freedom to humans

[3]Some exceptions are "legless" snake robots and worm robots which lie on a totally different region of (dynamical) locomotion.

[4]Dynamics indicates the existence of energy exchange between potential energy and kinetic energy during motion.

[5]A template is the simplest model (least number of variables and parameters) that exhibits a targeted behavior [FK99].

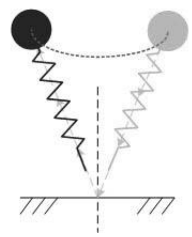

Figure 1.1: Spring-loaded inverted pendulum (SLIP)

better knowledge to design controllers for leg trajectories.

An alternative approach initiated around two decades ago focuses on utilizing simple mechanisms with extremely low DOF for each leg to construct reliable robots that may generate dynamic behaviors [Rai00]. In this approach, the robot is "anchored" with the simplest "template" which can, in principle, represent the original high DOF system with regard to motion [FK99]. For example, biological evidence shows that an animal running can be modeled as a spring-loaded inverted pendulum (SLIP) [FGM93, DFF^{+}00], shown in Figure 1.1. It directly follows from the "template" to represent the high DOF leg as a massless spring. As a result, utilizing compliant legs as passive springs to excite dynamic behaviors and to compensate insufficient active DOF on legs is widely adopted in robots following this approach. Additionally, low active DOF on each compliant leg results in low power consumption which helps in deploying simple control strategies. Thus making the robots autonomous and capable of performing dynamic behaviors—becoming "running robots", so to speak, standing as a milestone for exploring the dynamic robotics world. This approach uses simple dynamic systems on a robot platform, providing a chance to apply fundamental theory to practical implementation. The trade-off however, is that the behavior of a robot only matches a certain behavior of an animal based on the model we select, and is not able to represent the many behaviors that an animal might have. This indicates that different behaviors in animals may require the anchoring of different "templates", which further necessitates the design of different robots for different behaviors. It is only within this approach that we can fully explore the dynamic world from simple low DOF systems which we truly understand from a theoretical point of view with strong support from mathematics and physics. These systems will serve as the foundation for building high DOF dynamic systems in which we may be able to generate different behaviors based on different models with the same set of high DOF actuators. The long-term approach lies in understanding basic dynamic behaviors, designing feedback controllers, increasing the active DOF of the robots to generalize the internal mechanisms, and repeating this process until the system is capable of wide-range mobility.

We strongly believe that the correct approach to building highly mobile robots capable of locomoting like animals is to use simple and reliable mechanisms that are capable of exciting specific dynamic behaviors. The hexapod RHex, to be detailed in Section 2.2, serves as our first experimental platform to implement this idea. Using the knowledge and experience of dynamic systems gained from RHex, we might be able to build more complex platforms in the future.

1.2 Motivation

The hexapod RHex [BSK02] exhibits unprecedented mobility for a legged autonomous robot [SBK01]. Using an open loop feedforward control strategy, the machine runs at speeds exceeding five body lengths per second on even terrain [WLK04], and negotiates badly broken and unstable surfaces, as well as stairs [MCGB02, MMB01, CB03]. Initial empirical studies of controllers relying on cheap and inaccurate sensory feedback cues have resulted in significantly improved performance (inclinometers on slopes [KMS+01]; leg touchdown cues over broken terrain [WGK04]) and entirely new behaviors (body pitch sensitive accelerometers for flips [SRK04, SK02] and bipedal gaits [NB03]; leg touchdown cues for pronking gaits [MB01]).

Following this logic, a question arises: If more sensory feedback is available, can we further improve the current behaviors and/or be able to explore other behaviors? We believe that the answer is yes. One example follows the work of a previous lab member Dr. Saranli on theoretical considerations and simulation evidence of variable-speed dynamical running gaits [Sar02] which suggests that the availability of accurate full body state estimates as well as force interactions with the surrounding environment throughout the stance and aerial phases of locomotion should confer considerably greater agility. A controller for variable speed in wheeled vehicles is, in general, trivial—achieved by applying different voltage/current to the motor or air/fuel mixture to the internal combustion engine. However, it is a challenging problem for legged robots which use the energy exchange of the compliant legs to excite the continuous-time dynamic locomotion while maintaining full 6-dimensional stability. It becomes even harder for legged robots with high DOF rigid legs to apply large amounts of energy into motors to simulate spring effects due to the low power density of current commercial motors. In addition to the variable forward-speed controller, we explore the "legged-robot only" behavior—leaping, which requires sensory information to adjust the motion in order to maximize energy exchange in precise timing. These pieces of evidence and intuition together with the inspiration from animals motivate me to explore the problem of how to construct an appropriate sensory system for a legged robot.

The fundamental questions following this motivation lie on what kind of sensory information can be implemented on a robot, and which of them can be better used to improve the dynamic behaviors by sensory feedback—a problem we are interested in. We may search for a broad answer from the biological point of view by understanding what kind of sensing information animals have. The high-level conceptual answers define a subset of general animal sensory information, which includes environmental information (ground condition), interaction with environment (body/leg kinesthetics), and body status (body state, leg configuration, inertial force/torque) as we pointed out in the beginning of this chapter. On the other hand, we need also to complete the answer by considering the technological point of view, checking the feasibility of the implementation. For example, achieving a high-density micro force sensor array is not yet technological realizable reliably, due to limitation in manufacuaring at a nano or even micro scale; on the other hand, it is feasible to get linear velocity with a robot which animals cannot estimate. Thus, we aim to explore and implement the following sensing information for a legged robot:

- *leg configuration* — One of the important pieces of information regarding stability.
- *foot touchdown/ground reaction force* — Implementing pressure/force sensor arrays (kinesthetics) on the whole leg is difficult, but obtaining solo-contact foot information (touch, ground reaction) is feasible, and is sufficient for this primitive stage.
- *full body state* — Including 3 DOF center of mass (COM) displacement, 3 DOF body orientation and their derivatives (linear/angular velocity). Different behaviors may yield different approaches to algorithm development on the state estimation. In this thesis we will focus on the standard alternating tripod gait due to its familiarity and importance in hexapod robots.
- *body inertial force/torque* — These can be represented as a function of linear acceleration to the body mass and angular acceleration to the body inertia. Since the mass and inertia are usually constant, the required information is the 6 DOF linear/angular acceleration (assuming that the leg has small inertia so its motion does not affect the overall inertia).

1.3 Research Approach to Sensory System Design for a Hexapod Robot

Building a sensory system that can deliver the information described above at data rates relevant to motor control (~1kHz to preserve dynamic stability) remains a challenging problem in legged robotics due to the limitations of onboard instrumentation combined with extreme variations in operating regime. Moreover, since legged machines by definition spend a large fraction of their locomotion duty cycle in ground contact, the task of determining appropriate models is greatly complicated by the uncertainty of the ground conditions (local terrain shape, slipperiness, damping and compliance properties) and leg contact conditions (which legs are in stance).

The leg sensory system detailed in Chapter 3 provides the information of foot touchdown, leg configuration, and ground reaction force mentioned in Section 1.2. The generalized version of this problem can be described as how to measure the configuration and force/torque of a compliant member when it is under external loads on both ends. We adopt a novel approach to implement strain gauges together with assumptions of models that generate a direct kinematic mapping from localized strain information to the compliant member (leg) configuration and end-point force/torque (ground reaction force, motor torque) without involving dynamics. The foot touchdown/liftoff status can be easily delivered by comparing leg configuration to an empirical-set threshold. This methodology allows us to use a single set of sensors to deliver all of the desired leg information.

Intuitively, the knowledge of the configuration relative to the body of each leg in contact with the ground, together with information about the ground contact points yields complete pose information. By *pose*[6], we mean the full 6 DOF rigid body coordinates, 3 DOF describing the COM translation and 3 DOF describing the orientation of the body, relative to an inertial frame. In Chapter 4 we introduce a novel leg configuration-based full body pose estimator (hereafter referred to as the "leg pose sensor") for a hexapod robot in a tripod stance[7] with practical implementation on RHex. In that work we demonstrate that a memoryless transformation built from data driven phenomenological models relating leg strain to configuration together with a conventional kinematic model of leg configuration to body pose can accurately estimate body position and orientation when the robot's three non-collinear legs are fixed on the ground, i.e. in each tripod stance. In walking gaits with no aerial phase, the complete 6 DOF body pose in continuous time, also detailed in Chapter 4, can easily be extended from the above tripod-stance body pose from a purely kinematic model without velocity state estimation. The velocity state appears to be less important in this quasi-static walking locomotion.

In contrast, an alternating tripod runner experiencing significant aerial phases, with the concomitant touchdown/liftoff transients[8], would seem to require full body state estimation—both velocity and configuration information. In order to build the required estimator the sensor suite must incorporate enough information to allow the reconstruction of the full state from a record of past measurement attached to some dynamical model. During stance, complete 12 DOF continuous time body state estimates can be computed from the leg pose sensor by means of direct measurement and recourse to online differentiation. Absent of any other available sensors, these stance state estimates may be carried through the transient and flight phases only by the adoption of a particular dynamical prediction model. Although the leg pose sensor delivers accurate high bandwidth body pose estimates during stance (potentially marred by drift effects resulting from foot slippage detailed in Chap-

[6] 6 DOF body pose and their derivatives form a full 12 DOF body state.

[7] This term denotes the mode of leg contact wherein the three feet of the front and rear ipsilateral legs and the middle contralateral leg of a tripod are all in contact with the ground.

[8] Note that hexapedal running gaits need not entail an aerial phase to be "dynamical" in the sense of requiring careful management of kinetic energy to insure balance and steady progress [AMK+01]. However, RHex develops its greatest energy efficiency and highest speeds in gaits with long aerial phases. Hence, in this thesis, we focus our empirical tests on a "jogging" gait with an aerial phase exceeding 25% of the complete stride. By "touchdown" and "liftoff" transients, we refer to intermediate configurations where some number of legs fewer than three are in ground contact.

ter 4), overall performance throughout a complete stride is limited by inaccuracies in the transient phase models and the deleterious effects of online differentiation. In contrast, an inertial measurement unit (IMU), a popular sensor, continuously delivers derivative, typically translational/linear acceleration and rotational/angular velocity information over all phases of a stride. Saturation and drift effects[9] in the physical sensor can dramatically reduce the accuracy of the resulting integrated position estimates. The complimentary strengths and weaknesses of the leg pose sensor and IMU allow us to forge a better body state estimation than either one could achieve alone.

The traditional IMU (TIMU), comprised of 3 accelerometers for linear acceleration and 3 gyroscopes for angular velocity, hereafter abbreviated as "gyro", can readily provide full 12-DOF body state estimates when it is precisely located, carefully calibrated, and its output filtered appropriately[10]. Unlike the translational state components whose estimates require double integration of the accelerometer data, the rotational component estimates, requiring only a single integration step, might be expected to incur smaller errors. However, these available sensory sources do not adequately subserve estimation models that take second order dynamics into account. In the absence of angular acceleration measurements, the literature reveals a strong predilection for first order dynamics usually assuming constant velocity in preference to the direct differentiation that would otherwise be required without very accurate and formally observable dynamical models. Moreover, the general attitude toward contemporary cheap Micro-Electro-Mechanical System (MEMS) gyros suggests that their inferior drift and saturation properties relative to MEMS accelerometers may deteriorate any advantage at the signal processing stage. The considerable effort required to calibrate gyros detracts further from their inclusion in an IMU. Moreover, body inertia information promises to play an important role in the future implementation of more complicated models or feedback structures for dynamic running. Body inertia force can be directly retrieved from accelerometer information, while inertia torque requires the angular acceleration information usually derived from a bank of accelerometers with a dynamic equation. These facts all suggest the usage of angular acceleration data and angular velocity data, extracted if possible, from MEMS accelerometers for fusion. The falling cost and volume of MEMS-based accelerometers, together with the possibility of eliminating entirely the associated (theoretically innocent but pragmatically onerous) installation requirements motivates our introduction of a new 12-axis accelerometer suite to match the idea of an "advanced" IMU (AIMU) capable of delivering linear and angular acceleration as well as angular velocity detailed in Chapter 5. We will show that the 12-axis accelerometer suite

[9]The traditional navigation-grade IMU for rigid bodies in flight has good performance, but typically lies out of the range of robotics applications because of its cost and excessive volume.

[10]One of the strict constraint of utilizing traditional IMU to derive full body state is the requirement of installing the 3-axis accelerometer at the COM. If not satisfied, the COM acceleration will be a function of acceleration where the accelerometers are installed and a function of angular velocity and angular acceleration which is derived by the differentiation of angular velocity data. In this case, the noise floor of the COM acceleration data will strongly depend on the performance of both sensors and the differentiation process

is theoretically capable of these three states with no recourse to gyros, but is impractical in the present setting as a result of numerical ill-conditioning dependent upon the small baseline RHex's body affords. Therefore, in addition to the traditional 3-axis rate gyro, this 12-axis accelerometer comprises the advanced IMU that we add to our previous leg pose sensor to deliver full body state estimation in a hexapod robot with dynamical gaits detailed in Chapter 6.

Delivering reliable full body state estimation requires both good sensory information and appropriate models, which is even more of a challenge for the running locomotion that involves hybrid-model switching. Unfortunately, developing an effective approach to modeling a legged robot whose running gait is to be stabilized by state feedback estimates raises the prospect of entering upon a circular path with no clear starting point. For an n-legged machine there are 3^n possible formal Lagrangian models: touchdown-stick, touchdown-slip, and liftoff on each leg. These models include kinematic and dynamic properties of the legs whose small relative mass lends them at best negligible influence upon the body apart from the actuators' affects. Hence, the adoption of an appropriately abstracted (12 dimensional or lower) family of approximate models has strong appeal. Moreover, the approach to gait stabilization that we favor provides growing theoretical [Sar02] and empirical [SRK04] justification for the validity of these lower dimensional "template" control models. These abstracted models apply to the steady state conditions that emerge from well regulated gaits. Tractable feedback controllers that restore these gaits rely upon accurate estimates, while tractable filters based upon familiar dynamical models can be expected to yield accurate estimates only within well controlled gaits. For the present purposes of intelligent sensor development, we rely upon open loop stabilizing gaits developed by offline tuning experiments [WLK04] to bring the robot to a reliable steady state condition wherein familiar and tractable models can be readily implemented. Having established and verified the efficacy of these procedures for extracting reliable partial state estimates from the available sensor suite from Chapter 3 to Chapter 5, Chapter 6 mainly addresses the effect of sensory system to the state estimation with simple models. The support of leg pose sensor delivering displacement/orientation information renders the system observable, so the models only affect the duration of time for transients before it delivers the accurate estimates. However, the tradeoff to avoid the process of developing accurate models pays in the unavoidable time and effort to develop a totally different sensory suite (leg pose sensor). Therefore, in the meantime, we are also interested in exploring the alternate road—the possibility of good estimation by minimum sensory information using better models and algorithms. Section 6.5 introduces my collaborative work with Sarjoun Skaff and Alfred Rizzi at Carnegie Mellon University (CMU) on context-based state estimation based on standard Interacting Multiple Model (IMM) utilizing traditional IMU sensory information with additional "context" (information of leg touchdown or raw acceleration) to provide better estimation of timing to switch the models. Future research will combine the technology from both approaches and address the need and possibility for introducing more accurate physical models as well as switching between them as the leg contact conditions change during complex transients.

1.4 Contribution

This thesis develops a framework for what a sensory system in a hexapod robot should provide as feedback information, working toward the development of dynamic behaviors by feedback controllers.

This thesis details an approach to the implementation of strain gauges together with a simple data driven phenomenological model that simultaneously delivers information on leg touchdown, leg configuration, and ground reaction force suitable to general locomotion conditions like walking and running. This approach can also be utilized in the general problem of measuring the configuration and end force/torque of a compliant member when it is under an external load on both ends only.

We develop a novel leg-configuration-based within-stride full body pose estimator for a hexapod robot when the robot's three non-collinear feet are fixed on the ground, and also extend the algorithm for continuous-time full 6 DOF body pose estimation in walking gaits without aerial phases. We evaluate the performance of this algorithm at widely varying body speeds and over dramatically different ground conditions by means of a 6 DOF vision-based ground truth measurement system (GTMS), and also compare the odometry performance to that of sensorless schemes, both legged as well as on a wheeled version of the robot, using GTMS measurements of elapsed distance. The algorithm is quite generic and implementable on other robots since in principle it only requires sensory information of the kinematic relation between body coordinate system and a well defined foot coordinate system fixed in the world frame. For a robot with point foot contact (usually in quadrupeds, hexapods or others with a higher number of legs), this foot coordinate system can be established by 3 non-collinear feet on the ground. For a robot with areal foot (usually bipeds), this foot coordinate system can directly be defined on the foot pads. For typical robots with rigid legs, the kinematic relation between these two coordinate systems can easily be sensed by motor shaft encoders together with the physical dimensions of the links. For other robots with compliant legs like RHex, it becomes more challenging since we need encoder data together with the configuration of all sensible compliant members in order to obtain the foot coordinates with respect to the robot body, which we successfully demonstrate on RHex. This kind of leg configuration-based body pose sensor is extremely important and perfectly suitable for quasi-static climbing legged robots[11] since it not only relieves the concern about accumulation error due to foot slippage (assuming a rigid leg contact to the wall) but also reveals better performance than the IMU whose quality may be badly deteriorated by integration error in this vibration-rich climbing motion.

[11] In actuality, a "dynamic" climbing robot does not yet.

This thesis proposes a novel 12-axis accelerometer suite theoretically capable of delivering linear and angular acceleration as well as angular velocity (fulfilling the idea of "advanced inertial measurement unit (AIMU)") by using the kinematic relationships of rigid body motion without integration or differentiation. This suite provides additional angular acceleration measurement compared to the traditional inertial measurement unit (TIMU), avoids the need for gyros and for localization of the accelerometers at the center of mass on the robot's body, simplifies the installation and calibration. The partial state provided by the advanced IMU not only yields body inertia force/torque information but also delivers essential sensory feedback for full body state estimation when the robot operates in jogging/running gaits with aerial phases. The application of this 12-axis accelerometer suite is not limited in legged robots but can be deployed on mobile robots, vehicles, or other moving objects, especially suitable for a device with volume equal or greater than a cubic meter. One example of where developers have started to install inertial sensors in order to have better control is in automobiles. This design is also very useful in utilizing low-cost MEMS sensors as inertial sensors where the gyro is problematic in calibration and saturation.

We report on a hybrid 12-dimensional full body state estimator for a hexapod robot executing a jogging gait in steady state on level terrain with regularly alternating ground contact and aerial phases of motion. The algorithm uses a repeating sequence of continuous-time dynamical models that are interleaved in an Extended Kalman Filter (EKF) to fuse measurements from a novel leg pose sensor and an advanced inertial measurement unit comprised of a 12-axis accelerometer suite and a 3-axis gyro. This thesis implements this estimation procedure offline, using data extracted from numerous repeated runs of the hexapod robot RHex (bearing the appropriate sensor suite) we evaluate its performance with reference to a visual GTMS, comparing as well the relative performance of different fusion approaches implemented via different model sequences. The algorithm is generic and can be applied to a large number of settings in different levels based on the results gained from experiments. Generally speaking, for a multi-model hybrid system with or without specific model sequences, stable state estimation is achievable by utilizing simple models as long as some subsystems are observable and their time durations are long enough for the observer to converge and decrease the drift that happens in the remaining unobservable states. From a low level point of view, adopting this algorithm to other legged robots for body state estimation should be simple since it only requires an IMU and leg-configuration sensor whose requirements are detailed above, not tied to model selection for each mode since the models are motion and robot independent. For a biped, the approach is even simpler since it only has two modes, ground and aerial. From a higher level point of view, this methodology can also be applied to other kinds of sensor fusion in hybrid systems with mode-dependent sensory information.

1.5 Organization of Dissertation

Chapter 2 provides background knowledge to bridge the motivation and chosen approaches introduced in Chapter 1. Section 2.1 briefly reviews existing legged robots designed from both traditional and alternative approaches as described in Section 1.1, followed by a brief introduction to RHex and its specifications and behaviors. Section 2.3 reviews past work in related topics.

Chapter 3 introduces the general concept of leg sensory systems in a legged robot and demonstrates a set of specific applications utilized on the robot RHex. Section 3.1 introduces the information gained from each leg at a high concept level, followed by a brief summary of RHex's 4 different leg versions in Section 3.2. Section 3.3 illustrates the modeling framework of the compliant legs, followed by Section 3.4 showing the setup of an experimental table utilized to collect the required information for leg modeling. Section 3.5 introduces a specific setup to measure RHex's leg configuration in order to evaluate the performance of the modeling. Finally, Section 3.6 and Section 3.7 illustrate specific applications of the leg sensory system.

Chapter 4 introduces a computational algorithm for a within-stride and continuous-time body pose estimator for a hexapod robot utilizing the leg configuration sensor introduced in Chapter 3. Section 4.1 introduces the algorithm of body pose estimation, including within-stride body pose detailed in Section 4.1.1, odometry via sequential composition in Section 4.1.2, and a short discussion in Section 4.1.3. In Section 4.3 we evaluate the performance of this algorithm at widely varying body speeds in Section 4.3.1 and over dramatically different ground conditions in Section 4.3.2 by means of a 6 DOF vision-based GTMS detailed in Section 4.2. We also compare the odometry performance to that of sensorless schemes, both legged as well as on a wheeled version of the robot, using GTMS measurements of elapsed distance in Section 4.3.3, followed by a short discussion in Section 4.4.

Chapter 5 introduces a framework to construct an advanced inertial measurement unit delivering linear and angular acceleration as well as angular velocity by a novel 12 DOF accelerometer suite. Section 5.1 briefly reviews previous related work on angular acceleration measurements, followed by Section 5.2 that introduces a 3-dimensional coupled calibration which improves the accuracy of the measurement on practical implementation. Section 5.3 describes the methodology, characteristics, and initial experimental results of this 12 DOF accelerometer suite.

Chapter 6 introduces a hybrid 12-dimensional full body state estimator for a hexapod robot executing a dynamical gait in steady state on level terrain. Section 6.1 introduces some notation and illustrates the nature of the open loop stabilizing ("jogging") gait we will study subsequently. Section 6.2 summarizes the acquisition of partial state (body pose from leg pose sensor; linear and angular acceleration as well as angular velocity from advanced IMU) from raw sensor data. Section 6.3 describes the various dynamical models in each phase of a stride from which we construct statistical filters for full body state along with the details of how to fuse the two independent sensing sources (leg pose sensor and IMU), summarized in Section 6.2. Section 6.4 examines the accuracy of the resulting body state estimator implemented on RHex. Section 6.5 briefly introduces the context-based body state estimation[12] also for a hexapod robot executing a jogging gait in steady state on level terrain with regularly alternating ground contact and aerial phases of motion.

[12]In collaboration with Sarjoun Skaff and Alfred Rizzi at Carnegie Mellon University.

CHAPTER 2

Background

This chapter provides background knowledge to bridge the motivation introduced in Chapter 1 and my work in the following chapters. Section 2.1 briefly reviews existing legged robots designed from both traditional and alternative approaches as described in Section 1.1, followed by a brief introduction of RHex and its specifications and behaviors. Section 2.3 reviews past work in related topics.

2.1 A Brief Introduction to Legged Robots

The majority of the existing legged robots follow the traditional research approach introduced in Section 1.1 that use a higher DOF leg, and as a result, generally perform in quasi-static walking gaits due to power limitation and unclear control strategy. In the early 90's the AI Lab at MIT explored the idea of "robot insects", and two walking robots, Genghis [Bro89] and Hannibal [Ang91, Bre93] were built, each with 18 DOF in legs, as shown in Figure 2.1(a)(b). Dr. Quinn's group, Biologically Inspired Robotics Lab at Case Western Reserve University, has built a series of cockroach-inspired robots [QNB+03, QNB01a, QNB+01b, Tau00]. Robot III [NQ99, NQ98, NQB+97], with 24 DOF in legs, and robot V [KQR03], with 24 DOF in legs, are shown in Figure 2.1(c)(d). However, due to their low power density and complicated control structure, these robots can only perform "sit" and "stand" maneuvers, but do not walk. Forschungszentrum Informatik (FZI, Research and Information Center) in Germany has also built a series of robots following the same approach—Lauron I [BCI94], Lauron II [CBL97], with 18 DOF in legs, and the latest Lauron III [GSB01, GZZD05] which is equipped with multisensors for feedback walking, depicted in Figure 2.2(a). Other robots within this category are Hexapod [DN00], Figure 2.2(b), with 18 DOF in legs, from UIUC; octopod Scorpion [SK00, KLSK01], Figure 2.2(c), with 24 DOF total, from Institut Autonome Intelligente Systeme (AIS, institute of autonomous intelligent systems) in Germany; and octopod LobsterRobot [AWM+00, AWW+00], Figure 2.2(d), for underwater application from Northeastern University. Thanks to the availability of low-cost serve motors and controller

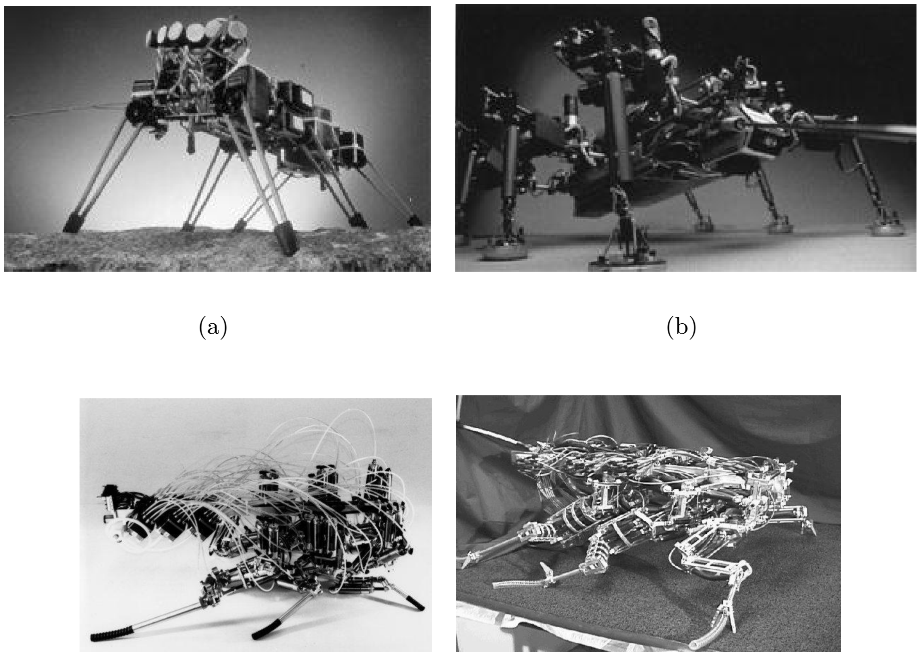

(a) (b)

(c) (d)

Figure 2.1: Photos of robots with high DOF legs: (a) Genghis from MIT; (b) Hannibal from MIT; (c) Robot III from CWRU; (d) Robot V from CWRU

chips, it is relatively easy to find hexapods being built by amateur robot hobbyists outside of those being built by academic institutions. Though they may not be professional enough to explore at high level research, most robots walk well by just simple sequential position control.

Dr. Raibert's group, Leg Lab at MIT, pioneered the alternative approach, also detailed in Section 1.1, by analyzing the dynamics of a simple hopper [Rai00] in the 80s. No actual autonomous multi-legged robot utilized this idea well until the mid 90's after Dr. Buehler's group, Ambulatory Robotics Lab at McGill University Canada, built the Scott series [SP04, PSB04, PB00, PSB03]. Scott I and Scott II are quadrupedal robots with only one active rotational DOF and one passive linear DOF in radial direction on each leg. Scott II shown in Figure 2.3(a) is the first robot capable of performing a dynamic gallop gait [SP04]. The hexapod RHex [SBK01] built in the collaboration of Dr. Koditschek's group at the University of Michigan, Dr. Buehler's group, and Dr. Rizzi's group at CMU is one of the most exciting robots in this field. It has only one active rotational DOF and 1–2 passive translational DOF depending on the type of legs. RHex, shown in Figure 2.3(b), referenced as one of the most versatile behavior excited by either openloop or feedback control, is also the experimental platform for my thesis work. Thus, detailed specifications will be introduced in Section 2.2. The Sprawl series [CKC04, CBC+02, KCC04] shown in Figure

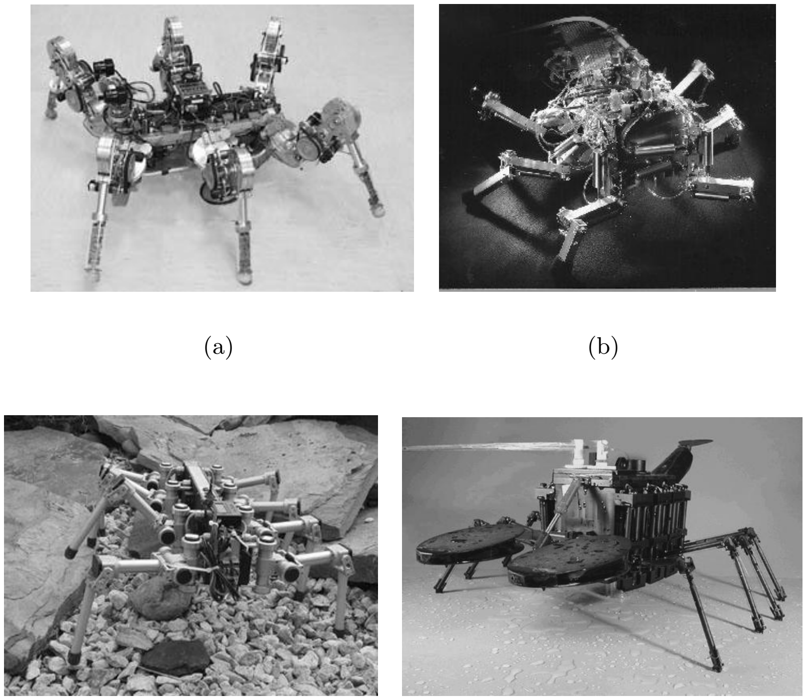

(a) (b)

(c) (d)

Figure 2.2: Photos of robots with high DOF legs: (a) Lauron II from FZI; (b) Hexapod from UIUC; (c) Scorpion from AIS; (d) LobsterRobot from NEU

2.3(c), built by Dr. Cutkosky's group, Dextrous Manipulation Lab at Stanford, has a similar hexapod form but with an opposite design strategy—one active translational DOF and one passive rotational DOF on each leg. The latest version of robot iSprawl [KCC04] performs the fastest running gait, 15-bodylength/sec, in the legged robot world. The quadrupedal robot Tekken series [FhKC03, KFK01, KAS99, ZFhK05, ZFhK04], shown in Figure 2.3(d), from Dr. Kimura's group in Japan utilizes the same idea to store and release spring energy for locomotion, but instead of exchanging spring energy through natural robot dynamics, it accomplishes that artificially by controlling the timing of windup and release leg springs. This mechanism combined with specific leg trajectory design yields a more elegant and natural looking locomotion. However, this reciprocal swing motion of the legs (continuous accelerate/deaccelerate motors) significantly increases the energy consumption as well as decrease the ability of overcoming obstacles. Dr. Waldron's group, Robotic Locomotion Lab at Stanford, also developed a quadrupedal robot Kolt shown in Figure 2.3(e) based on a similar windup/release spring idea, whose shape resembles the one legged hopper robot built at CMU [BZ98] shown in Figure 2.3(f).

Another approach taken by some researchers includes the combination of legs with other mechanisms like wheels or tracks. Dr. Quinn's group, Biologically Inspired Robotics Lab, at

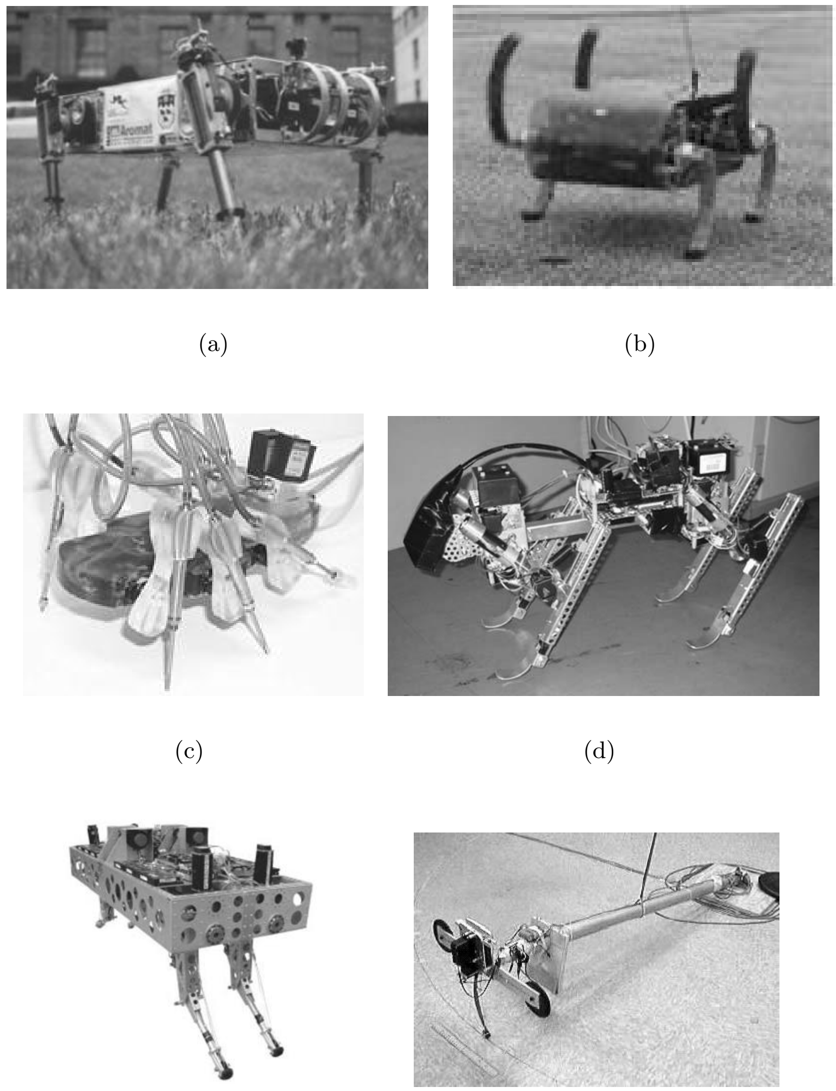

(a) (b)

(c) (d)

(e) (f)

Figure 2.3: Photos of robots with compliant legs: (a) Scott II from McGill; (b) RHex from the University of Michigan (standard version with half-circle legs); (c) Sprawlita from Stanford; (d) Tekken II from Kimura's group; (e) Kolt from Stanford; (f) One Leg Hopping Robot from CMU

Case Western Reserve University, also built a series of cockroach-inspired robots "Whegs" with simple rigid "legs" that combines the advantage of wheels and legs [LHQ05,QNB+01b], MiniWhegs shown in Figure 2.4(a). The robot uses "multilegs" to simulate the effect of wheels, increasing the mobility on flat terrain, and a discontinuous "wheel" that preserves the advantage of "legs" to overcome obstacles. These robots can move fast and pass broken terrain to a certain level; however, the motion is not dynamic and may not be able to

(a) (b)

Figure 2.4: Photos of robots with legs and wheels: (a) MiniWhegs from CWRU; (b) Hylos from Bidaud's group

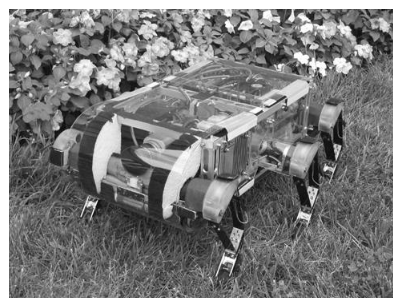

Figure 2.5: Rumba (RHex version 1.7) with the 4-bar legs equipped with strain-based leg configuration sensors (leg pose sensor) stands in a meadow

generate legged-creature-only motion like running, leaping or grasping. Dr. Bidaud's group, Laboratorie de Robotique de Paris at Universite Pierre et Marie Curie, developed a robot Hylos, shown in Figure 2.4(b), which has small wheels in the end of each legs. The "legs" in this robot merely act as the mechanism to adjust the relative locations between wheels and the body to maintain the balance (small pitch and roll angles) when the robot operates on the uneven terrain. Perhaps the more precise description of this robot is an enhanced wheeled robot.

2.2 A Brief Introduction to RHex

An introduction to the hexapod robot RHex [SBK01], shown in Figure 2.5, is presented in this section to give readers a better understanding about its construction, components, functionality, and behaviors. This is the platform I am currently working on.

- *Basic Specification* — Dimensions: 50cm (length) x 25cm (width) x 15cm (body height) or 25cm (total height when standing, body plus leg); weight: 8.5kg

- *Computation* — The main computation and control is run under customized RHex code written in the C++ language on the QNX 6.0 real time operation system (OS) in a "computer-like" PC104 stack (running industrial standard PC104+ bus) composed by a CPU board (Lippert Automationstechnik, Cool Runner, Pentium II 300MHz), an encoder board (Micro Computer System, MSIP400), a power board (Real Time Device, EPWR104), a PCMCIA adapter for wireless card (VersaLogic Corporation, PCM3115), and customized RHio board for RHex I/O interface. The computation for the vision system is operated in Linux on a second PC104 stack composed by a CPU board and a firewire board.

- *Actuation* — Designed for simplicity, the robot has only 1 active rotational DOF per leg driven by a DC brush motor (Maxon, RE-25, 20W) with gearbox (Maxon, GP-32C, ratio 1:33) and encoder (Maxon, HEDS 5540). It has 1 or 2 passive DOF per leg either by using compliant 4-bar legs or half-circle legs accordingly. The control signal sent from the RHio board goes through a motor drive board (MDB) to amplify the signal to the motors.

- *Sensing* — The standard version of RHex is equipped with the following sensors: a 3-axis optical rate gyro (Fizoptika, 941-3A), two 2-axis MEMS accelerometers (Analog Device, ADXL210) to construct 3-dimensional measurement along three principle axes, a firewire camera (SONY, DFW-X710), 6 encoders for motor position, 8 temperature sensors (monitoring temperature of 6 motors, heat sink on motor drive board, and body chamber), and sensors for voltage and current measurement. In order to proceed with my research, I also installed the following sensors in one of the robots, Rumba, shown in Figure 2.6: three 1-axis MEMS gyro (Analog Device, ADXRS300) to construct 3-dimensional measurement along three principle axes, eight 2-axis MEMS accelerometers (Analog Device, ADXL210) to construct 3-dimensional measurement along the three principle axes in four different locations of the robot's body, and 1 (for the 4-bar leg) or 2 (for the half-circle leg) strain gauges on each legs to acquire its configuration.

  Data from the MEMS sensors is acquired directly by another I/O board (Microsys, MPC550, 12bit per channel) through wires at the rate of 1KHz, the same as the main-loop computation. In contrast, RHex's freely rotating legs introduce a significant technical difficulty in taking measurements from any sensors installed on them—this is essentially a "remote sensing" problem. In our implementation, strain gauge measurements are transferred to the PC over a bi-directional wireless communication network, LegNet [Kom05], featuring a 50 Kbaud communication channel over a 916MHz carrier connecting a master located in the PC104 stack on the body to six self-contained microcontroller based slave units mounted on each leg. In this setting we achieve synchronous sampling of all strain gauges at 333Hz at a 6-bit resolution.

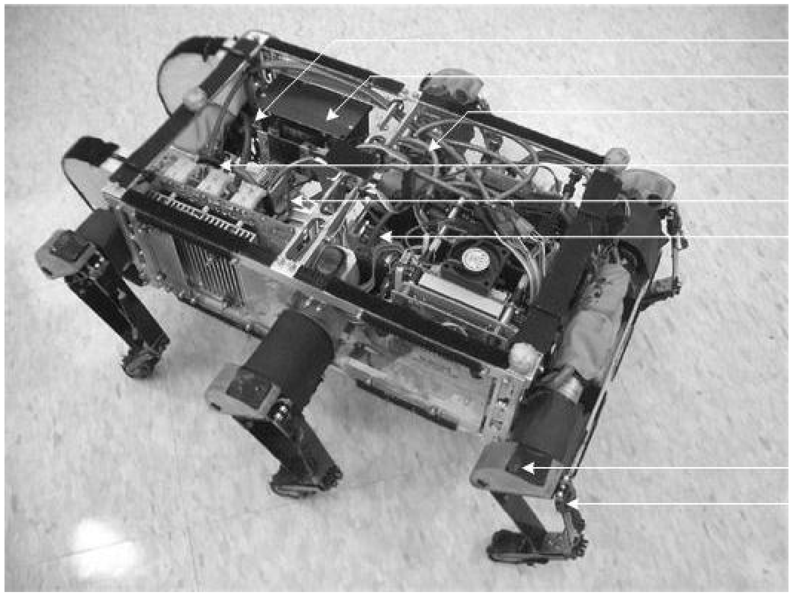

Figure 2.6: Photo of RHex with sensors, including four 3-axis MEMS accelerometer suites (form a 12-axis accelerometer suite), 3-axis optical gyro, 3-axis MEMS gyro, and a leg sensory system (strain gauges and LegNet on all legs).

- *User Interface* — A customized Graphic User Interface (GUI) runs on host laptops equipped with Linux OS, utilizing a joystick (Logitech, WingMan Cordless Rumblepad) to control the robot through a wireless network.

RHex, which is presently driven by task-level open loop controllers, performs extraordinarily mobility in different behaviors including:

- *Tripod Walking* no aerial phase
- *Tripod Jogging* [WLK04] with aerial phase, tuned for energy efficiency
- *Tripod Running* [WLK04] with aerial phase, tuned for maximum speed
- *Stair Climbing/Descent* [MCGB02, MMB01, CB03]
- *Hill Climbing*
- *Pipe Climbing*
- *Leaping*

RHex also performs the following behaviors with feedback controller:

- *Slope Climbing* [KMS+01] with accelerometer as inclinometer

- *Back Flip (Self-Right)* [SRK04, SK02] with partial state feedback provided by gyro
- *Bipedal Walking* [NB03] with partial state feedback provided by gyro
- *Pronking* [MB01] with foot touchdown sensing by motor current
- *Rough Terrain Passing (Coordination Controller)* [WGK04] with foot touchdown sensing by motor current
- *Bouncing* with foot touchdown sensing by motor current
- *Fly-by-Wire (Inertial-Assisted Navigation)* [SKMR03] with IMU
- *Vision-assisted Walking/Jogging* [SKMR03] with camera

2.3 Literature Review

The scope of this dissertation covers the design of a sensory system on a legged robot which provides the sensing information of leg status (foot touchdown, leg configuration and ground reaction force), inertia force and torque, and full body state when the robot operates in the quasi-static or dynamical gaits (walking or jogging) as detailed in Section 1.2. Therefore, the literature survey mainly involves research work related to the above topics[1].

The amount of available literature easily reveals the major trends in the robotics field and the problems people are interested in. It is without doubt that wheel-based robots strongly dominate robotic research. As a result, their development is further ahead of legged robots. Though some design principles may vary from wheel-based robots to legged robots, the literature regarding the development of wheel-based robots still offers a good reference and provides a guideline through this learning and comparison process.

The treatment of strain gauges as the sensing source to derive leg configuration or ground reaction force on the compliant legs detailed in Chapter 3 appears to be novel since no literature found regarding this issue. This is probably due to the fact that only few legged robot are designed with compliant legs for energy exchange, and even fewer of those have sensing capability on the legs. While strain is traditionally used for force [LDR+99, IH01] or torque [YIT03] measurement in the load cells, with the assumption of linear relation between strain on the designed local structure and the external force or torque, we explore the feasibility of utilizing local strains to represent overall configuration or end forces of a given massive structure (legs).

[1] We conducted systematic searches for *mobile/legged robot state estimation (estimator)*, *mobile/legged robot sensor fusion*, *mobile/legged robot odometry*, *mobile/legged robot pose (posture)*, *mobile/legged robot positioning/navigation/localization*, *mobile/legged robot inertia navigation*, robot leg sensor, Kalman Filter, *angular acceleration* across the standard bibliographic databases—Engineering Index (Compendex), IEEE Xplore, and ISI Web of Knowledge.

The localization, positioning and navigation problems have been treated extensively in the robotics society. For traditional wheeled robots, these problems concerning a "partial state," including COM displacement in horizontal plane and body yaw angle (here after referred as "localization" state), can be considered as a subset of our generalized description of full 12 DOF body state. In 1997 Dr. Borenstein published a survey paper [BEFW97] regarding available commercial sensors and up-to-date positioning techniques for mobile robots, including two major fields—relative positioning and absolute positioning. The former, usually implies odometry or inertial navigation [WT00, BS01, BDW95, Gre95]. The latter, usually combines the relative positioning technology to the sensor providing absolute locations by means of the so called "sensor fusion technology".

Odometry obtained by simply counting the motor shaft revolution by encoder is treated as the fundamental technology for positioning in wheeled robots; however, it is also notorious for its unbounded estimation error due to wheel slippage [Rud03, Mar02, BF96b, Mar01a]. Researchers try to reduce this error using approaches that include fusing with gyro [COB01, PCCL97, BF96a], providing environment map [HMA03, GMR01], or equipping the sensor capable of absolute positioning has global positioning system (GPS) [GRS99] or vision for landmark detection [BG01]). In contrast to the odometry whose accuracy depends on the ground condition, another relative positioning techniques utilizing inertial measurements are capable of representing true body pose as well as is extendable to other kinds of robots or vehicles. However, the same notorious drift problem exist due to integration error [SNDW00, NDW99b, MED98]. Thus, several approaches aimed to improve the estimation include using precise calibration and alignment [NDW99a, BhFDW95, LPP93, GHM91, DSNDW99], better choice of models (ground [JDW03, DSNDW01], underground [SDNDW99], underwater [GASH01], air [RH04, SGG$^+$00, KBI99]), and more generically, upgrading to absolute positioning by fusing with other sensors.

The idea of sensor fusion for state estimation has spread widely within the mobile robotics community, largely for application to wheeled vehicles addressing algorithm development, hybrid system [EAM01, DMC00], decentralized structure [NBDW99, BNDW98], multi-level fusion [RPS01], controller design [AA02], and some practical implementation [MSDW01, KZK97, AA02, PRS01]. Among all, the key component is the well-known linear filtering technology Kalman Filter [Kal60], the linear filter for prediction proposed by R. E. Kalman in 1960. Its unique structure helps to recover full state of the linear model by the correct weight ratio determined by noise of the model and the input from sensors based on some generic assumption. Over the decades researchers have evaluated its performance [RB02, RSB99], adopt this filter on different kinds of sensor fusion [FTPHBB00, SW99], and to improve the original algorithm (for example, to extend it to nonlinear systems [JU97, JUDW00]).

Recent and effective approaches to improving navigation accuracy in outdoor mobile robots or vehicles is the fusion of inertial measurement with GPS [ER02] data [PPU02, SNDW99, Kni97, MHJ94]. Utilizing such a low-cost positioning recalibration device, the requirement of inertial measurement unit decreases, resulting in wide spread model improvements [FT00b,FT00a,Wei96] and various applications (ground vehicles [Bev04,SW03, MV98], underwater vehicles [YBA+01,SHM97]). This challenge involves a series of unsolved problems such as selecting between a tight or loose fusion approach, choosing appropriate models for each sensor and for fusion, and synchronizing data. A similar situation occurs in the fusion of inertial measurements to vision data [Dez99, RV90, RJM02, LD98], the equivalent approach for indoor application[2].

Notwithstanding its importance for a more agile and responsive RHex [Sar02], we have been surprised to discover that there is no prior account of a complete body pose sensor in the legged robot literature. We have found literature about dead-reckoning error [MMAI01], positioning [OIYH98, SS01, KS92], and some prior work on exteroceptive vision based [Mar01b,LK03,BSW00,HKA97] approaches to positioning for legged machines. These algorithms, however, are specifically designed for their particular robots, which are not compatible with a general legged robot setting. We also found literature related to body orientation, and posture control for BIPED [Gor99], for quadruped [RI01, AH96], and for hexapod [FAH+95] orientation estimation aimed for a walking robot [RH00]. However, they are all focused on the foot force distribution or stability and balance by active feedback controllers. In addition, their algorithm are too specific to be generalized for other legged robots. Thus, our treatment of complete pose appears to be novel.

My work in Chapter 4 utilizing encoder data and leg configuration to obtain 6 DOF body pose can be treated as "odometry" for legged robots. The leg configuration data is necessary since the assumption of constant distance between ground and motor shaft varies in legged robots. In addition, the pattern to generate locomotion appears to be different as well. The accuracy of body pose estimation in localization states (COM displacement in the horizontal plane and body yaw angle) is determined by a foot slippage condition which requires further absolute positioning for long-distance locomotion, similar to the odometry in wheeled robots. The remaining three states, pitch, roll, and COM displacement in the vertical direction, here after referred as "stability" state, uniquely belong to legged robots, remaining bound and providing good high-frequency estimation.

Determining the relative pose of a manipulated object has won significant attention within robotic hand literature, especially for industrial autonomous robots, which yield various kinds of research on the problem of "grasping" for a robotic hand. For example, grasping irregular object after a simple detection scheme [LOS+00, KT94]; using haptic sensors to detect shape and hollowness of deformable objects [EETP99]; research on grasping policies by acquiring state [GJ02]; developing fingernail sensors to detect finger posture and shear force [MA01]. Considering a legged robot standing on the ground as a "ground

[2] Some sensors other than inertial measurement and GPS are also utilized in the navigation problem on mobile robots, like ultrasonic sensor [MAG+02], sonar [WC00], vision [BAL00, MKS99], angle measurement [HS96] and geometrical map [BA02].

grasping" problem becomes a much larger challenge since it strongly depends on the correct usage of gravity instead of the clamp force generated by an internal hand structure For that reason, there exists no literature on similar research for legged robots as of yet. Studies on ground force detection [NMK+02] or redistribution of ground force among robot legs [RI01, KIJ01] will serve as the basis of research in this direction.

While the localization, positioning or navigation problem addresses an important issue on wheel-based robots, that of legged robots reveals to be much more complex, not only because the motion expands from three to six dimensions, but also because the region of locomotion moves from quasi-static to dynamic[3]. The importance of the velocity state in legged robots during dynamic motion forces the estimation problem to expand into a 12 DOF body state, significantly more complicated than the typical 3 DOF state found in the wheel-based robots. In addition, it is also intuitively clear that full body state estimation on a legged robots will require certain sensor fusion techniques due to the wide range of dynamic motion over the limit that a single sensor can achieve. For this reason, few legged robots exist in the world, and even fewer of those are capable of dynamic locomotion. Of course, on some level, the fusion of IMU and the leg pose sensor is similar to some approaches used in wheel-based robots. For example, for localization states like COM displacement in the fore/aft and lateral directions together with yaw, our approach can be "morphed" as the fusion of IMU and "odometry" sensor, which incurs the threat of drift due to foot slippage. On the other hand, for stability states, pitch, roll, and COM displacement in the vertical direction, our approach is similar to the traditional use of vision or GPS to eliminate drift in the standard mobile robot fusion problem. However, there are important differences between these two "drift-reset" mechanisms: First, the leg pose sensor operates at sampling rates as high as those of the IMU, not like vision or GPS that have low update rates; second, the leg sensor provides higher accuracy estimates than differential GPS or vision can achieve. In summary, we find no prior statement nor solution of the problem posed by our work described in Chapter 6: the fusion of leg pose and IMU sensor data for a legged robot with dynamical gaits. In addition, including angular acceleration into the IMU for state estimation also appears to be novel.

We are not surprised that the derivation of angular acceleration [OV98] draws some attention in the robotic society, which has typically been detained mathematically from dynamic equations with linear acceleration measurement. The idea of an all-accelerometer IMU is directly followed since linear and angular acceleration, covers both translational and rotational space, can both be derived from accelerometers. This also yields the question of how many accelerometers are necessary. The standard approach of using 6 accelerometers yields unbound estimation error due to the possibly-drift integrated angular velocity appearing in the dynamic equations[4]. Hence, Dr. King [PKK75, MK79] introduced a novel

[3] In my opinion, it is this complex nature that makes working with legged robots far more interesting.

[4] Particular applications with small angular velocity may ignore its effect and simplify the dynamic equation [AKR03].

9-axis accelerometer suite delivering bounded linear and angular acceleration by eliminating the effect of the angular velocity by these 3 extra accelerometers. Unfortunately, this scheme requires that the accelerometer suite be very accurately installed at a specific spatial configuration, which significantly reduce the feasibility for a practical installation. Dr. Debra's group [CLD94, LH02, LL99] conducted a series of work on a 6-axis accelerometer suite that can deliver stable angular acceleration but with the tradeoff of losing stability on linear acceleration, since it becomes a function of unbounded angular velocity. Nevertheless, though we may save the cost of the accelerometers, if we only consider angular acceleration, this approach imposes a very strong constraint on the location and orientation of the 6 accelerometers yielding even lower feasibility for implementation [TPMV01]. Possibly eliminating entirely such theoretically innocent but pragmatically onerous requirement together with the falling cost and volume of MEMS-based accelerometers motivates our introduction of a 12-axis accelerometer suite detailed in Chapter 5 as an "advanced IMU" capable of delivering linear, angular acceleration and angular velocity.

CHAPTER 3

Leg Sensory System

This chapter introduces the general concept of the leg sensory system on a legged robot and specific applications utilized on the robot RHex. We implement strain gauges on the compliant parts of RHex's legs to detect leg touchdown/lift-off status and to estimate leg configuration and ground reaction forces. This methodology provides an unique approach to delivering multisensory information from a single sensing source that can be generalized to a family of legged robots with compliant legs.

Section 3.1 introduces the information gained from each leg in a high concept level, followed by a brief summary of RHex's 4 different leg versions in Section 3.2. Section 3.3 illustrates the modeling framework of compliant legs, followed by Section 3.4 showing the setup of an experimental apparatus utilized to collect required information for leg modeling. Section 3.5 introduces a specific setup to measure RHex's leg configuration in order to evaluate the performance of the modeling work. Finally, Section 3.6 and Section 3.7 illustrate the specific applications on the idea of the leg sensory system.

3.1 Information from the Leg

The first question that arises regarding a leg sensor at a conceptual level is "what kind of information we can get from leg," followed by, "which information is important for locomotion?" The answer can be categorized into the following three items:

- *tactility* — with simple capability to distinguish touch or no touch conditions or with more advanced capability to detect different force or pressure levels on the contact point or area. Large force or pressure on the leg typically indicates "ground contact" condition, which specializes the tactility information as *ground contact* and *ground reaction force.*

- *leg actuation force* — focusing on force generated internally as opposed to the previous item focusing on force interaction with surroundings. Theoretically, these two are not totally independent. This dependence is observed in the dynamic equations based on the physical system.

- *leg state* — including configuration and its derivative. Velocity state is comparably less important than configuration if the mass/inertia of the legs is considerably smaller than those at the body.

3.2 General Information about RHex's Legs

After learning what kind of information we can obtain from a leg, the second question is, "how to design a new leg with sensing capability or how to implement a sensor on the current available leg to obtain the desired information?" Instead of the top-down method of designing a new leg equipped with new sensing capability, we choose a bottom-up method of implementing sensors with desired sensing information and minimal modification to the currently available RHex legs. Our decision is based on the following two reasons: First, to prevent changing the leg characteristics, especially the property of spring stiffness, in order to preserve a similar dynamic response (which in turn maintains the robot's dynamic behavior). Second, to provide an opportunity to analyze the currently developed behaviors with sensory information from a leg.

Before delving further into this topic, we first provide some background information about RHex legs[1]. From the initial RHex version 0.2 to the latest version 1.7, RHex legs have progressed through four generations—delrin leg, hard 4-bar leg, soft 4-bar leg, and half-circle leg as shown in Figure 3.1. The main improvement from generation to generation is demonstrated through properties of compliance, reliability, and simplicity. The feature of compliance on legs acting as a passive spring is the key component for a robot to perform dynamic behavior, while reliability and simplicity are for practical issues of robot assembly and maintenance. The Delrin leg, composed of plastic delrin, a metal hip and a rubber foot, was discarded long ago because of its low compliance and fragility. Both the hard and soft 4-bar legs designs based on the Daniel straight-line mechanism can be treated as a passive 1 DOF system where the compliance is generated by the deformation of two fiberglass components on the internal 4-bar linkage mechanism. The only difference between these two designs is in the two joints close to the hip in the internal 4-bar linkage—fixed joints in the hard 4-bar and revolute joints in the soft 4-bar providing more motion flexibility. In the latter case, the lower natural frequency of the robot excited by the motor shaft rotation results in better dynamic locomotion. However, due to the complexity of assembly and fragility in the fiberglass component, the 4-bar leg was soon replaced by the current design of half-circle legs, which are composed of layers of fiberglass for compliance and bicycle tire tread for traction. From the geometrical view, the half-circle leg is intuitively modeled as the assembly of infinite torsional springs, each with an infinitesimal mass. This implies an infinite DOF system. Nevertheless, it can be treated as a 2 DOF system under reasonable

[1]General RHex information is detailed in Section 2.2.

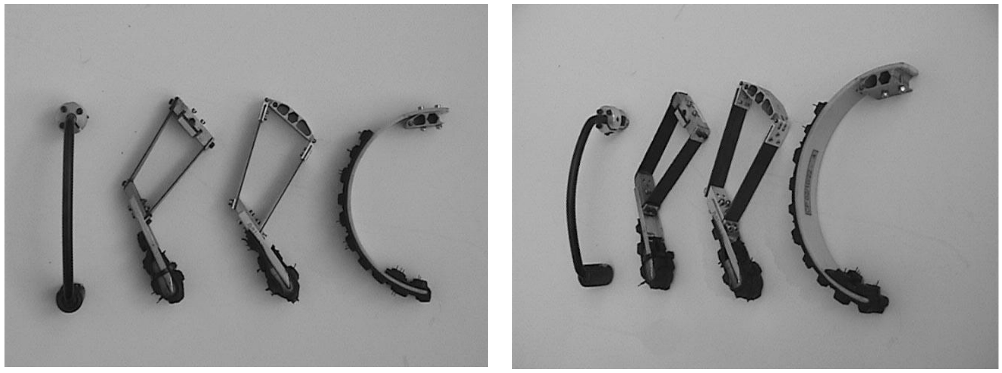

Figure 3.1: Four different kinds of legs of RHex: (a) front view; (b) tilt view; (i) delrin leg; (ii) hard 4-bar leg; (iii) soft 4-bar leg; (iv) half-circle leg

assumptions presented below. Though currently most researchers on the RHex project are operating the robot with half-circle legs, the soft 4-bar legs still play an important role due to its simple 1 DOF structure that results in easier modeling. Thus, both the soft 4-bar leg and the half-circle leg are used in development of the leg sensor. The following illustration focuses on the half-circle leg since it represents a more general case.

3.3 Concept of Leg Modeling

Understanding the desired leg information as well as the characteristics of RHex legs for sensory implementation, the next procedure identifies "what kind of sensor and with how much bandwidth for implementation." The answer, however, is not straight forward and strongly depends on how the legs are modeled, which is further dependent on the modeling assumptions based on objective physical specifications or subjective observations. Unlike simulation work, which requires modeling in a relatively high dimensional mathematical space to achieve excellent accuracy, the physical operational robot requires a relatively simpler model since it faces the tradeoff between limited signal bandwidth and desired signal resolution under available realtime online computer resources.

In order to find the "optimized" model suitable for sensory implementation and to discard minor issues in modeling, some assumptions are made as follows:

- *no mass on the leg* — The mass of the leg (4-bar leg: 100g; half-circle leg: 50g) is comparably small to that of the body ($\sim 8500g$). Centrifugal force and Coriolis force generated during leg rotation, due to small leg mass and inertia, are negligible at slow leg rotation speeds especially when the legs are on the ground.

- *no damping on the leg* — In the real world every mechanical system has damping[2]. However, we are inevitably forced to impose this unrealistic assumption based on the empirical difficulty of obtaining nonlinear coefficients of the damping model and measuring the velocity state online. The validity of this assumption will be checked in Section 3.7.2. The leg itself becomes an energy conservative system under this assumption.

- *infinite stiffness on the direction normal to the sagittal plane* — Legs are designed to allow deformation in the sagittal plane only. Note that in actuality, although the stiffness in the direction normal to the sagittal plane is not infinite, it is much larger compared to the two directions in the motion plane.

- *point contact to the ground by foot only* — Different contact points or multi-contact points on the leg result in different "effective" legs which require different mappings in each scenario. This assumption allows us to construct one "universal" model without dealing with multi-model switching. In real experiments, the robot operating in general walking and jogging gaits, with either the 4-bar leg or the half-circle leg, obeys this assumption well. However, we observe a large contact region from recorded videos by high speed cameras when the robot operates in high speed running gaits[3]. In this case, one extra contact sensor is necessary for detecting the contact point in order to perform multi-model switching.

Without loss of generality, the ideal half-circle leg shown in Figure 3.2(a) from a micro perspective can be sectionalized and modeled as the assembly of infinite equal-mass and inertia elements with equal-stiffness massless linear and torsional springs and equal-damping massless linear and torsional dampers in between as shown in Figure 3.2(b). Suppose there exist n small elements. Then this system has $6n$ DOF since each element has 3 DOF in displacement and 3 DOF in orientation. The springs and dampers connecting to both ends of each element, shown in detail in Figure 3.2(c), can be simplified by one pair of linear spring and damper passing through the COM of this element, as well as one pair of torsional spring and damper winding up through the COM. The general dynamic equations for each element:

$$
\begin{array}{lcccccc}
M_l \ddot{x_{l\_i}} & + & D_l(\dot{x_{l\_i}}, x_{l\_i}) & + & K_l(x_{l\_i}) & = & \mathbf{f}_{l\_i} \\
I_r \ddot{x_{o\_i}} & + & D_r(\dot{x_{o\_i}}, x_{o\_i}) & + & K_r(x_{o\_i}) & = & \tau_{r\_i} \\
\text{where} & & x_{l\_i} \in \mathbb{R}^3 & , & \mathbf{f}_{l\_i} \in \mathbb{R}^3 & & \\
 & & x_{o\_i} \in \mathbb{R}^3 & , & \tau_{r\_i} \in \mathbb{R}^3 & & \\
 & & i = 1, ..., n & & & &
\end{array}
\tag{3.1}
$$

[2]The existence of damping in the legs can be validated experimentally—after releasing the leg from a compressed configuration, we observe both the 4-bar leg and the half-circle leg are back to rest length after a few cycles of vibration. The stored potential energy is dissipated by damping in the leg.

[3]Only applicable when robot runs with the half-circle legs.

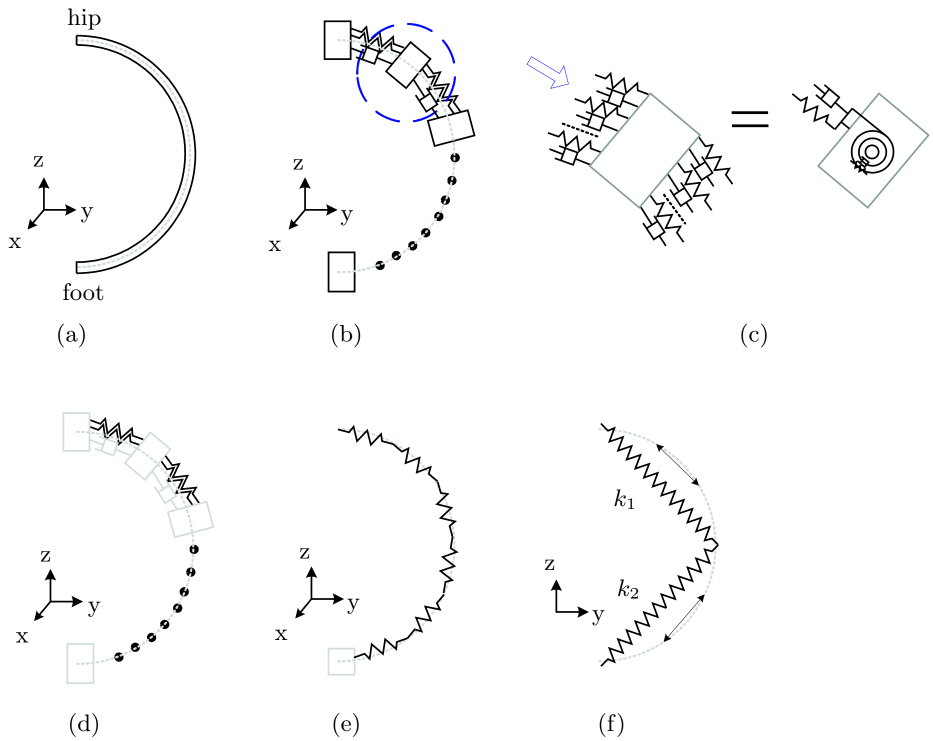

Figure 3.2: Sketch of the half-circle leg model: (a) sketch of the original leg; (b) physical leg model at a micro scale; (c) detail of each small element; (d) system without damper and mass; (e) equivalent system to (d); (f) final model displayed in a particular linear case

where M_l, D_l, K_l are a 3×3 matrix of leg mass, leg damping and leg stiffness; $\mathbf{f}_{l\_i}$ and τ_{r_i} are external forces and torque acting on the i^{th} object accordingly; x_{l_i} and x_{o_i} are the state of displacement and orientation of the i^{th} object accordingly.

Based on the assumption of no mass or inertia and no damping in the leg, this model can be simplified as an assembly of n linear springs shown in Figure 3.2(d) with $3n$ DOF, which can actually be treated as a large 3-dimensional linear spring shown in Figure 3.2(e) since the state between each pair of small springs is unimportant[4]. Adding the assumption of plane deformation, the leg becomes a 2 DOF system which can be conceptually represented in Figure 3.2(f) if the stiffness matrix is linear[5]. The original $6n$ DOF dynamic equation reduces to a 2 DOF kinematic equation, i.e. the spring stiffness model:

$$\begin{aligned} &K(x) = \mathbf{f}_{ext} \\ &\text{where } x \in \mathbb{R}^2, \mathbf{f}_{ext} \in \mathbb{R}^2. \end{aligned} \tag{3.2}$$

More specifically, consider a virtual clamp fixing the hip point. Then, x can be repre-

[4]This can be modeled as a 3 DOF torsional spring as well. There exists a fixed transformation between these two representations.

[5]Only a system with a linear stiffness matrix can be represented as two orthogonal linear springs, and the stiffness of these two springs are equal to the eigenvalues of the stiffness matrix. The matrix diagonalizing the stiffness matrix indicates the angles between current axes and the principle axes of the system.

sented as foot displacement in cartesian coordinate $\mathbf{d}_C$, including d_y and d_z; and $\mathbf{f}_{ext}$ can be represented as a ground reaction force $\mathbf{f}_G$, including normal force f_n, and friction force f_f. Equation (3.2) shows that one can find a direct map from leg configuration, $\mathbf{d}_C$, (in the displacement field $\mathcal{D}$) to the ground reaction force $\mathbf{f}_G$, (in the force field $\mathcal{F}$) without involving any other variables. This further suggests a quasi-static relationship—the work from all external forces and moments contributes to potential energy only, not to inertial and damping forces.

The resulting 2 DOF kinematic equation shown in (3.2) leads to the conclusion that *the half-circle leg can be well approximated as a 2 DOF system*, which further suggests sufficiency of two independent sensor channels measuring in either field, x or $\mathbf{f}_{ext}$, to recover both leg configuration and ground reaction force with known stiffness matrix, K. Following a similar logic, the 4-bar leg can be modeled as a 1 DOF system without any extra assumptions.

Combining the previous conclusion with the available information from the leg detailed in Section 3.1, we begin searching for a suitable sensor with 2 independent channels to derive the desired information. After surveying suitable commercial sensors in both displacement field and force field for installation with minimal modification on the current soft 4-bar leg and the half-circle leg, the strain gauge is the final selection because of its precise measurement of strain, compact package size, and easy installation. Though strain is categorized as a property of the displacement field, it is widely used as the basic component for most force sensors (load cell) on the market, by means of performing a precise linear mapping from the displacement field to the force field by a special design of the deformation mechanism under particular geometry shape. Therefore, in the first stage we believe that installing strain gauges with a precise known model allows us to extract correct leg information in both displacement and force fields. Theoretically, the number of independent-working strain gauges should be equal to the degree of freedom of leg for mapping and modeling work. Consequently, in our first experimental trial one and two strain gauges are installed on the soft 4-bar leg and the half-circular leg as shown in Figure 3.3.

Within two strain gauges, ϵ_1 and ϵ_2, installed on the half-circle leg shown in Figure 3.4(a), there exist three different fields for mapping and modeling—the force field $\mathcal{F}$; the displacement field $\mathcal{D}$; and the strain field $\mathcal{S}$. We are interested in three mappings: First, $\mathcal{M}_{SD} : \mathcal{S} \rightarrow \mathcal{D}$ shown in Figure 3.4(c); second $\mathcal{M}_{SF} : \mathcal{S} \rightarrow \mathcal{F}$ which relate the strain data to the leg configuration or foot displacement, d_y and d_z; and third, strain data to the ground reaction forces, f_f and f_n shown in Figure 3.4(d). Furthermore, inserting known ground reaction forces into three equilibrium equations within planar motion, two force equations and one moment equation shown in (3.3) yields the motor torque τ_m, along with the remaining two unknowns—reaction forces from motor shaft f_{r_y}, and f_{r_z} shown in Figure 3.4(d). The touchdown information can be derived simply by setting a threshold in either the configuration model or force model, or may be detected from raw strain output as shown in Figure 3.4(b). Thus, two strain gauges are sufficient to provide most of the

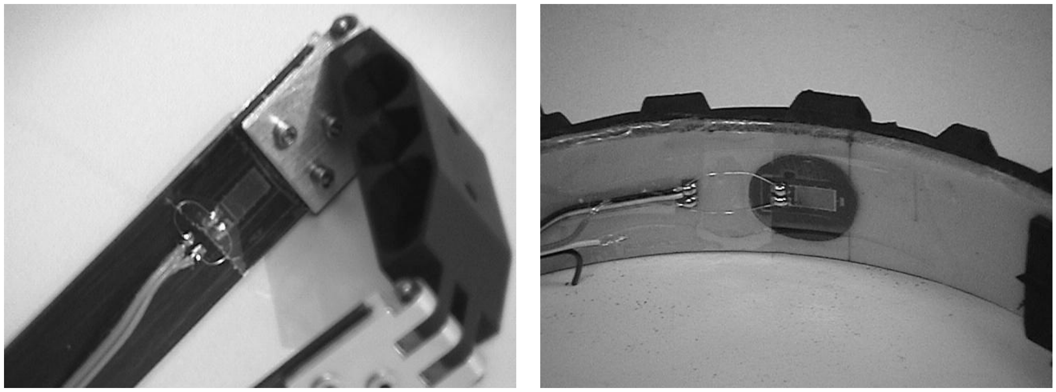

(a) (b)

Figure 3.3: Photos of the RHex legs with strain gauges: (a) 4-bar leg; (b) half-circle leg

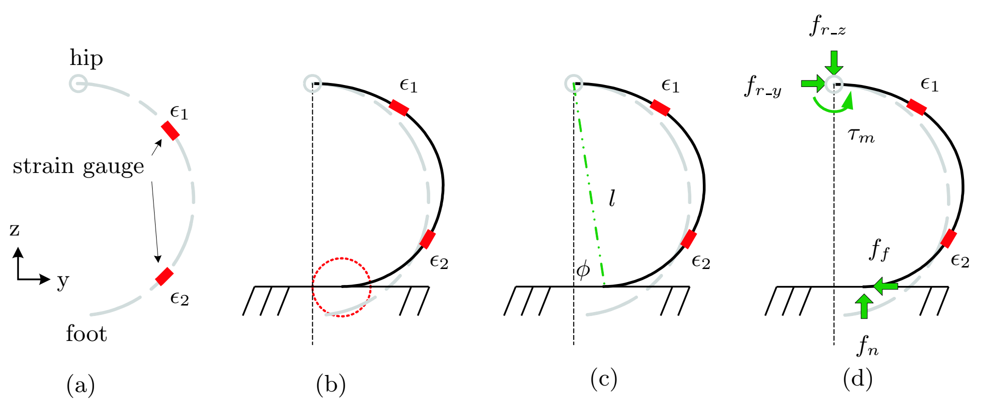

Figure 3.4: Available information on the half-circle leg with implementation of strain gauges: (a) leg at rest position with two strain gauges; (b) touchdown information; (c) leg configuration information; (d) ground reaction forces and motor torque information

desired information from the leg detailed in Section 3.1.

$$\sum F_y = 0; \sum F_z = 0; \sum M_o = 0 \tag{3.3}$$

$$\begin{bmatrix} d_y \\ d_z \end{bmatrix} = \mathcal{M}_{SD}(\begin{bmatrix} \epsilon_1 \\ \epsilon_2 \end{bmatrix}) \tag{3.4}$$

$$\begin{bmatrix} f_f \\ f_n \end{bmatrix} = \mathcal{M}_{SF}(\begin{bmatrix} \epsilon_1 \\ \epsilon_2 \end{bmatrix}) \tag{3.5}$$

For the 4-bar leg equipped with only one strain gauge, we are able to extract leg configuration but not ground reaction force and motor torque. One strain gauge can only provide one force data in the direction of leg compliance which is the resultant coupled force of normal and friction forces. Unable to decouple them, we also lose the ability to get further motor torque information. There is the option of designing another independent working small deformation area in order to install a second strain gauge. However, that would become a time-consuming subproject as well as defeat the goal of minimal modification. Consequently, touchdown and leg configuration are the only concern for the 4-bar leg at its current stage. The mapping $\mathcal{M}_{SD} : \mathcal{S} \to \mathcal{D}$ is similar to that of the half-circle leg but in 1 dimension.

This approach utilizes the leg as a pure input-output system, and during the model process we adopt a data driven model without exploring the analytical model of the system. The analytical model for the compliant members together with the free body diagram may also yield desired mapping; however, we prefer to use data-driven approach due to the following reasons: First, the compliant members made by fiber glass don't have properties of isentropic, especially for those custom-layered fiberglass, so we have a hard time to find a suitable analytical model for this case; second, it is still necessary to build a device to test the performance of this analytical model; thus, we prefer to directly use this device to find the data-driven model.

One of the direct applications of this kind of leg sensory system in a robot is ground compliance identification. During locomotion the pattern of the leg configuration or the ground reaction force is also affected by the ground compliance in addition to leg spring stiffness and body/leg mass. In this case we can expect different patterns of the leg configuration or the ground reaction force versus time, and these patterns can be recognized into different categories for identification. Appendix B describes some initial results in this research direction.

3.4 Benchtop Experimental Apparatus

A benchtop experimental apparatus [Lin05] shown in Figure 3.5 was utilized for collecting quasi-static leg data from various applied force, displacement and strain fields. This apparatus was built in order to perform modeling work on both RHex 4-bar and half-circle legs. Figure 3.6(a) sketches the kinematic parts of the apparatus. In this 2-dimensional setup, the "hip" of the leg is rigidly mounted at the origin of the setup, fixing both its position and orientation such that the polar coordinate clamp frame $\mathcal{C}$ coincides with the table plane, and at rest the foot vector points vertically downward. The virtual ground is a horizontal line passing through the foot which is attached to a foot clamp with free rotational motion. The foot clamp is mounted on a force sensor, which is secured on top of the linear slider mounted on the turntable. The foot can move freely in a 2 DOF polar coordinate frame centered at the origin. The position of the foot, $\mathbf{d}_P$, in the polar coordinate clamp frame $\mathcal{C}$, is measured by a linear potentiometer (Midori LP-50F) and a rotary potentiometer (Midori CPP-35B) along these two sliders. A 3-axis force sensor (Bokam

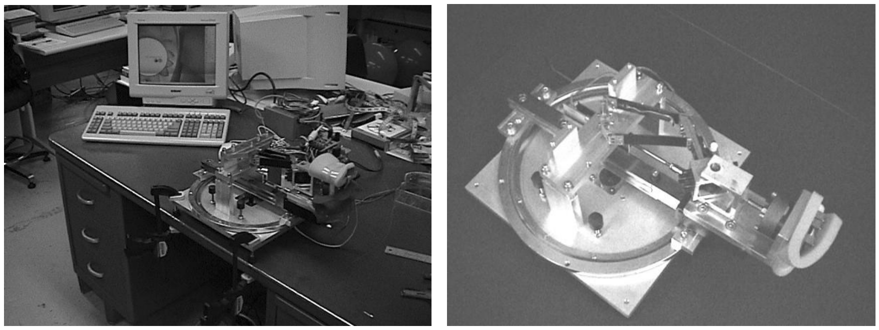

(a) (b)

Figure 3.5: Photos of benchtop experimental apparatus: (a) experiment area; (b) benchtop experimental apparatus

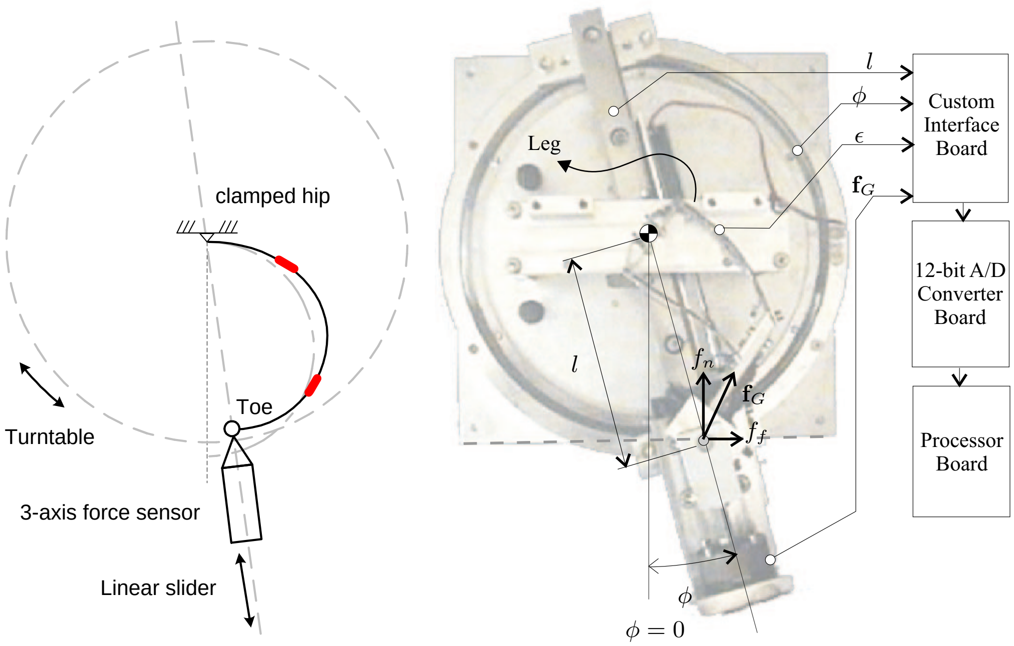

(a) (b)

Figure 3.6: Sketches of benchtop experimental apparatus: (a) kinematic diagram; (b) sensor signal flow

DX-480) measures the force at the foot simulating the ground reaction force $\mathbf{f}_G$. Figure 3.6(b) illustrates the leg configuration variables on the deformed leg attached to the setup, and on the right, a simple block diagram of the acquisition system is depicted.

Acquisition of the apparatus data is performed by a PC/104 stack containing: 1) Lippert Automationstechnik S-104P-CRR2-VEPS300 PC104 300 MHz CPU board with 256MB

RAM and 512MB compact flash running QNX6.0 real-time operation system; 2) Micro/Sys MPC550 12-bit AD converter board; 3) Real Time Device EPWR104-HR25, 25W PC104 5V/12V power supply; 4) VersaLogic PCM-3115 PC104 PCMCIA adapter with Avaya 128RC4 wireless Ethernet; and 5) a custom built interface board.

Sensors are sampled at 1KHz while the position of the foot is manually manipulated at slow speeds. Sensor data, including the strain of the leg after amplification by a Wheatstone Bridge, ϵ_1 and/or ϵ_2, measuring how much the leg deforms, the foot position in the clamp frame $\mathbf{d}_P \in \mathcal{C}$, and the force at the foot $\mathbf{f}_G \in \mathcal{C}$, simulating the ground reaction force acting on the foot, are filtered by a low pass filter with a cut-off frequency of 20Hz to eliminate high frequency sensor noise. The resultant data is stored in the on-board compact flash for off-line fitting studies.

3.5 High Speed Measurement of Leg Configuration

In order to evaluate the performance of the leg configuration model in real robot operation, we prepared an experimental "ground truth" measurement system utilizing a high speed camera to record kinematic configuration of the robot leg during realistic robot operating conditions.

Figure 3.7 illustrates the experimental setup where the robot walks along a 2×1 meter runway. A high speed black-and-white analog camera (RadLake HR-1000) is located 1 meter away from the path viewing the robot in the sagittal plane at 125 frames per second. In order to simplify offline analysis of the visual data, the runway and its background as well as the frame of robot are all covered with black mat card board. In these experiments we focused on the middle leg on the camera side which is instrumented with a LegNet LegModule providing strain gauge measurements at 6-bit resolution at 333Hz. Two reflective markers made by 3M tape are placed on the leg: 1) a 10×10 mm square reflective piece at the foot; and 2) a 100×10 mm rectangular piece extending from the hip attachment point towards the foot position in rest, pointing the rest configuration, $\phi = 0$. A low power halogen lamp is located near the camera to illuminate the scene. In order to synchronize the strain data collected on the robot with the visual data recorded by the camera, the robot is fitted with a set of LEDs that turn on when the strain logging is initiated on the robot.

An experiment starts with the robot placed at the beginning of the runway in standing pose ready to walk. Visual recording is initiated first followed by the activation of the logger on the robot. As soon as the LEDs on the robot indicate the start of the logging of strain, the user commands the robot to walk until it gets out of the camera view.

Recorded video is converted into a sequence of frames. Starting from the frame where the LEDs are on for the first time the frame sequence is fed to a MATLAB script. Each gray-scale frame is converted to black-and-white by setting a threshold and the objects in the image are distinguished from each other by using a connected components algorithm.

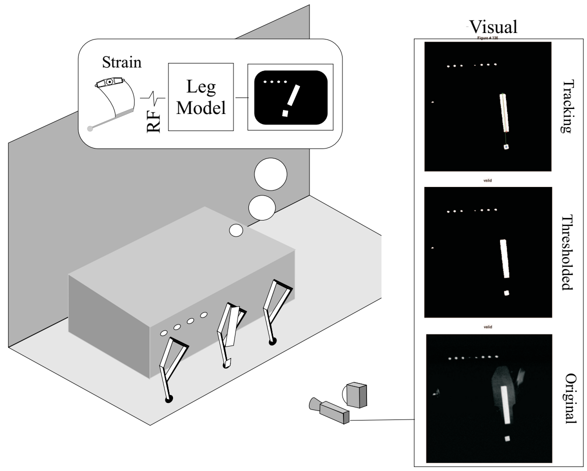

Figure 3.7: High speed sagittal plane ground truth experimental test station

The two markers, the foot and the ruler, are identified based on their geometric properties. The effective leg length, l, is the distance from the top of the ruler marker to the center of the foot marker and the deflection angle, ϕ, is the angle between the major axis of the ruler marker and the line connecting the top of the ruler to the center of the foot. These two variables represent the leg configuration in a polar coordinate system. Note that both the resulting visual measurements and the strain measurements recorded on the robot start at the same instant since they are synchronized by the activation of an LED.

3.6 4-Bar Leg Modeling and Evaluation

The 4-bar leg is chosen as our first trial for modeling and evaluation as well as testing the performance of the strain gauges due to its simple 1 DOF structure.

3.6.1 The 4-Bar Leg

The RHex soft 4-bar leg [Moo01] depicted in Figure 3.8 is a passive mechanical system composed of four parts: a hip clamp, front and rear compliant members, and a shin. The compliant members are thin rectangular fiberglass (S-glass[6]) strips that are rigidly fixed at one end to the shin and connected to the hip clamp at the opposite end by a revolute joint or hinge, creating a 4-bar linkage structure on a plane which will be referred to as the "leg plane" and denoted by $\mathcal{L} = \mathbb{R}^2$. The hip clamp rigidly attaches this leg structure to the hip motor shaft such that the shaft axis is normal to the leg plane $\mathcal{L}$, and goes through its origin.

In this particular arrangement the compliant parts are flexible in directions within the leg plane $\mathcal{L}$, but "infinitely" stiff in other directions for all practical purposes as our assump-

[6] Manufactured by Kinetic Composites, INC, http://www.kcinc.com/

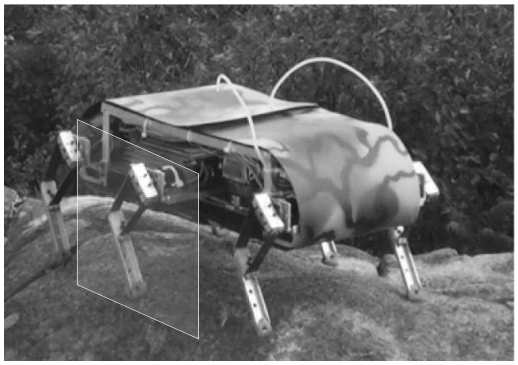

(a)

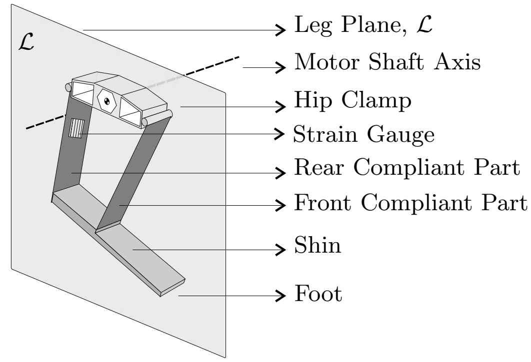

(b)

Figure 3.8: The 4-bar leg: (a) RHex with the 4-bar legs standing up in a natural setting; (b) key components of the 4-bar leg

tions. Combined with the constraints imposed by the closed chain mechanism the entire leg structure remains in the leg plane $\mathcal{L}$, for all times. Because the locus of physically valid leg configurations obtained empirically by the benchtop experimental apparatus detailed in Section 3.4 is a very thin set within the 2-dimensional leg plane $\mathcal{L}$, we have adopted the simplifying assumption that each leg is effectively a 1 DOF mechanism, and we develop a scalar nonlinear representation of the function relating strain to configuration accordingly.

We choose to utilize the strain across rear compliant part, $\epsilon \in \mathcal{S} := \mathbb{R}^+$, for computing the configuration of this 1 DOF leg. A strain gauge (Vishay EA-250BK-10C) is installed near the hinge connecting the rear compliant part to the hip clamp where the strain ϵ, is the smallest. In our empirical studies the maximum strain measured during tripod walking gait is approximately 1000 micro strain which falls within the 10^6 cycle at 1500 micro strain range reported in the strain gauge specifications[7].

3.6.2 Configuration Model

Figure 3.9 shows a kinematic sketch of the 4-bar leg mounted to a motor shaft on the body defined in body frame $\mathcal{B}$, as well as defines basic leg configuration variables. Let $\mathcal{C} := \mathbb{R}^+ \times S^1$ be a polar coordinate system in the leg plane $\mathcal{L}$, attached to the hip clamp, whose states are the distance between the hip attachment point and the foot, $l \in \mathbb{R}^+$, or "the effective leg length"; and the angular deflection from the rest position of the foot, $\phi \in S^1$, as depicted in Figure 3.9(b). Though these two variables seem to construct the 2 DOF polar coordinate centered at the hip, the actual foot locus depicted with a dashed line

[7]At a typical walking speed, the legs recirculate at roughly 2 Hz, hence we should expect mechanical sensor failures at a specified leg every 5 x 10^5 sec, hence, with six operating simultaneously, at some leg every 8 x 10^4 sec. Thus, at a typical a cruising speed of 1 m/s, we would expect to travel 80 km before suffering a leg sensor failure.

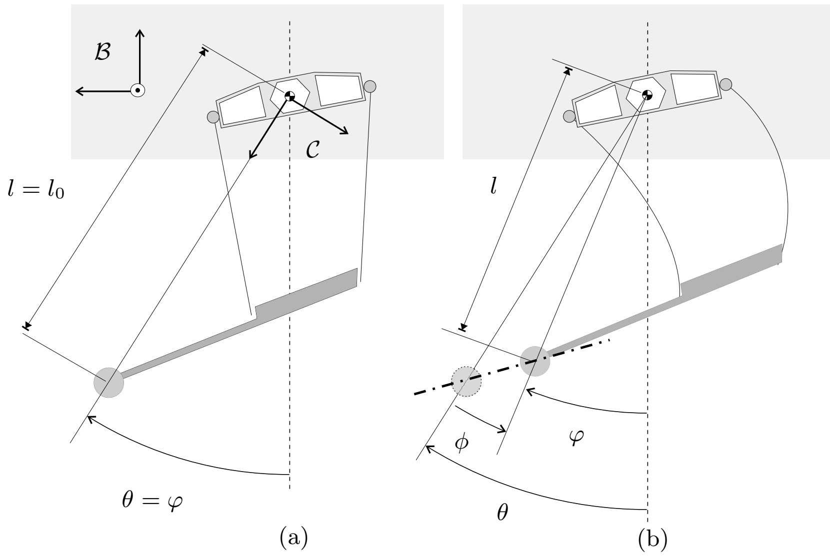

Figure 3.9: Kinematic sketches of the 4-bar leg: (a) at rest; (b) during compression

is an approximate 1 DOF curve. We introduce a memoryless system model for the 4-bar leg configuration relating the strain measurements across the rear compliant part, $\epsilon \in \mathcal{S}$, to the displacement of the foot with respect to the hip attachment point, $\mathbf{d}_P \in \mathcal{C}$, which is a representation of the leg configuration.

Considering a quasi-static setting we ignore damping and leg mass as in our assumptions detailed in Section 3.3 and model the 4-bar leg as a pure passive spring attached to the hip clamp with torsional and radial compliance. The locus of the physically valid foot positions for the 4-bar leg, presented in Section 3.6.3, lies in a very thin set suggesting a 1 DOF operating regime for this mechanism allowing us to represent the leg configuration $\mathbf{d}_P$, as a function of the scalar strain measurement, ϵ, given by a Taylor function, $\mathcal{M}_{SD\_4Bar} : \mathcal{S} \to \mathcal{C}$,

$$\mathbf{d}_P = \begin{bmatrix} l \\ \phi \end{bmatrix} = \mathcal{M}_{SD\_4Bar}(\epsilon) := \begin{bmatrix} \sum_{i=0}^{N} \left[p_i \epsilon^i \right] \\ \sum_{i=0}^{N} \left[q_i \epsilon^i \right] \end{bmatrix} \tag{3.6}$$

where the length coefficients, $\{p_i | i = 0, ..., N\}$, and deflection coefficients, $\{q_i | i = 0, ..., N\}$, are computed by the fitting studies detailed in Section 3.6.3.

3.6.3 Fitting Study

Before proceeding with the system identification computations it is necessary to clean up the raw benchtop data which is generated by manual manipulation of the 4-bar leg. Note that the resulting leg configurations at the sampling instants shown in Figure 3.10(a) are distributed unevenly over the leg plane, $\mathcal{L}$, where the axes of the plots are the cartesian displacement of the foot point, (d_y, d_z), from the rest position which is indicated by the

Table 3.1: Performance of the Polynomial Configuration Models of the 4-Bar Leg

	Model Fit		Cross Validation	
Order	$f_{NRMSE}(l, \hat{l})$	$f_{NRMSE}(\phi, \hat{\phi})$	$f_{NRMSE}(l, \hat{l})$	$f_{NRMSE}(\phi, \hat{\phi})$
1	1.12%	4.87%	1.20%	5.44%
2	1.11%	4.79%	1.16%	5.51%
3	1.05%	4.53%	1.11%	5.19%
4	1.05%	4.43%	1.11%	5.26%

solid dot. As a first step, we obtain a uniformly distributed set of data by averaging out the original raw data and resampling it over a uniform grid of points over the original region as seen in Figure 3.10(b).

The second step chooses "physically relevant" points from the uniform data that correspond to ground contact with no slippage characterized by two constraints: 1) positive normal component of ground reaction force, $f_n > 0$ with maximum allowable force threshold shown in Figure 3.10(c); and 2) friction force acting on the ground, tangent component of the ground reaction force, is less than the maximum static frictional force, $f_f < f_s$ shown in Figure 3.10(d). The maximum static frictional force is given by $f_s = \mu_s f_n$ where μ_s is the coefficient of static friction which is empirically measured to be 0.65 for the 4-bar legs over card board.

The coefficients of the leg model in (3.6) are computed by fitting the resulting physically relevant uniformly distributed data set shown in Figure 3.10(d) by a root mean squared (RMS) method. Letting $\hat{\mathbf{d}}$ denote the model prediction for a stream of N physical measurements, $\mathbf{d} = (d_1, ..., d_N)$, taken from a leg, where d_i denotes either length l_i, or deflection ϕ_i, we measure model performance by the percentage normalized RMS error, $f_{NRMSE}(\mathbf{d}, \hat{\mathbf{d}})$, between the original data, $\mathbf{d}$, and the corresponding model output, $\hat{\mathbf{d}}$, given by

$$f_{NRMSE}(\mathbf{d}, \hat{\mathbf{d}}) := \frac{1}{d_{\max}} \sqrt{(\left|\left|\mathbf{d} - \hat{\mathbf{d}}\right|\right|_2^2 / N)} \times 100 \tag{3.7}$$

where N is the length of the data vectors and $d_{\max}$ is the maximum value in original data.

Table 3.1 reports fitting and cross validation[8] performances by normalized RMS error for the leg model in (3.6) with different polynomial order, N. Small values indicate successful model prediction. Since the improvement in model performance is insignificant for quadratic and higher order polynomials, we choose to use the linear model due to its simplicity. Figure 3.11 presents the resulting linear fits for the leg length l, and deflection angle ϕ, respectively.

[8]This term denotes our simple estimates of the predictive accuracy of these models, as follows. In each data set we selected at random a small amount of data (typically 20% of the available input output pairs) for use as a cross validation test population. The models were fit to the 80% unselected population and then used to "predict" the input output relationships within the test population.

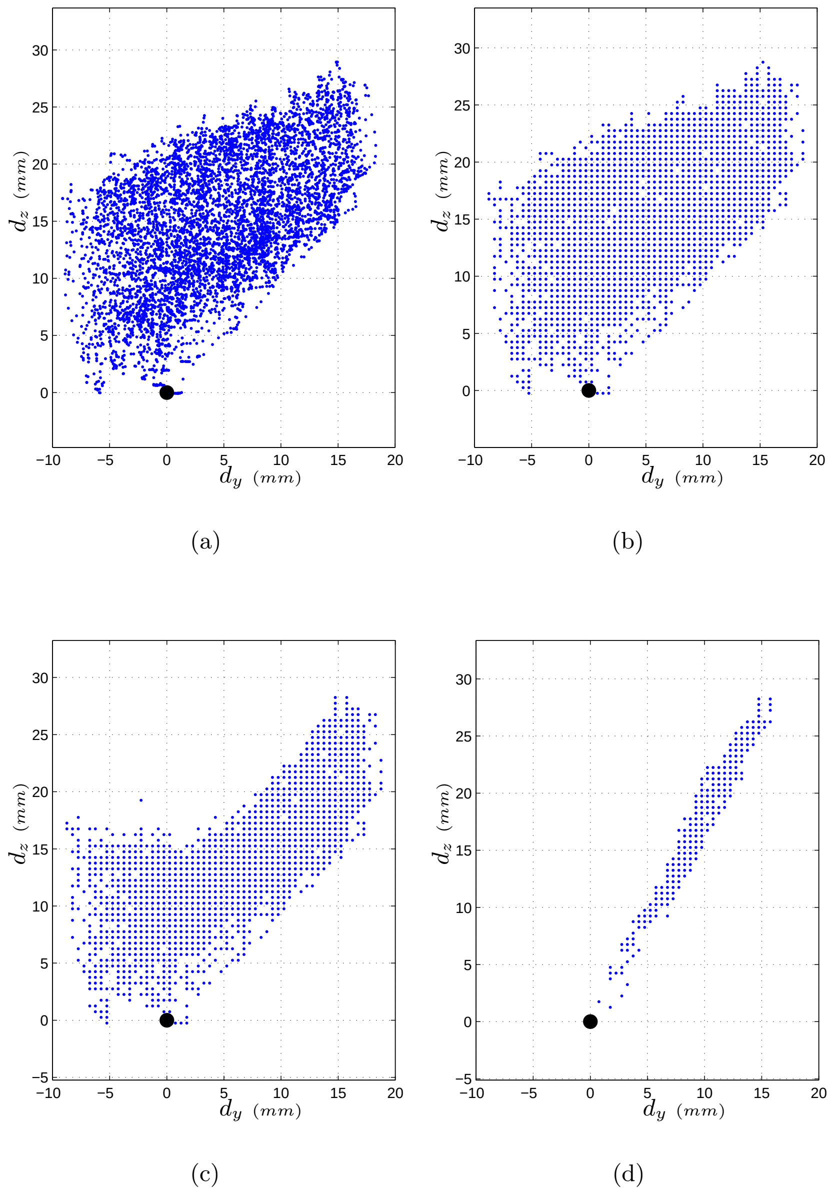

Figure 3.10: Scatter-plots of foot positions of the 4-bar leg: (a) raw data; (b) uniformly distributed data; (c) data with suitable normal ground reaction force; and (d) final physical relevant points

3.6.4 Evaluation of the Configuration Mode

In order to assess the performance of the kinematic leg model in (3.6) under realistic operating conditions we ran a set of experiments where the output of the model is compared against the leg configuration as measured by a visual test station described in Section 3.5.

Figure 3.12 shows plots of visually measured leg configuration states and the leg model output for five runs. The model performance evaluated by percentage RMS error for the

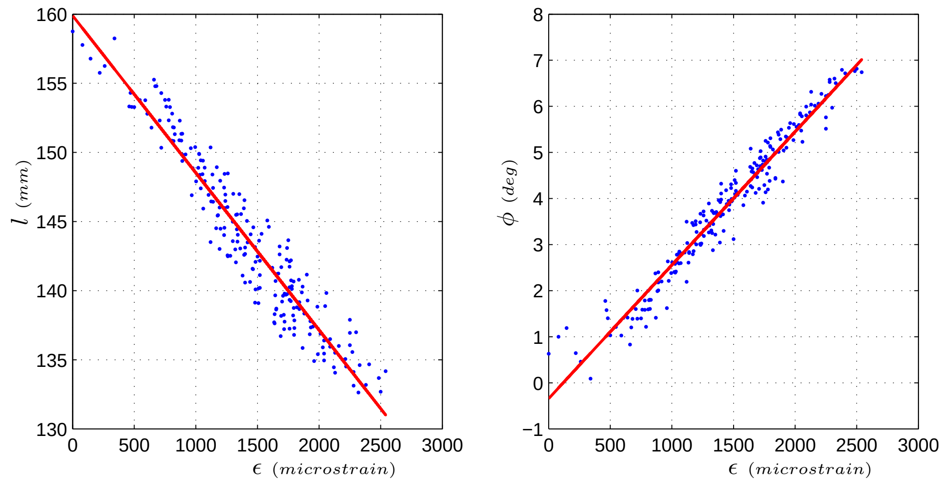

(a) (b)

Figure 3.11: Linear configuration model of the 4-bar leg: (a) leg length model; (b) leg deflection angle model with physically relevant data (unit: l cm ; ϕ deg ; "ϵ" unitless)

Table 3.2: Performance of Configuration Model of the 4-Bar Leg via Experimental Verification

Speed	0.2 m/sec		0.45 m/sec	
	$f_{NRMSE}(l,\hat{l})$	$f_{NRMSE}(\phi,\hat{\phi})$	$f_{NRMSE}(l,\hat{l})$	$f_{NRMSE}(\phi,\hat{\phi})$
Exp #1	1.29%	10.34%	1.25%	15.00%
Exp #2	1.19%	7.77%	1.11%	16.95%
Exp #3	1.29%	8.77%	1.12%	12.01%
Exp #4	1.14%	6.38%	1.11%	12.97%
Exp #5	1.29%	8.89%	1.23%	9.61%

same plots can be found in Table 3.2. We observe very small errors in effective length l, which remains less than 2% of the rest length independent of the walking speed. The deflection angle errors seems to grow as the speed increases with an apparent upper bound at 17%. Although the percentage error in deflection angle ϕ, is not small, its absolute value, below 5 degrees, turns out to have a negligible adverse effect upon the pose estimator, as reported in Chapter 4.

3.7 Half-Circle Leg Modeling and Evaluation

With the experience of a configuration model for the 4-bar leg, the half-circle leg is now investigated for its configuration model and ground reaction force model, which represents a more general leg sensory system.

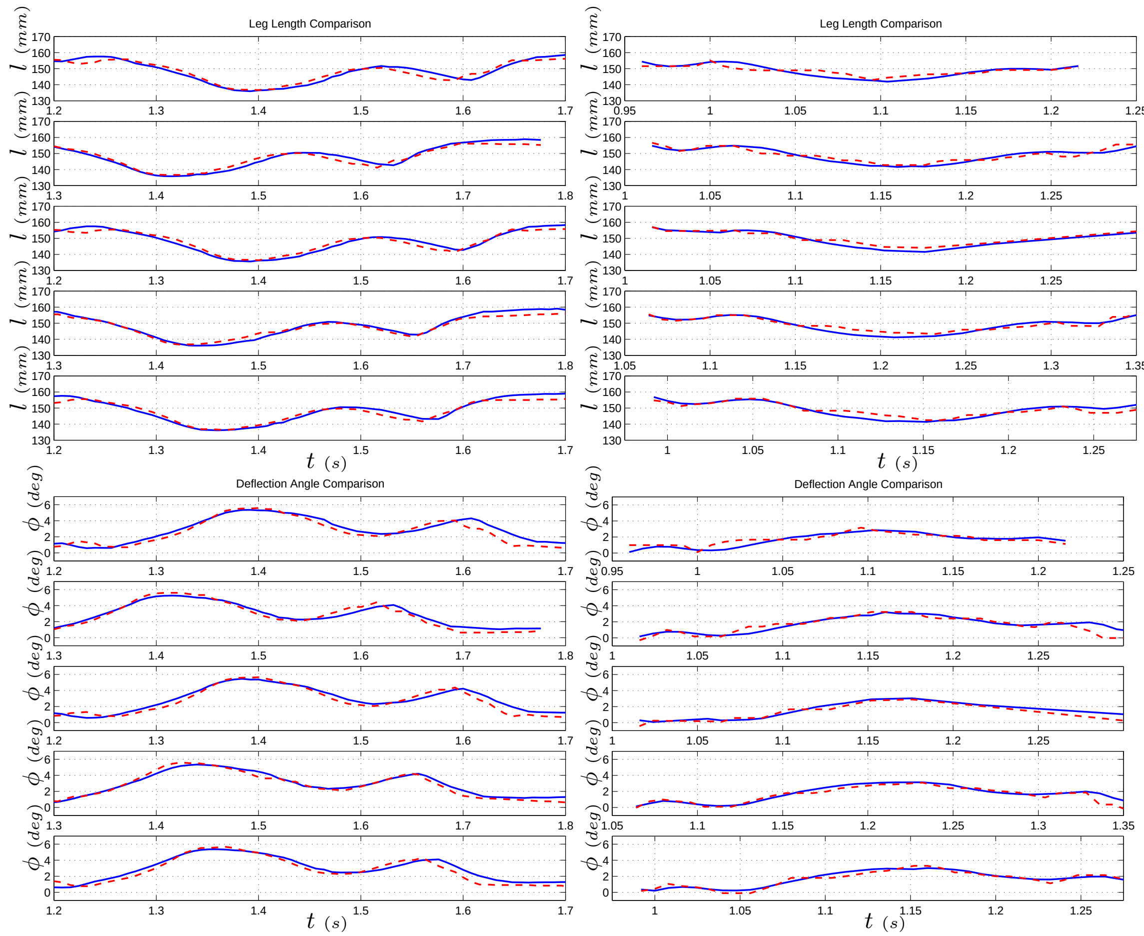

Figure 3.12: Plots of performance of 4-bar leg configuration model: comparison of visually measured (solid line) and leg model generated (dashed line) leg states at 0.2 m/sec (left) and 0.45 m/sec (right). Plots from five runs for the effective leg length l, (top) and deflection angle ϕ, (bottom) at provided. Rows are ordered according to the experiment number to match with Table 3.2. (unit: l cm ; ϕ deg ; t sec)

3.7.1 The Half-Circle Leg

Unlike the 4-bar leg's complex structure, the half-circle leg, a passive 2 DOF mechanical system, is composed of a hip clamp, a fiberglass leg and a section of bicycle tire tread. The simple design improves robustness of the leg during robot locomotion, and softer compliance in the legs results in the whole robot system performing closer to the natural frequency of the virtual "spring loaded inverted pendulum (SLIP)" resulting in a better tractable and dynamical behavior. However, this higher DOF system results in more complex modeling and requires more sensor channels installed on the leg to achieve the same task.

Following the terminology and concept from the 4-bar leg, the leg plane $\mathcal{L} = \mathbb{R}^2$ is also defined as the plane of 2 DOF motion, the sagittal plane. The hip clamp secures the leg structure to the hip motor shaft such that the shaft axis is normal to the leg plane $\mathcal{L}$, and goes through its origin. The displacement of the foot can be represented in cartesian coordinates $\mathbf{d}_C$, including d_y and d_x, as shown in (3.4); or in polar coordinates $\mathbf{d}_P$, including l and ϕ following the modeling concept from the 4-bar leg shown in (3.6)(a).

3.7.2 Internal Stiffness Model

Though the internal stiffness model, mapping from the displacement field to the force field $\mathcal{M}_{DF} : \mathcal{D} \rightarrow \mathcal{F}$ shown in (3.8), is not for sensory purposes like the other two mappings shown in (3.4) and (3.5). Instaed, it acts as a check point to evaluate whether the leg itself qualifies as an energy conservative system derived from energy potential in a specific operating region suitable for our case. This further determines the validity of our assumption of the leg being a 2 DOF system as detailed in Section 3.3. Therefore, it is worthwhile to evaluate the performance of this stiffness model before going deeper into the other two models related to the sensory system.

$$\begin{bmatrix} f_f \\ f_n \end{bmatrix} = \mathcal{M}_{DF}(\begin{bmatrix} d_y \\ d_z \end{bmatrix}) \tag{3.8}$$

Generally speaking, an energy conservative system can be described by a time-invariant potential energy function, $\phi_e \in \mathcal{E}$, in energy field, depending only on position x, and force $\mathbf{f}$, relating to energy function by

$$\mathbf{f} = -\nabla \phi_e \tag{3.9}$$

which indicates a coupling in parameters for systems greater than 1 DOF (Cauchy-Riemann Condition). Based on these characteristics, we can model the system with and without the constraints of this condition to check if the model performs similarly. If the result is positive, then the system is energy conservative.

Two-variable polynomial functions from order 2 to order 5 in energy space shown in (3.10) are chosen as the modeling function for the overall research of the half-circle leg for its simplicity, which is equivalent to the polynomial model from order 1 to order 4 in force space.

$$\begin{aligned}
\phi_{e_2_all} &= \sum_{i=0}^{2} \phi_{e_i} = \phi_{e_0} + \phi_{e_1} + \phi_{e_2} \\
\phi_{e_3_all} &= \sum_{i=0}^{3} \phi_{e_i} = \phi_{e_0} + \phi_{e_1} + \phi_{e_2} + \phi_{e_3} \\
\phi_{e_4_all} &= \sum_{i=0}^{4} \phi_{e_i} = \phi_{e_0} + \phi_{e_1} + \phi_{e_2} + \phi_{e_3} + \phi_{e_4} \\
\phi_{e_5_all} &= \sum_{i=0}^{5} \phi_{e_i} = \phi_{e_0} + \phi_{e_1} + \phi_{e_2} + \phi_{e_3} + \phi_{e_4} + \phi_{e_5}
\end{aligned} \tag{3.10}$$

where

$$
\begin{aligned}
\phi_{e\_0} &= k_0 \\
\phi_{e\_1} &= k_{11}x_1 + k_{12}x_2 \\
\phi_{e\_2} &= k_{21}{x_1}^2 + k_{22}{x_2}^2 + k_{23}x_1x_2 \\
\phi_{e\_3} &= k_{31}{x_1}^3 + k_{32}{x_2}^3 + k_{33}{x_1}^2x_2 + k_{34}x_1{x_2}^2 \\
\phi_{e\_4} &= k_{41}{x_1}^4 + k_{42}{x_2}^4 + k_{43}{x_1}^3x_2 + k_{44}x_1{x_2}^3 + k_{45}{x_1}^2{x_2}^2 \\
\phi_{e\_5} &= k_{51}{x_1}^5 + k_{52}{x_2}^5 + k_{53}{x_1}^4x_2 + k_{54}x_1{x_2}^4 + k_{55}{x_1}^3{x_2}^2 + k_{56}{x_1}^2{x_2}^3
\end{aligned}
\tag{3.11}
$$

where $[x_1x_2]^T$ is a 2-dimensional displacement vector, equal to $\begin{bmatrix} d_y & d_z \end{bmatrix}^T$ in cartesian coordinates or $\begin{bmatrix} l & \phi \end{bmatrix}^T$ in polar coordinates if specialized to the leg case. The constant term k_0 can be set to "0" since it represents the relative level of energy.

The stiffness mapping function $\mathcal{M}_{DF}$ in this specific case can be derived by applying (3.10) into (3.9). Below is an example of a mapping function in quadratic form from a 3rd order energy function:

$$
\begin{bmatrix} f_f \\ f_n \end{bmatrix} = \begin{bmatrix} k_{11} \\ k_{12} \end{bmatrix} + \begin{bmatrix} 2k_{21} & k_{23} \\ k_{23} & 2k_{22} \end{bmatrix} \begin{bmatrix} d_y \\ d_z \end{bmatrix} + \begin{bmatrix} 3k_{31} & k_{34} \\ k_{33} & 3k_{32} \end{bmatrix} \begin{bmatrix} {d_y}^2 \\ {d_z}^2 \end{bmatrix} + \begin{bmatrix} 2k_{33} \\ 2k_{34} \end{bmatrix} d_yd_z
$$

$$
\text{or, } \mathbf{f}_G = K_{Constant} + K_{Linear} \begin{bmatrix} d_y \\ d_z \end{bmatrix} + K_{Quadratic} \begin{bmatrix} {d_y}^2 \\ {d_z}^2 \end{bmatrix} + K_{QCouple}d_yd_z
\tag{3.12}
$$

where the coefficients k_{ij} in the matrices can be represented by "stiffness matrices" with different orders: $K_{Constant}$, K_{Linear}, $K_{Quadratic}$, and $K_{QCouple}$. Ideally, no constant term k_{11}, k_{12}, in the model should exist because no force exists when the leg is at "rest position" if the leg acts like a spring. However, in practical modeling work we preserve these constant terms to compensate the small inevitable toe clamping force when the leg is at rest position due to imperfect settings. From (3.12) it is easy to observe the existence of a relation between the parameters in the stiffness matrices, for example, the off-diagonal terms of K_{Linear} are equal. This is due to the assumption of the existing energy function which preserves the property of energy conservation. In the following modeling work we will compare the performance of this model to the "no-constraint" one which break any relation between parameters. For example, in the same quadratic force model, the no-constraint case will have 12 parameters, two in the constant term, four in the linear term, four in the quadratic term, and two in quadratic coupling term, compared to 9 in (3.12).

Table 3.3 shows the results of model performance under various assumed orders of the polynomials and various constraints in the parameters. The RMS error reduces as the order of the polynomial increases since the increase of the parameter space adds more room to adjust the model to the data. Small RMS error indicates that there indeed exists the two-to-two mapping between displacement field and force field, which further suggests the DOF of

Table 3.3: Performance of the Internal Stiffness Model for the Half-Circle Leg

Index	Model Type	L	LQ	LC	LQC	LQCQ
Model Root Mean Square Error						
(a)	Normal	0.8214	0.2951	0.3501	0.2529	0.2467
(b)	with Constant	0.8117	0.2777	0.3317	0.2463	0.2445
(c)	with Cauchy-Riemann	0.8501	0.3991	0.4189	0.3364	0.3091
(d)	with Constant Cauchy-Riemann	0.8120	0.3063	0.4005	0.2797	0.2771
Cross Evaluation Root Mean Square Error						
(a)	Normal	1.0024	0.3283	0.4135	0.2669	0.2676
(b)	with Constant	0.9866	0.3113	0.3940	0.2637	0.2668
(c)	with Cauchy-Riemann	1.0606	0.4269	0.4811	0.3502	0.3316
(d)	with Constant Cauchy-Riemann	0.9866	0.3424	0.4753	0.2952	0.2977

the half-circle leg is two. Comparing (b) and (d) to check the effect of the Cauchy-Riemann condition, small changes in RMS error indicate that the model itself satisfies the condition, which proves that the leg model can be approximated as an energy conservative system in our quasi-static operating region. As a result, we can ignore the damping effect on the leg modeling. In comparing (a) to (b) and (c) to (d), it is clear that the constant terms adjust the model to compensate the offset, a affine model, by the empirical clamping force error. However, small changes also indicate that the error due to clamping is minimal.

3.7.3 Configuration Model

The mathematical structure of the configuration model for the half-circle leg mapping from strain field to displacement field $\mathcal{M}_{SD} : \mathcal{S} \rightarrow \mathcal{D}$ shown in (3.13) is similar to that of the internal stiffness model shown in Section 3.7.2. Since the half-circle leg is a 2 DOF system, we use two strain gauges as input variables for the model mapping:

$$\begin{bmatrix} d_y \\ d_z \end{bmatrix} = \mathcal{M}_{SD}(\begin{bmatrix} \epsilon_1 \\ \epsilon_2 \end{bmatrix}) = \begin{bmatrix} f_{SD\_1}(\epsilon_1, \epsilon_2) \\ f_{SD\_2}(\epsilon_1, \epsilon_2) \end{bmatrix}. \tag{3.13}$$

The data fitting procedure is similar to that for the 4-bar leg detailed in Section 3.6.3; raw data is needed to be meshed into the uniform grid as well as to be filtered to physically relevant points shown in Figure 3.13. The distribution of the final physically relevant data points[9] indicates that the half-circle leg performs “wind-up” deformation during the robot locomotion, and this wind-up motion stores potential energy from displacements in both radial and tangential directions in the sagittal plane.

Performance of the polynomial models in different orders for estimating configuration from strain data of the half-circle leg is shown in Table 3.4. The suitable model to use is shown in (b) since: (1) Unlike the internal stiffness model derived from the energy function

[9]The leg orientation can be checked by the kinematic sketch of the benchtop experiment apparatus shown in Figure 3.6.

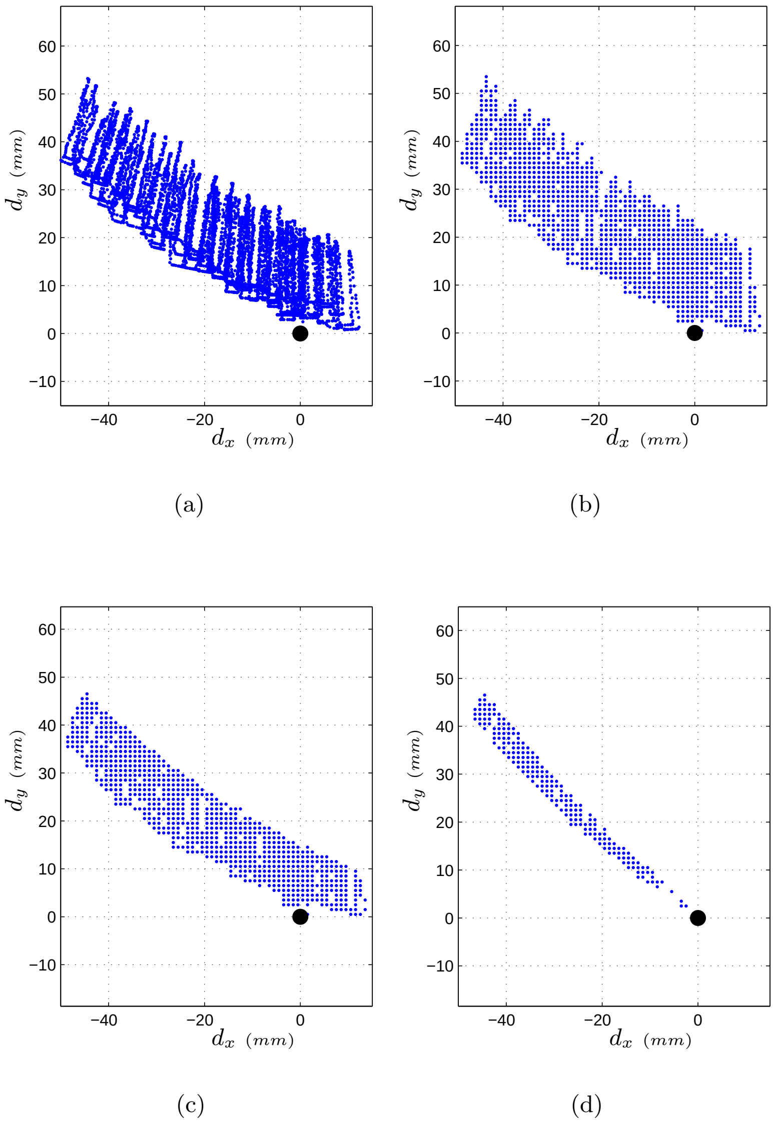

Figure 3.13: Scatter-plots of the foot positions of the half-circle leg: (a) raw data; (b) uniformly distributed data; (c) data with suitable normal ground reaction force; and (d) final physical relevant points (unit: mm)

resulting in the Cauchy-Riemann condition, this model has totally independent parameters. Rows (c) and (d) shows the effect of unsuitable constraints. (2) The output of strain gauges shows nonzero value in the natural leg configuration without deformation. Rows (a) and (c) shows the effect of the lack of the constant term. This table also indicates that the linear-quadratic (LQ) model yields a low RMS error in a minimal set of parameters and is the suitable model. Notice that the cross evaluation error on the LQ model is also less than 10%.

Table 3.4: Performance of the Polynomial Configuration Models for the Half-Circle Leg

Index	Model Type	L	LQ	LC	LQC	LQCQ
Model Root Mean Square Error						
(a)	Normal	5.9191	0.6868	0.8983	0.4168	0.3991
(b)	with Constant	1.0662	0.4196	0.4187	0.4150	0.3990
(c)	with Cauchy-Riemann	6.0134	1.0723	1.2067	0.8847	0.8722
(d)	with Constant Cauchy-Riemann	1.3604	0.9024	0.8855	0.8843	0.8709
Cross Evaluation Root Mean Square Error						
(a)	Normal	6.2299	0.7317	0.9745	0.4543	0.4906
(b)	with Constant	1.1853	0.4419	0.4549	0.4485	0.4909
(c)	with Cauchy-Riemann	6.3315	1.1411	1.3001	0.9313	0.9504
(d)	with Constant Cauchy-Riemann	1.5452	0.9427	0.9298	0.9302	0.9520

Another necessary step before importing the model into real robot operation is to check the independency of the variables. To this end, we use the Jacobian matrix of the model shown in (3.14) to construct a 2-norm condition number, the ratio of the largest singular value to the smallest one of the matrix. Large condition numbers indicate a nearly singular matrix, which also means non independency. Figure 3.14 shows the condition number over the whole domain, where the dash-dot line indicates the boundary of reasonable robot operation domain. A condition number ranging from 2 to 6 inside this domain indicates good independency in this LQ model.

$$Jacob(\epsilon_1, \epsilon_2) = \begin{bmatrix} \frac{f_{SD\_1}(\epsilon_1,\epsilon_2)}{\partial \epsilon_1} & \frac{f_{SD\_1}(\epsilon_1,\epsilon_2)}{\partial \epsilon_2} \\ \frac{f_{SD\_2}(\epsilon_1,\epsilon_2)}{\partial \epsilon_1} & \frac{f_{SD\_2}(\epsilon_1,\epsilon_2)}{\partial \epsilon_2} \end{bmatrix} \tag{3.14}$$

3.7.4 Ground Reaction Force Model

The procedure of the ground reaction force model for the half-circle leg mapping from strain space to force space $\mathcal{M}_{SF} : \mathcal{S} \rightarrow \mathcal{F}$ shown in (3.5) is similar to that of the configuration model detailed in Section 3.7.3. After the same data filtering process, the performance of the ground reaction force model is shown in Table 3.5, while the condition number with the robot operation domain is shown in Figure 3.15. From the table row (b), the LQ model is again the best fitting model. The condition number is also within the range of 2 to 6.

From intuition we may get the wrong impression that the requirement for a successful mapping from the strain field to the displacement field is less than that to the force field since strain and displacement are in the same “field”, though we use the similar simple model in both case. In truth, these two require the same strict assumptions detailed in Section 3.3. Strain measured from a strain gauge can be considered as a “localized displacement” at a specific point. The fundamental reason why we can use these two localized displacements to estimate the overall displacements is the existence of a spring effect on the whole leg, which mandatorily deforms the leg within a minimal energy requirement, also the “equilibrium”

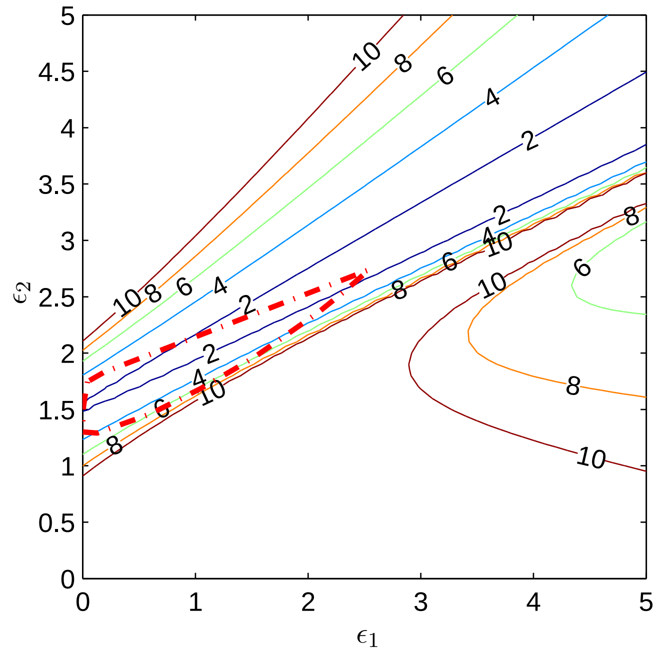

Figure 3.14: Condition number of the configuration model of the half-circle leg. The units of the axes "ϵ" are represented by voltage—larger voltage indicates smaller strain; nominal voltage located between $2.6 \sim 2.8$

Table 3.5: Performance of the Ground Reaction Force Models for the Half-Circle Leg

Index	Model Type	L	LQ	LC	LQC	LQCQ
Model Root Mean Square Error						
(a)	Normal	0.7689	0.0827	0.1077	0.0566	0.0561
(b)	with Constant	0.1022	0.0570	0.0570	0.0563	0.0561
(c)	with Cauchy-Riemann	1.0872	0.3427	0.3888	0.2868	0.2852
(d)	with Constant Cauchy-Riemann	0.2940	0.2882	0.2866	0.2856	0.2850
Cross Evaluation Root Mean Square Error						
(a)	Normal	0.8001	0.1051	0.1347	0.0694	0.0694
(b)	with Constant	0.1272	0.0688	0.0699	0.0704	0.0692
(c)	with Cauchy-Riemann	1.1932	0.3851	0.4552	0.29200	0.2907
(d)	with Constant Cauchy-Riemann	0.3036	0.2953	0.2944	0.2918	0.2899

state. Without the spring effect, there is an infinite number of deformed configurations within a given specific foot displacement. For example, suppose the leg is made of a section of bike chain—fixing the relative location of both ends does not give any information about the configuration of the middle chains. On the other hand, knowing the relationship between two randomly chosen links does not reveal any information about the relative locations of the end points. However, this spring effect not only relates the displacement to the force but also brings the damping effect and inertia into consideration based on the principle of

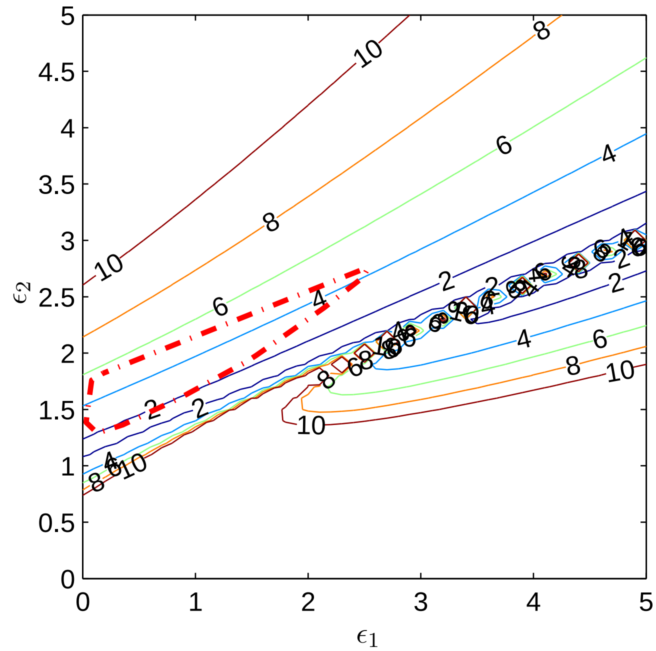

Figure 3.15: Condition number of the ground reaction force model of the half-circle leg. The units of the axes "ϵ" are represented by voltage—larger voltage indicates smaller strain; nominal voltage located between $2.6 \sim 2.8$

the dynamic equation. Therefore, in order to simplify the equation shown in (3.1) to the fixed force-displacement relationship shown in (3.2), a few strict assumptions are required, like no mass, damping, or quasi-static operation region, as detailed in Section 3.3.

3.7.5 Evaluation of the Configuration and the Ground Reaction Force Model

The procedure to evaluate a 2 DOF quadratic configuration model for the half-circle leg is similar to that of the linear configuration model for the 4-bar leg. This is done by comparing the leg configuration from the modeling output of the leg sensor to the measurements of the virtual ground truth system using the same setup illustrated in Section 3.6.4 and shown in Figure 3.7. Evaluating the ground reaction force model can be achieved by a similar procedure in which the virtual ground truth system is replaced by a force plate to measure the force between foot and the ground detailed in Appendix C.

The evaluation of the models of the half-circle leg and its applications are beyond the scope of this dissertation. Our focus in the next chapter moves onto the information of the leg configuration of the 4-bar leg and its applications.

CHAPTER 4

Body Pose Estimation by Leg Sensor

This chapter introduces a computational algorithm for continuous measurement of full body pose for a hexapod robot utilizing the 4-bar leg configuration sensor introduced in Chapter 3. We will focus on an alternating tripod walking gait because of its familiarity and importance in RHex. The computations presented below generalize to a family of gaits characterized by two conditions: A) the body is supported by at least three legs with non-collinear toes at any given time; and B) ground contact legs have no toe slippage[1].

Section 4.1 introduces the algorithm of body pose estimation, including the within stride body pose detailed in Section 4.1.1, odometry via sequential composition in Section 4.1.2, and a short discussion in Section 4.1.3. In Section 4.3 we evaluate the performance of this algorithm at widely varying body speeds in Section 4.3.1 and over dramatically different ground conditions in Section 4.3.2 by means of a 6 DOF vision-based ground truth measurement system (GTMS) detailed in Section 4.2. We also compare the odometry performance to that of sensorless schemes, both on legged as well as on a wheeled version of the robot, using GTMS measurements of elapsed distance in Section 4.3.3, followed by a short discussion in Section 4.4.

4.1 Computation of Body Pose

In an alternating tripod walking gait we identify two intervals: the *single stance phase*[2] and the *double stance phase* when all legs are in ground contact as depicted in Figure 4.1. This suggests a hierarchically structured algorithm with two levels:

1. A low level, discussed in Section 4.1.1, operating during individual single stance phases, computing the body pose in a locally defined coordinate system. We will

[1]These conditions guarantee that the toe contacts yield a well defined coordinate system fixed in the world frame. Appropriate generalizations of the calculations would extend the computation of full body pose to other kinds of legged robots, like quadrupeds or even bipeds with foot or surface contact.

[2]Single Stance Phase denotes the instance when the body is supported by only one tripod where the three toes of the front and rear ipsilateral legs and the middle contralateral leg of a tripod are all in contact with the ground, as depicted in Figure 4.1(a).

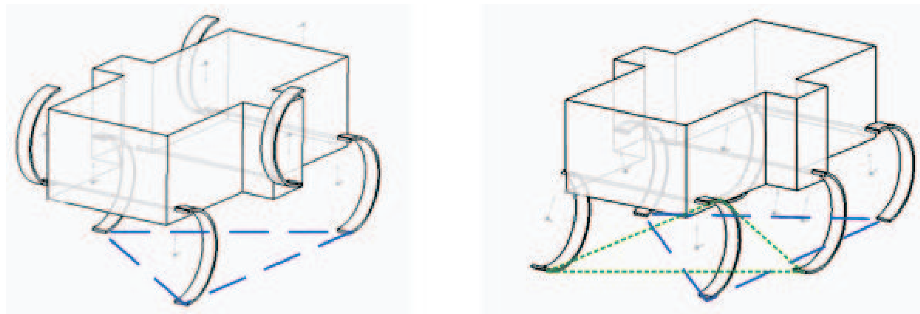

(a) (b)

Figure 4.1: Two types of stances of RHex in a tripod walking gait: (a) single stance phase(left tripod: blue dashed; right tripod: green dotted) ; double stance phase

call the tripod coordinate system $\mathcal{T}$, rigidly related to the world coordinate system $\mathcal{W}$.

2. A high level sequence of compositions, described in Section 4.1.2, relating the tripod coordinate systems in consecutive single stance phases to evaluate the body pose with respect to the world coordinate system, $\mathcal{W}$.

4.1.1 Pose Computation during Single Stance

Assume a leg model $\mathbf{s}_i(z_i)$, where z_i denotes the sensory measurements available regarding the configuration of the kinematic chain connecting the robot body COM to the i$^{\text{th}}$ toe and $\mathbf{s}_i$ represents the point of toe contact with respect to the robot body coordinate system $\mathcal{B}$. For example, in the RHex implementation, z_i consists of two mappings—first, the kinematic mapping relating the i$^{\text{th}}$ hip clamp coordinate system $\mathcal{C}_i$, to the body coordinate system $\mathcal{B}$, by a rigid transformation $\mathcal{N}_{\mathcal{C}_i\mathcal{B}}(\theta_i) : \mathcal{C}_i \rightarrow \mathcal{B}$, which is parameterized by the angular position of hip shaft θ_i; second, another kinematic mapping relating the strain across the compliant portion of the leg as read from the sensor suite ϵ_{ij}, to the leg configuration in the clamp coordinate system, by a numerical modeling $\mathcal{M}_{SD\_i}$, detailed in Chapter 3—yielding the equation:

$$\mathbf{s}_i(\theta_i, \epsilon_{ij}) = \mathcal{N}_{\mathcal{C}_i\mathcal{B}}(\theta_i) \circ \mathcal{M}_{SD\_i}(\epsilon_{ij}) \tag{4.1}$$

where $i = 1, 2, ..., 6$ denotes the index of the leg and j represents the index of the strain reading in each leg, $j = 1$ for the 4-bar leg; $j = 1, 2$ for the half-circle leg.

Without loss of generality, consider the case of a single left tripod stance shown in Figure 4.2. With the definition of the support triangle $\mathcal{S}$, whose vertices are identified with the non-collinear toes of the ground contact legs, we can derive the unit vectors along the two edges of the support triangle $\mathcal{S}$, that intersect at $\mathbf{s}_3$ as

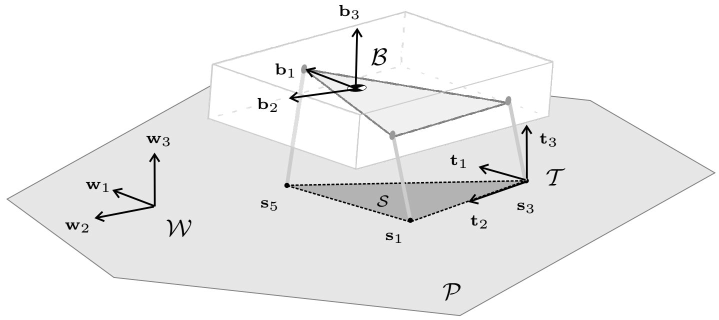

Figure 4.2: Sketch of RHex in left-tripod stance together with associated terminologies

$$\mathbf{e}_1 := \frac{\mathbf{s}_5-\mathbf{s}_3}{||\mathbf{s}_5-\mathbf{s}_3||_2} \quad \mathbf{e}_2 := \frac{\mathbf{s}_1-\mathbf{s}_3}{||\mathbf{s}_1-\mathbf{s}_3||_2}.$$

Now define the tripod coordinate system $\mathcal{T}$, with origin at $\mathbf{s}_3$ and orthonormal basis derived by Gram-Schmidt Orthogonalization as

$$\mathbf{t}_1 := \frac{\mathbf{e}_1-(\mathbf{t}_2^T\mathbf{e}_1)\mathbf{t}_2}{||\mathbf{e}_1-(\mathbf{t}_2^T\mathbf{e}_1)\mathbf{t}_2||_2} \quad \mathbf{t}_2 := \mathbf{e}_2 \quad \mathbf{t}_3 := \mathbf{t}_1 \times \mathbf{t}_2$$

represented in the body coordinate system $\mathcal{B}$. Then a rigid transformation $\mathcal{N}_{\mathcal{BT}}$, relates points $\mathbf{p}_{\mathcal{B}}$, expressed in the body coordinate system $\mathcal{B}$, to points expressed in the tripod coordinate system $\mathcal{T}$, by

$$\mathcal{N}_{\mathcal{BT}}(\mathbf{p}_{\mathcal{B}}) := \mathbf{M}_{\mathcal{BT}}(\mathbf{p}_{\mathcal{B}} - \mathbf{s}_3) \tag{4.2}$$

where $\mathbf{M}_{\mathcal{BT}} := \begin{bmatrix} \mathbf{t}_1 & \mathbf{t}_2 & \mathbf{t}_3 \end{bmatrix}^T$ (rotation matrix).

Equation (4.2) contains 6 DOF within stride body pose information [Pau83]. The COM displacement with respect to current tripod coordinate system $\mathcal{T}$, is read off as $-\mathbf{M}_{\mathcal{BT}}\mathbf{s}_3$, where the third entry also represents the absolute height of COM to the level ground r_z. Similarly, by deriving the body lateral and fore/aft unity vectors in the tripod coordinate system $\mathbf{b}_1 = \mathbf{M}_{\mathcal{BT}}\begin{bmatrix} 1 & 0 & 0 \end{bmatrix}^T$ and $\mathbf{b}_2 = \mathbf{M}_{\mathcal{BT}}\begin{bmatrix} 0 & 1 & 0 \end{bmatrix}^T$, respectively, it directly follows that the orientation states, pitch α, roll β and yaw γ, with respect to current tripod coordinate system $\mathcal{T}$, are

$$\begin{aligned} \alpha &:= \arctan\left(\frac{\pi_3 \circ \mathbf{b}_2}{\sqrt{(\pi_1 \circ \mathbf{b}_2)^2 + (\pi_2 \circ \mathbf{b}_2)^2}}\right) \\ \beta &:= \arctan\left(\frac{\pi_3 \circ \mathbf{b}_1}{\sqrt{(\pi_1 \circ \mathbf{b}_1)^2 + (\pi_2 \circ \mathbf{b}_1)^2}}\right) \\ \gamma &:= \arctan\left(\frac{\pi_1 \circ \mathbf{b}_2}{\sqrt{(\pi_2 \circ \mathbf{b}_2)^2 + (\pi_3 \circ \mathbf{b}_2)^2}}\right) \end{aligned} \tag{4.3}$$

where we use the notation $\pi_i \circ \mathbf{v}$ to denote the i^{th} entry of a vector, $\mathbf{v} \in \mathbb{R}^n$. Like COM displacement in vertical direction r_z, two of the three orientation states, pitch α and roll

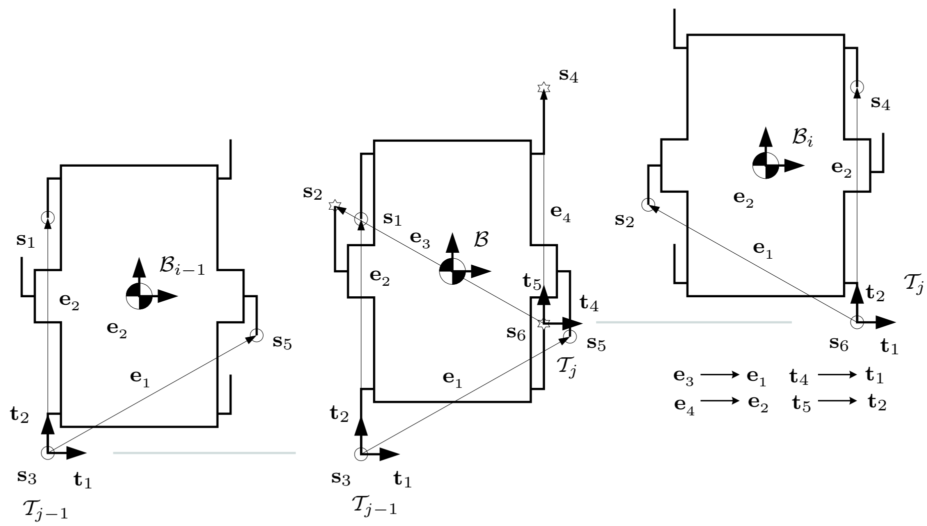

Figure 4.3: Sketch of motion of two consecutive tripod stance phases and one double stance phase in between. The symbols $\circ$ and $\star$ indicate the event of foot touchdown.

β, present the absolute orientation with respect to the level ground, the world coordinate system, $\mathcal{W}$. On the other hand, to represent the remaining states—COM displacement in lateral r_x, fore/aft r_y and yaw γ—requires the information of the motion history which will be detailed in the next section.

4.1.2 Leg Based Odometry via Composition of Single Stance Measurements

We use the term *odometry* to denote the computation of instantaneous body pose in the world coordinate system $\mathcal{W}$, relative to a frame originally aligned with that of the body before the initiation of its motion. We will now detail how the single stance phase pose computations described above in Section 4.1.1 can be integrated over multiple steps to generate this continuous computation of absolute body pose.

First we compute the homogeneous transformation between the tripod coordinate system of consecutive single stance phases $\mathcal{T}_j$ and $\mathcal{T}_{j+1}$, as follows. Assuming the toes defining these tripod coordinate systems are stationary throughout their presumed stances, i.e. there is no slippage and no liftoff, and assuming there is an adequate period of double support where the two stance phases overlap for a time sufficient to complete their respective single stance pose computation Then both coordinate systems are related to the same moving body coordinate system, $\mathcal{B}$ as depicted in Figure 4.3. Now, assuming that the prior tripod coordinate system $\mathcal{T}_j$, has been expressed in world coordinates, the representation of its successor $\mathcal{T}_{j+1}$, in the world coordinate system follows by the properties of rigid transformations in a straightforward manner that we now detail.

We index single stance phases, $j = 0, 1, ...$, according to their occurrences over the course of locomotion where we denote the j^{th} single stance tripod coordinate system by $\mathcal{T}_j$. Without loss of generality, assume that the tripod coordinate system of the first single stance phase coincides with the world coordinate system, $\mathcal{T}_0 \equiv \mathcal{W}$.

The key to establishing a relationship between the tripod coordinate systems of two consecutive single stance phases is the fact that there exists an intermediate double stance phase where all legs are in ground contact. This allows us to define simultaneously the tripod coordinate systems of the single stance phase before, $\mathcal{T}_{j-1}$, and after, $\mathcal{T}_j$, this double stance phase. Letting $\mathcal{N}_{\mathcal{B}_j\mathcal{T}_j}$ denote the map from the body coordinate system $\mathcal{B}$, to the j^{th} tripod coordinate system $\mathcal{T}_j$, defined in (4.2), we compute the map relating the two tripod coordinate systems of consecutive single stance phases $\mathcal{N}_{\mathcal{T}_j\mathcal{T}_{j-1}} : \mathcal{T}_j \rightarrow \mathcal{T}_{j-1}$, given by

$$\mathcal{N}_{\mathcal{T}_j\mathcal{T}_{j-1}} := \mathcal{N}_{\mathcal{B}_{j-1}\mathcal{T}_{j-1}} \circ \mathcal{N}^{-1}_{\mathcal{B}_j\mathcal{T}_j}.$$

In the on-line implementation of the pose computation algorithm we need to detect double stance phase in order to compute the transformations between tripod coordinate systems of consecutive single stance phases $\mathcal{N}_{\mathcal{T}_j\mathcal{T}_{j-1}}$. Taking advantage of the flat ground plane $\mathcal{P}$, and assuming that all toes lie on the same plane only during double stance phase, in our application we empirically set a threshold $\overline{f_\rho}$, on a planarity function $f_\rho(\mathbf{s}_i), {\scriptstyle i=1\ldots6}$, detailed below to determine the double stance phase.

Planarity function is a function we use to determine the "planarity" of a set of points by finding the least squared error to a specific plane which is parameterized with minimum least squared error to these points. Given a set of N points in the 3-dimensional space $\mathbf{s}_i, {\scriptstyle i=1\ldots N}$, by defining the covariant matrix as

$$\mathbf{P} := \textstyle\sum_{i=1}^{N} \mathbf{s}_i^T \mathbf{s}_i - \overline{\mathbf{s}}^T \overline{\mathbf{s}} \quad \text{where} \quad \overline{\mathbf{s}} := \frac{1}{N} \sum_{i=1}^{N} \mathbf{s}_i,$$

the eigenvector $\mathbf{v}$, associated with the smallest eigenvalue in $\mathbf{P}$ by function $\mathbf{V}: \quad \mathbf{v} := \mathbf{V}(\mathbf{P})$ represents the normal direction of the plane with minimum least squared error to these points. With the knowledge that the plane passes through the mean of the points, we can define the *planarity function* as

$$f_\rho(\mathbf{s}) := \tfrac{1}{N} \textstyle\sum_{i=1}^{N} [(\mathbf{s}_i - \overline{\mathbf{s}}).\mathbf{V}(\mathbf{P})]^2 \tag{4.4}$$

which yields the mean squared distance of the points around the best common plane[3].

In our application we empirically set a threshold $\overline{f_\rho}$ on the planarity function $f_\rho(\mathbf{s})$, with six toe coordinates in the body coordinate system $\mathbf{s}_i, {\scriptstyle i=1\ldots6}$, as the inputs to determine the double stance phase in order to compute the transformations between tripod coordinate systems of consecutive single stance phases. Figure 4.4(a) illustrates the flow diagram of the complete on-line body pose computation algorithm utilizing the planarity function $f_\rho(\mathbf{s})$.

[3]In general, planarity can also be determined by the relation between eigenvalues in a covariant matrix $\mathbf{P}$, but we prefer to use (4.4) because it is represented in physical measurements.

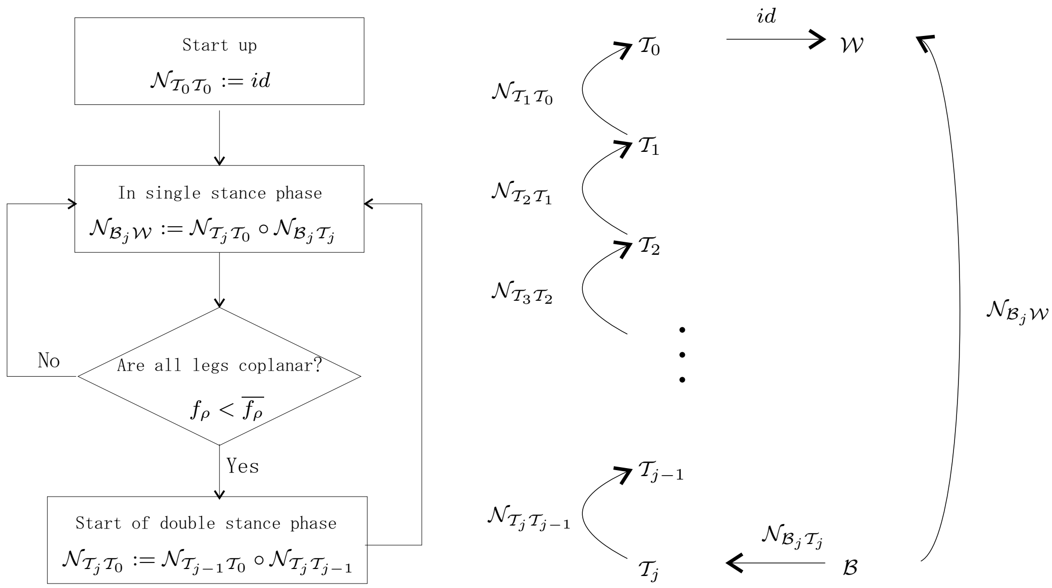

(a) (b)

Figure 4.4: (a) Flow chart for the within-stride body pose computation and leg odometry functions; (b) Commutative diagram relating the tripod coordinate systems $\mathcal{T}_j$.

The commutative diagram of Figure 4.4(b) illustrates the sequential relationship between the tripod coordinate systems $\mathcal{T}_j$. As a direct consequence, the map $\mathcal{N}_{\mathcal{T}_j\mathcal{T}_0} : \mathcal{T}_j \rightarrow \mathcal{W}$, relating the j$^{\text{th}}$ tripod coordinate system $\mathcal{T}_j$, to the world coordinate system $\mathcal{W} \equiv \mathcal{T}_0$, can be defined recursively,

$$\mathcal{N}_{\mathcal{T}_j\mathcal{T}_0} := \mathcal{N}_{\mathcal{T}_{j-1}\mathcal{T}_0} \circ \mathcal{N}_{\mathcal{T}_j\mathcal{T}_{j-1}}, \quad j \in \{1, 2, ...\}$$

where $\mathcal{N}_{\mathcal{T}_0\mathcal{T}_0} := id$. This in turn leads to the definition of the rigid transformation $\mathcal{N}_{\mathcal{B}_j\mathcal{W}} := \mathcal{N}_{\mathcal{T}_j\mathcal{T}_0} \circ \mathcal{N}_{\mathcal{B}_j\mathcal{T}_j}$ that relates points, $\mathbf{p}_{\mathcal{B}}$, expressed in the body coordinate system, $\mathcal{B}$, during the j$^{\text{th}}$ single stance phase, to their representation in the world coordinate system, $\mathcal{W}$, which we prefer to write as

$$\mathcal{N}_{\mathcal{B}_j\mathcal{W}}(\mathbf{p}_{\mathcal{B}}) := \mathbf{M}_{\mathcal{B}_j\mathcal{W}} \left(\mathbf{p}_{\mathcal{B}} - \mathbf{c}_j\right). \tag{4.5}$$

More precisely, $\mathbf{M}_{\mathcal{B}_j\mathcal{W}}$ is the rotation matrix transforming the coordinates in the j$^{\text{th}}$ body coordinate system to the world coordinate system, and $\mathbf{c}_j$ is the origin of the world frame represented in the j$^{\text{th}}$ body frame.

The body pose is now read off the entries of the transformation matrices in the familiar manner. The COM translation in lateral r_x and fore/aft r_y directions as well as body orientation in yaw γ are computed from the rigid transformation, $\mathcal{N}_{\mathcal{B}\mathcal{W}}$, shown in (4.5) in the similar manner to the method shown in Section 4.1.1 [Pau83] since these three configuration variables require the whole history of locomotion, i.e. localization state. On the other hand, the COM translation in the vertical r_z direction as well as body orientation in pitch α and roll β are directly computed from the within-stride rigid transformation $\mathcal{N}_{\mathcal{BT}}$, shown in (4.2) as detailed in Section 4.1.1 to eliminate the possible accumulation error due to unnecessary integration since these are history-independent states, i.e. stability states.

4.1.3 Short Discussion

The algorithm is quite general, remaining valid, in principle, on any terrain to which a fixed toe coordinate system can be established. In practice, two caveats mitigate against its utility on badly broken or unsteady ground. Considering the latter, for sufficiently treacherous terrain, the toe frame will cease to be statically stable, and slipping legs will invalidate the assumptions upon which the computation is based. In these settings, the ability of a legged machine like RHex to balance dynamically will exceed the ability of this quasi-static strain-based model to sustain accurate pose; leg strain data is likelier to be more useful as a means of determining ground reaction forces; pose information would require the IMU we discuss in the paper's conclusion. Considering the former, the value of this algorithm in isolation also seems likely to diminish on badly broken ground—even terrain that affords good stable toe holds—since the orientation of the resulting toe frame relative to one fixed in the static world will presumably be completely unknown. Again, we anticipate that the addition of IMU based data, for example, knowledge of the direction of gravity, will prove vital in such settings. Along the same lines, the reader should note that there is no intrinsic need for a tripod of ground contacts—merely a statically stable toe frame which might even be established by a biped's single foot.

4.2 Ground Truth Measurement System for 6 DOF Body Pose

In order to evaluate the performance of the body pose computation algorithm in realistic robot operating conditions, we utilize a ground truth measurement system (GTMS) [Sha03], a 3-dimensional visual tracking system for multiple markers.

Figure 4.5 illustrates the key components of the GTMS setup. Two analog cameras (SONY XC-77) are located on both sides of a 3m x 3m runway looking down from a height of 2 meters combined with two halogen lamps installed next to each camera for illumination. The video streams are synchronized by two junction boxes (SONY, JB-77), digitized by two frame grabber cards (Data Translation, DT3155) at 30 Hz, and imported into a Pentium-based PC running Linux as our computational resource. To ease the detection of the markers, the runway and the robot RHex are covered with black cardboard as shown in Figure 4.6(a). Three markers made by spherical balls covered with 3M reflective tape are

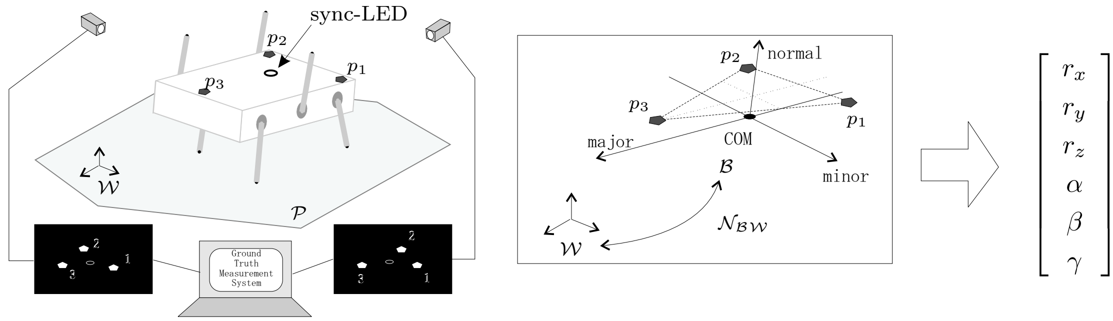

Figure 4.5: Ground Truth Measurement System: Two cameras track the three markers on the body which are depicted by numbered pentagons. We use a forth marker (an LED) on the robot, shown as an empty circle, to synchronize the logged data stored in the robot with the visual data. An off-line system computes body pose with respect to the world coordinate system $\mathcal{W}$.

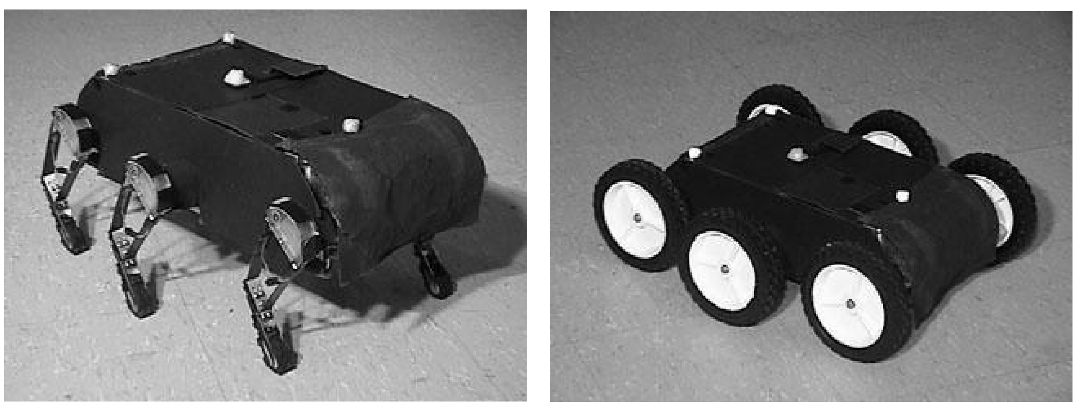

(a) (b)

Figure 4.6: Photos of Legged RHex (a) and Wheeled RHex (b) in black covers

installed on top of the robot. For synchronization between robot actions with the visual recording a LED referred as sync-LED installed on top of the robot acts as a controllable forth marker which is visible to the cameras as well.

An experiment starts with the robot at standing pose in the beginning of the runway within the field of view of both cameras. The sync-LED which is off in the beginning is switched on, indicating that $t = 0$, for the run right after visual recording starts. For the following 9 seconds, the maximum length of the visual recording limited by PC's buffer, the user commands the robot to walk in a straight line while GTMS records digital video streams from two cameras into PC's memory. After the recording is complete, the raw visual data is processed by an off-line tracking program which triangulates the positions of all the markers starting from the frame when the sync-LED is first detected, and the

Table 4.1: Body Pose Absolute Maximum Error in GTMS Measurement

state	r_x	r_y	r_z	α	β	γ
unit	cm	cm	cm	deg	deg	deg
abs max	0.5	0.5	0.5	1.71	2.79	1.30

final markers' trajectories represented in the world coordinate system, $\mathcal{W}$, are saved in a file for follow-up computations. The robot pose can then be calculated based on the known geometric relation between the markers and its COM.

Currently three markers, p_1, p_2 and p_3, are installed on the top of RHex's frame on left back corner, right back corner, and middle front accordingly shown in Figure 4.5(Left). The COM located in the center of the RHex frame with distance d_{COM} to the plane defined by three markers $\mathcal{P}_{marker}$, can be derived by the following procedures. First, find the normal vector of the plane $\mathcal{P}_{marker}$, $\mathbf{n}_{marker}$ by the cross product ($\mathbf{n}_{marker} = \frac{(p_2-p_3)\times(p_1-p_3)}{\sqrt{||(p_2-p_3)\times(p_1-p_3)||_2^2}}$). Second, find the point p_5 located on the plane $\mathcal{P}_{marker}$ where the normal vector passes though COM, which is $p_5=\frac{1}{4}p_1+\frac{1}{4}p_2+\frac{1}{2}p_3$ in the current setting. Third, Derive the COM located with distance d_{COM} below p_5 on the $\mathcal{P}_{marker}$ by the equation $p_5+\mathbf{n}_{marker}d_{COM}$. Three orientation angles, pitch α, roll β, and yaw γ, can be directly derived by the same equation shown in (4.3) with $\mathbf{b}_1 = p_2-p_1$ and $\mathbf{b}_2 = p_3-\frac{1}{2}p_1-\frac{1}{2}p_2$.

The triangulation performance of the GTMS is measured at a set of points scattered within the field of view of the cameras. We compare the output of the triangulation to the known physical location for each marker and determine the absolute maximum error in triangulation to be 5mm. In the above procedure, error in the vertex positions leads to maximum error in body pose states. For each state we construct the worst case scenario that yields the largest error given by a triangulation error. Plugging in the empirically measured triangulation error we obtain the absolute maximum error for each state as listed in Table 4.1.

4.3 Performance Evaluation

We now report on the performance of the pose estimation scheme presented in Section 4.1 using the strain based leg sensor introduced in Section 3.6. We investigate performance under realistic operating conditions over multiple steps, reporting on the effects of increasing speed and decreasing surface friction. The reader should note that RHex's relatively constrained kinematics preclude the exercise of its yaw degree of freedom when it walks with no aerial phase and no toe slippage, hence the implementation we discuss in this section will entail no data of that nature—we discuss measurements involving only the five configuration variables: the displacement of the COM in the lateral direction, r_x, fore/aft direction, r_y, and vertical direction, r_z, as well as orientations given by pitch, α, and roll,

Table 4.2: RMS Error of the Body Pose Computational Algorithm over Multiple Steps (Medium speed, 0.35 m/sec)

Run #	State					Reference	
						total walking distance	number of strides
	r_x (cm)	r_y (cm)	r_z (cm)	α (deg)	β (deg)	ν (cm)	υ
Run #1	0.56	1.52	0.17	0.50	0.63	85.1	8
Run #2	0.57	1.98	0.28	0.64	0.80	75.0	7
Run #3	0.33	1.20	0.22	0.78	0.81	75.2	7
Run #4	0.27	1.46	0.24	0.54	0.69	96.8	9
Run #5	0.30	1.94	0.19	0.53	0.64	84.2	8
avg	0.41	1.42	0.22	0.60	0.71	83.3	7.8
std	0.13	0.32	0.04	0.10	0.08	8.0	0.7

β in the world coordinate system, $\mathcal{W}$.

In our assessment we compare the output of the computational algorithm to independent measurements made by a visual GTMS described in Section 4.2, different from the one used in the previous section described in Section 3.5. Performance is measured by the vector RMS error between the outputs of the algorithm and GTMS, given by

$$f_{RMSE}(\mathbf{d}, \hat{\mathbf{d}}) := \sqrt{(\left|\left|\mathbf{d} - \hat{\mathbf{d}}\right|\right|_2^2 / N)} \tag{4.6}$$

where $\mathbf{d} = (\mathbf{d}_1, ..., \mathbf{d}_N)$ and $\mathbf{d}_i := (r_x, r_y, r_z, \alpha, \beta)_i$ represents the configuration trajectory with length N from the GTMS, while $\hat{\mathbf{d}}$ denotes the corresponding configuration trajectory estimate output from the algorithm.

A typical run yields two sets of data for each configuration variable: GTMS measurements (green solid line); and algorithm outputs (blue dashed line). Figure 4.7 shows the comparison of these plots for each configuration variable for a typical run over multiple steps. Note, as explained at the end of Section 4.1.2 that the r_x and r_y computed (dashed) traces represent the result of the high level "Odometry via Composition" algorithm while the r_z, α, and β traces represent the result of the within stride computation described in Section 4.1.1. In Table 4.2 we compute the RMS error for each configuration variable as well as the mean (avg) and standard deviation (std) of the RMS error for a typical experiment set which contains five runs[4]. We also include GTMS measured elapsed distance ν, and number of tripod strides for each run υ, as reference.

[4]Performance of single tripod steps is detailed in Section 4.3.4.

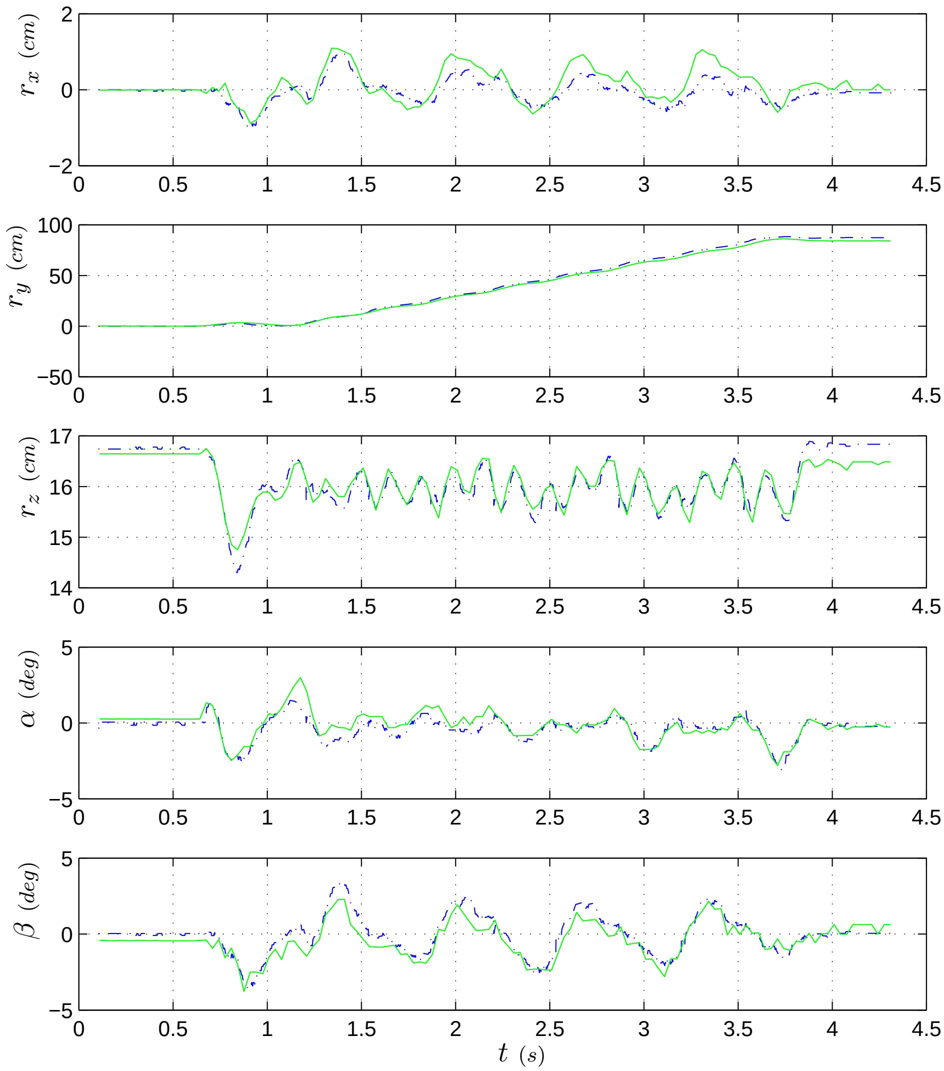

Figure 4.7: Body pose states measured by GTMS (solid line) and computed according to our algorithm (dashdot line)

4.3.1 Performance at Varying Speeds

Three sets of experiments measure the effects of walking speed on pose estimation performance: slow (0.25 m/s); medium (0.35 m/s); and fast (0.51 m/s). All of these operating regimes fall into the continuous contact family that our algorithm presumes. However, the duration of the double stance and the magnitude of the ground reaction forces differ as the speed changes resulting in different levels of error in frame composition during double

Table 4.3: RMS Error of the Body Pose Computational Algorithm over Multiple Steps at Varying Speeds over Cardboard ($\mu_s = 0.65$, $\mu_k = 0.60$)

Statistics	State					Reference	
	r_x (cm)	r_y (cm)	r_z (cm)	α (deg)	β (deg)	total walking distance ν (cm)	number of strides υ
Slow walking speed (0.25 m/s)							
avg	0.42	4.53	0.30	0.78	0.73	84.0	8.4
std	0.13	0.80	0.08	0.09	0.06	6.2	0.5
Medium walking speed (0.35 m/s)							
avg	0.41	1.42	0.22	0.60	0.71	83.8	7.8
std	0.13	0.32	0.04	0.10	0.08	8.0	0.7
Fast walking speed (0.51 m/s)							
avg	0.39	1.41	0.27	0.63	0.68	84.8	7.4
std	0.05	0.25	0.04	0.08	0.08	6.5	0.7

stance.

Table 4.3 summarizes the results for the speed experiments. At all speeds, small RMS error values compared to the robot size (50cm x 25cm x 15cm) indicate successful pose computation where the mean error in angular states remain less than 1 degree and that of lateral r_x and vertical r_z positions are less than 1 cm. Since the slippage during double stance has significant impact on the fore/aft r_y direction of the robot, the corresponding RMS error is the largest. We observe that the error in the fore/aft position decreases with increasing speed. This is due to two changes: 1) an increase in speed causes a shorter double stance period improving the accuracy of the sequential composition computation; and 2) ground reaction force magnitude increases with speed, decreasing the likelihood of slippage during stance.

4.3.2 Performance over Different Ground Conditions

In a second set of experiments we investigate the effects of varying surface coefficients of friction, which we expect to have most significant impact on the accuracy of our pose estimation algorithm. For this study, we appeal to the standard macroscopic model of stickiness [HR88], and characterize surfaces according to their static or stiction, μ_s, and kinetic or sliding, μ_k, friction coefficients.

We empirically determine the friction coefficient of surfaces to be used in these experiments by placing the robot on the surface of interest in the standing pose and pulling in the fore/aft direction. The exerted force is measured by a 1-DOF force sensor (Cooper

Table 4.4: RMS Error of the Body Pose Computational Algorithm over Multiple Steps over Different Ground Conditions at Slow Walking Speed (0.25 m/s)

Statistics	State					Reference	
						total walking distance	number of strides
	r_x (cm)	r_y (cm)	r_z (cm)	α (deg)	β (deg)	ν (cm)	υ
Cardboard ($\mu_s = 0.65$, $\mu_k = 0.60$)							
avg	0.42	4.53	0.30	0.78	0.73	84.0	8.4
std	0.13	0.80	0.08	0.09	0.06	6.2	0.5
Plastic ($\mu_s = 0.33$, $\mu_k = 0.27$)							
avg	0.40	4.45	0.51	0.83	0.65	79.0	8.0
std	0.08	0.82	0.05	0.05	0.06	6.2	0.6
Plastic covered with wet soap ($\mu_s = 0.20$, $\mu_k = 0.11$)							
avg	1.39	9.72	0.45	0.63	1.12	73.8	7.4
std	0.22	1.30	0.07	0.07	0.22	5.6	0.5
Plastic covered with dry soap ($\mu_s = 0.07$, $\mu_k = 0.05$)							
avg	1.82	9.40	0.42	0.63	0.65	78.6	8.2
std	0.28	0.56	0.07	0.09	0.05	3.1	0.4

Instruments, LFS260), and the collected data is analyzed to determine the static, μ_s, and kinetic, μ_k, friction coefficients.

In these experiments the robot walks at slow speed (0.25 m/sec) over four types of surfaces: cardboard ($\mu_s = 0.65$, $\mu_k = 0.60$); plastic ($\mu_s = 0.33$, $\mu_k = 0.27$); plastic covered with wet soap ($\mu_s = 0.20$, $\mu_k = 0.11$); and plastic covered with dry soap ($\mu_s = 0.07$, $\mu_k = 0.05$). Table 4.4 summarizes the results of this experiment set. As the friction coefficient decreases we observe significant deterioration in the accuracy of the horizontal components (r_x, r_y) of the COM. This is a direct result of the increase in slippage. The vertical component (r_z) of the COM and angular configuration variables (α, β) are not affected as severely since these are invariant with respect to COM horizontal translation (the most significant component of a "slipping" robot's motion), and, moreover, their computation only depends on the current single stance phase measurements but not on any of the previous ones. In general, except on the most adversarial slippery surfaces such as the soaped plastic that we specially prepared for this study, the algorithm performs well and consistently over normal ground conditions. For example, those characterizing cardboard or plastic that seem to typify the static friction coefficients we observe ($0.3 \leq \mu_s \leq 0.7$) on most of the indoor terrain that the robot's rubber toes encounter.

4.3.3 Odometry Performance

Although online estimation of within-stride state represents our chief motivation for developing this body pose sensor, we have noted in the introduction a large literature in the field of mobile robotics concerned with odometry. We have also observed in Section 4.1.2 that the assumptions of the walking gait over level terrain allow the computation of legged odometry using the procedure that we described there. Thus, we are interested in evaluating the idea of "legged odometry" presented here.

Table 4.5 compares our leg strain based odometry estimates, by reference to discrepancies with GTMS measurements of elapsed distance, with sensorless schemes for the legged machine as well as on a wheeled implementation of the Robot pictured in Figure 4.6(b). With no sensing apart from motor shaft measurements, blind odometry estimates result from counting the number of leg cycles and multiplying by a previously calibrated distance-per-cycle constant. This is also the traditional approach to odometry in wheeled vehicles as well. We ran calibration tests for RHex and a wheeled implementation of the robot, counting the number of motor shaft cycles over the same long flat surface to get the best possible conversion constant. The table presents discrepancies, $\kappa(\%)$ $(={|\Delta\nu|}/{\nu})$, as a percentage of the GTMS measured elapsed distance ν, for each of the three odometry methods: sensorless legged; pose-based legged; and sensorless wheeled. The results show that the leg strain based odometry from body pose measurements is greatly superior to the blind predictions of the open loop scheme, by nearly an order of magnitude at the higher speeds where the inaccuracies of double support have less effect. The dynamical nature of legged walking[5] causes speed variations during locomotion that incur significantly more slippage, exacerbated at slower gaits by prolonged double support, than the far smoother ride afforded by wheels. Thus, our sensor based legged odometry is significantly less accurate than the blind results from counting motor shaft revolutions on the wheeled version of the same machine.

4.3.4 Single Stance Body Pose Computation

The performance analysis of the pose computation in the previous subsections follows the hierarchical structure of the algorithm detailed in Section 4.1.2. This section focuses on the error in the low level "stride by stride" individual single stance phases detailed in Section 4.1.1 without the complications introduced by the sequential composition in the higher level. We set the origin of both the world coordinate system $\mathcal{W}$, as well as the tripod coordinate system $\mathcal{T}$, according to the COM of the robot measured by the GTMS in the beginning of each single stance phase. Based on this common reference, the output of the algorithm and the measurements of the GTMS are plotted against each other. Figure 4.8 shows such a set of plots for a typical run. For each single stance phase we evaluate the RMS Error for each configuration variable. Table 4.6 summarizes the RMS Error values for

[5] even in the absence of an aerial phase, RHex's gaits exhibit a significant interchange of body kinetic and leg spring potential energy in stance.

Table 4.5: Odometry Performance at Varying Speeds and over Different Ground Conditions (RHex with Leg Strain Based Pose Sensor *vs.* Sensorless RHex *vs.* Wheeled RHex)

Statistics	Legged RHex					Wheeled RHex	
	GTMS	sensorless		pose-sensor-based		GTMS	
	ν	$\lvert\Delta\nu_d\rvert$	κ_d	$\lvert\Delta\nu_l\rvert$	κ_l	ν	κ_w
	(cm)	(cm)	(%)	(cm)	(%)	(cm)	(%)
Slow walking speed (0.25 m/s) on cardboard ($\mu_s = 0.65$, $\mu_k = 0.60$)							
avg	84.0	17.9	21.4	5.1	6.1	87.6	0.3
std	6.2	0.7	2.0	1.9	0.7	3.3	0.09
Medium walking speed (0.35 m/s) on cardboard ($\mu_s = 0.65$, $\mu_k = 0.60$)							
avg	83.8	17.6	21.1	1.8	2.2	83.3	0.3
std	8.0	1.8	1.0	0.8	1.0	1.8	0.07)
Fast walking speed (0.51 m/s) on cardboard ($\mu_s = 0.65$, $\mu_k = 0.60$)							
avg	84.8	13.9	16.3	1.5	1.7	80.8	0.5
std	6.5	3.1	2.9	0.6	0.6	0.9	0.26)
Slow walking speed on plastic ($\mu_s = 0.33$, $\mu_k = 0.27$)							
avg	79.0	18.0	22.8	5.3	6.6	87.6	0.3
std	6.2	1.9	1.8	3.4	4.4	5.2	0.08
Slow walking speed on plastic covered with wet soap ($\mu_s = 0.20$, $\mu_k = 0.11$)							
avg	73.8	16.0	21.8	6.0	8.2	90.2	1.7
std	5.6	0.6	1.5	0.4	0.7	4.0	0.22
Slow walking speed on plastic covered with dry soap ($\mu_s = 0.07$, $\mu_k = 0.05$)							
avg	78.6	20.9	26.5	14.0	17.8	93.2	1.2
std	3.1	2.5	2.9	0.7	0.6	5.1	0.43

Table 4.6: RMS Error of Single Stance Body Pose Computation (Medium speed, 0.35 m/sec)

Run #	State				
	r_x (cm)	r_y (cm)	r_z (cm)	α (deg)	β (deg)
Run #1	0.16	0.40	0.13	0.44	0.58
Run #2	0.22	0.35	0.19	0.56	0.89
Run #3	0.27	0.33	0.19	0.54	0.77
Run #4	0.24	0.44	0.16	0.42	0.78
Run #5	0.27	0.52	0.13	0.50	0.70
avg	0.23	0.41	0.16	0.49	0.74
std	0.04	0.07	0.03	0.05	0.10

the data illustrated in Figure 4.8. The mean and standard deviation of RMS Error for each state is also computed.

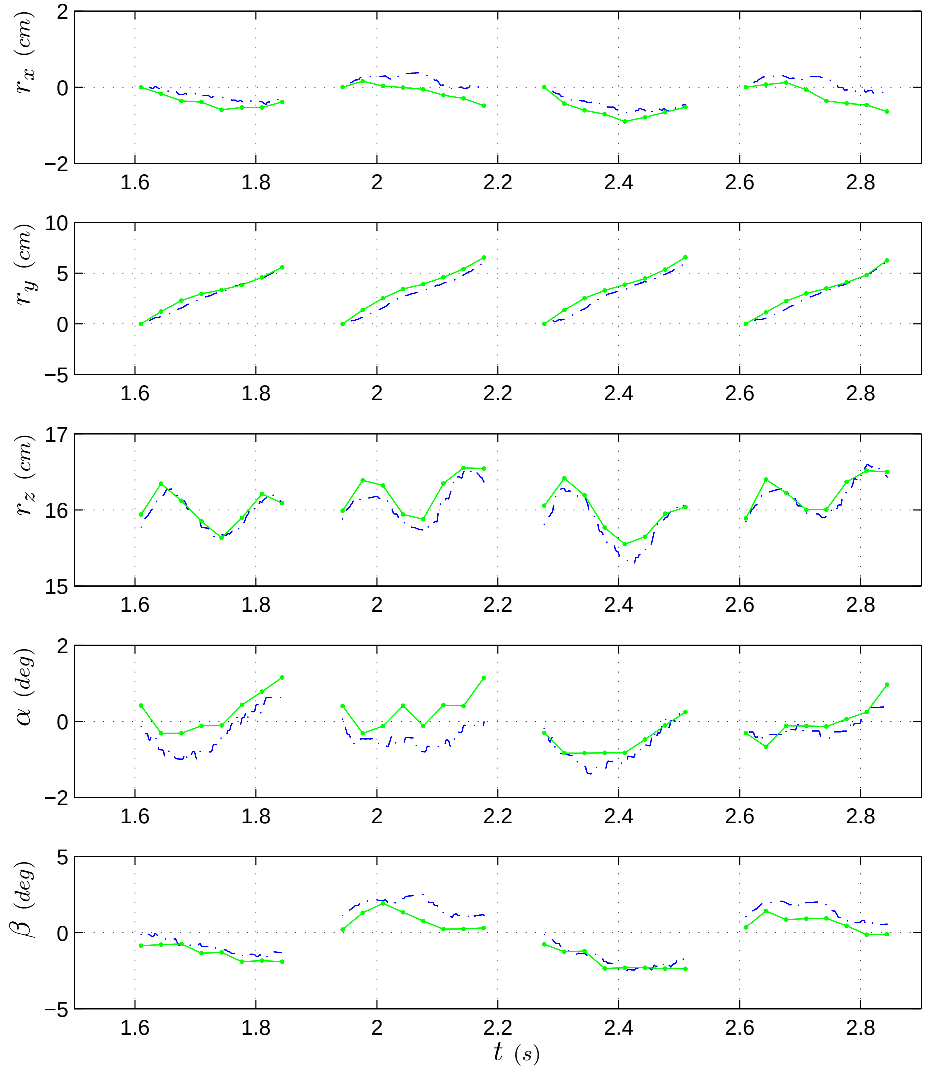

Figure 4.8: Pose states measured by GTMS (solid line) and computed according to our algorithm (dashdot line) for single stance body pose computation.

4.4 Short Discussion

We have introduced a continuous-time full body pose estimator for a hexapod robot based on the kinematic configuration of its legs suitable for robot operating in the following two conditions: A) the body is supported by at least three legs with non-collinear toes at any given time; and B) ground contact legs have no toe slippage. The algorithm is structured in a two layer hierarchy: the lower layer relates leg configuration to body pose within a single stance while the higher layer recursively composes consecutive single stance measurements to achieve complete legged odometry —continuous pose computation across multiple steps. We have implemented this algorithm on the robot RHex [SBK01] utilizing strain measurements of its 4-bar legs [Moo01] linked over a wireless communications network [Kom05][6].

Using a high speed visual ground truth measurement system, we have shown that the leg configuration model used to interpret the strain data achieves very high accuracy in realistic operating conditions, e.g. effective length errors of less than 2%. Using a separate conventional frame rate visual ground truth measurement system we have evaluated the performance of the resulting low level single stance pose estimator and the high level legged odometry system at various speeds and conditions of surface friction. The body pose estimator is shown to perform well at all speeds over normal ground conditions—achieving, for example, five times more accurate legged odometry than computed from averaged open loop distance-per-stride estimates. The estimator continues to function well over a variety of ground conditions, with the onset of significant performance degradation on the most slippery surfaces like soaped plastic, whose coefficient of friction is less than a third that of normal linoleum.

In its present form, the pose computation algorithm cannot function if the operating regime includes an aerial phase as is typical of RHex's most useful dynamical gaits [Sar02]. To remedy this shortcoming in Chapter 5 we introduce the "Advanced Inertial Measurement Unit" composed by linear accelerometers and rotational rate gyroscopes to complement the body pose sensor derived from leg kinematic configuration introduced here. This multiple array of sensor modalities will not only allow us to perform pose estimation during aerial phases but also enable us to detect and correct errors resulting from slippage, the primary source of inaccuracy in the present sensor.

[6] Note that, in consequence of RHex's constrained kinematics, as explained in Section 4.3, we have not exercised its yaw degree of freedom in this study.

CHAPTER 5

Advanced Inertial Measurement Unit

This chapter introduces a framework to construct an advanced inertial measurement unit delivering linear and angular acceleration as well as angular velocity through the construction of a novel 12-axis accelerometer suite. The additional angular acceleration data generated by the advanced IMU coupled with the linear acceleration and angular velocity from a traditional IMU builds a stronger foundation of sensor data fusion for better state estimation. In addition to the inertia force derived by the accelerometers through the traditional IMU, the new system also delivers information of inertia torque acting on the body, thus completing force/torque information in a physical second order dynamical system. We implement this advanced inertial measurement system on RHex's body to deliver COM translational state and body rotational state as detailed in Chapter 6.

Section 5.1 briefly reviews previous related work on angular acceleration measurements, followed by Section 5.2 introducing 3-dimensional coupled calibration which improves the accuracy of measurement on practical implementation. Section 5.3 describes the methodology, characteristics, and initial experimental results of this 12-axis accelerometer suite.

5.1 Previous Related Work on Linear and Angular Acceleration Measurement

The most direct way to obtain 6 DOF linear and angular acceleration estimates, $\mathbf{a}_{COM}$ and $\dot{\omega}$, is to measure linear acceleration by accelerometers implemented according to Figure 5.1(a). The green solid arrows represent three 1-axis accelerometers installed orthogonally at COM, also the origin of body frame, and three 1-axis accelerometers installed on the principle axes and oriented in specific directions. The result is derived from the equation[1]:

[1] 6 DOF acceleration can also be calculated if the whole six 1-axis accelerometer suite is "shifted" away from COM. However, in this case linear acceleration, $\mathbf{a}_{COM}$, will also be a function of angular velocity.

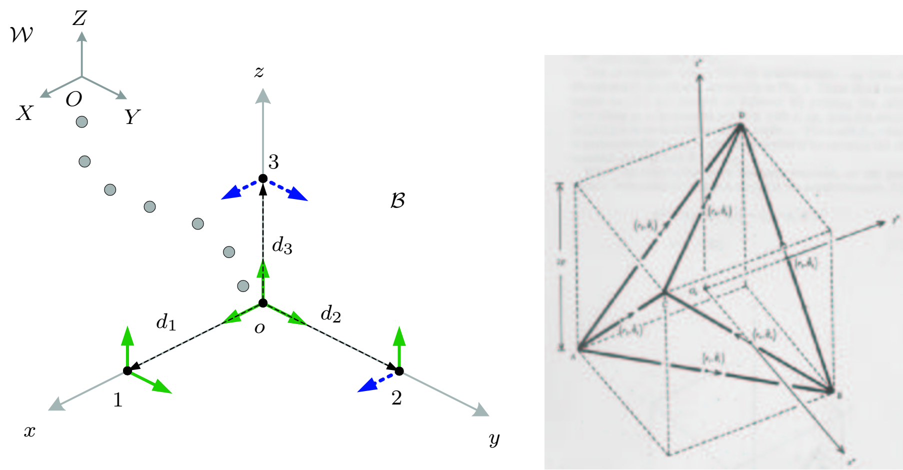

(a) (b)

Figure 5.1: (a) 6-axis accelerometer suite (green arrows) and 9-axis accelerometer suite (green and blue arrows); (b) 6-axis accelerometer IMU proposed by DeBra [CLD94]

$$
\begin{aligned}
\mathbf{a}_{COM} &= \begin{bmatrix} a_{ox} & a_{oy} & a_{oz} \end{bmatrix}^T \\
\dot{\omega}_x &= (a_{2z} - a_{oz})/d_2 - \omega_y \omega_z \\
\dot{\omega}_y &= -(a_{1z} - a_{oz})/d_1 + \omega_x \omega_z \\
\dot{\omega}_z &= (a_{1y} - a_{oy})/d_1 - \omega_x \omega_y.
\end{aligned}
\tag{5.1}
$$

Deriving linear acceleration is straight forward, and angular acceleration can be derived by obtaining angular velocity by integration with given initial conditions prior to plugging it into (5.1). However, in a physical implementation the unbounded drifting error in angular velocity due to numerical integration rapidly deteriorates the accuracy of angular acceleration measurement. Consequently, King proposed to use a 9-axis accelerometer suite [PKK75], green solid arrows plus blue dashed arrows shown in Figure 5.1(a), to construct the IMU, generating another three equations for angular acceleration computation:

$$
\begin{aligned}
\dot{\omega}_x &= -(a_{3y} - a_{oy})/d_3 + \omega_y \omega_z \\
\dot{\omega}_y &= (a_{3x} - a_{ox})/d_3 - \omega_x \omega_z \\
\dot{\omega}_z &= -(a_{2x} - a_{ox})/d_2 + \omega_x \omega_y.
\end{aligned}
\tag{5.2}
$$

The summation of (5.1) and (5.2) eliminates the crossterms of angular velocity, resulting in a pure input output kinematic mapping from sensor data to 6 DOF acceleration measure:

$$
\begin{aligned}
\dot{\omega}_x &= (a_{2z} - a_{oz})/d_2 - (a_{3y} - a_{oy})/d_3 \\
\dot{\omega}_y &= (a_{3x} - a_{ox})/d_3 - (a_{1z} - a_{oz})/d_1 \\
\dot{\omega}_z &= (a_{1y} - a_{oy})/d_1 - (a_{2x} - a_{ox})/d_2.
\end{aligned}
\tag{5.3}
$$

Following the idea of eliminating the crossterms, DeBra proposed the gyro free IMU [CLD94] shown in Figure 5.1(b) with six 1-axis accelerometers installed on three principle axes with equal distance to the origin, ρ, and oriented in specific directions. In this special arrangement angular acceleration is a function of accelerometer measurements ($a_k,\ _{k=1\sim6}$) and ρ only. However, the downside of obtaining stable angular acceleration measure with three less 1-axis accelerometers than proposed by King is instability in linear acceleration due to its dependency on angular velocity:

$$
\begin{aligned}
\mathbf{a}_{COM} &= g_{6l}(a_k, \rho, \omega_i\omega_j)\ _{k=1\sim6}\ ,\ _{i,j=1,2,3} \\
\dot{\omega} &= g_{6r}(a_k, \rho).
\end{aligned}
\tag{5.4}
$$

As a result, the 9-axis accelerometer suite seems to be the minimum number of accelerometers to obtain a stable solution for full 6 DOF acceleration measurement. However, in using King's method, the critical constraint on locations for accelerometer installation, 3 at COM and 6 along principle axes[2], as well as the practical problem of accuracy of measurement direction, detailed in the following Section 5.2, inevitably limit the feasibility of the practical implementation.

5.2 Coupled Calibration

Theoretically, acceleration along a specific direction—usually the principle axis of the body frame; ex: a_z—can be obtained by a 1-axis accelerometer τ_3', installed on the body frame as shown in Figure 5.2(a) with known body orientation—α, β, and γ—utilized to eliminate the influence of the gravity force. From the reverse point of view, the sensor reading τ_3', depends on body orientation and acceleration along that specific direction only (ex: a_z). However, in a practical implementation the misalignment shown in Figure 5.2(a) between desired and measured directions of acceleration due to installation error causes that the sensor reading, τ_i, is linearly dependent on the acceleration along all three principle axes:

$$
\tau_i = g_i(a_x, a_y, a_z, \alpha, \beta, \gamma)\ _{i=1,2,3}. \tag{5.5}
$$

For this reason, in the general case, a 3 DOF acceleration reading is required ($\tau_i,\ _{i=1,2,3}$) for a single acceleration along a specific direction (ex:a_z). If only one accelerometer measurement is applied, the acceleration measurement in the specified direction will be contaminated by the acceleration in the remaining two directions. This practical concern motivates us to use

[2]We cannot "shift" this 9-axis accelerometer suite away from the COM since this causes $\mathbf{a}_{COM}$ to be a function of angular velocity, which conflicts with the main idea of eliminating angular velocity in the computational process.

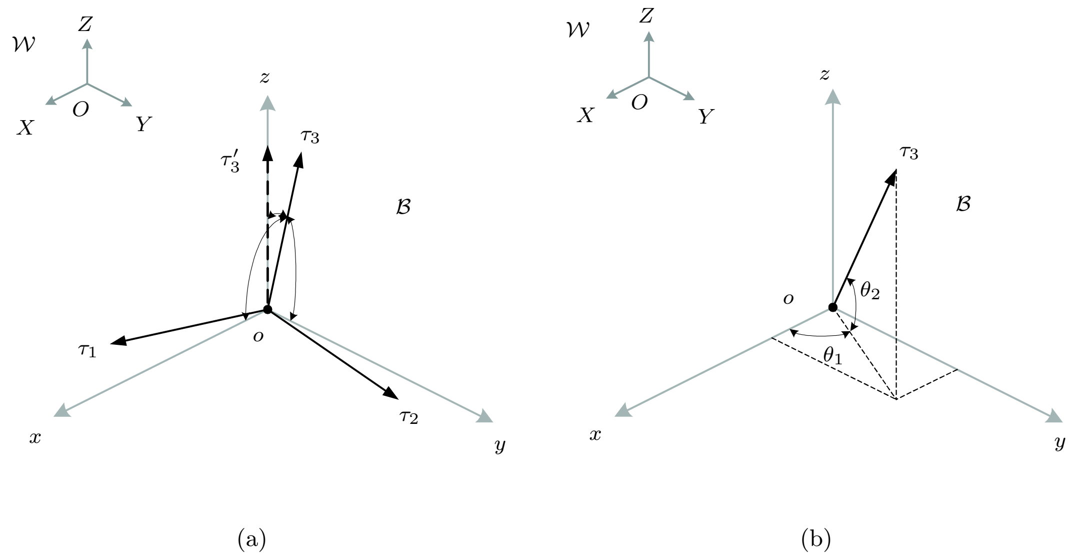

Figure 5.2: (a) Sketch of misalignment between an accelerometer measuring directions—τ_1, τ_2, and τ_3—and the principle axes; (b) Sketch of an acceleration measurement along z by a misaligned accelerometer τ_3

a 3-axis accelerometer suite as the "basic unit" for acceleration measurement, which allows us to construct a 3 DOF coupled mapping from sensor space to orthogonal acceleration space along three principle axes $\mathbf{a}_k$ with known body orientation, expressed in the general form:

$$\mathbf{a}_k = \begin{bmatrix} a_x & a_y & z_z \end{bmatrix}^T = g_{ortho}(\tau_1, \tau_2, \tau_3, \alpha, \beta, \gamma). \tag{5.6}$$

This function $g_{ortho}(\bullet)$ contains three operations: first, linear coupled 3×3 mapping of acceleration from directions along sensors to that along principle axes; second, rotation operator to rotate coordinates of acceleration from body frame to world frame; and third, remove the acceleration due to gravity.

Considering the case that acceleration a_z is measured by only one misaligned 1-axis accelerometer τ_3 pointing $(cos\theta_2 cos\theta_1, cos\theta_2 sin\theta_1, sin\theta_2)$, spherical coordinates represented in cartesian coordinates, shown in Figure 5.2(b), the percentage error of measuring a_z is given by

$$\frac{(a_x cos\theta_2 cos\theta_1 + a_y cos\theta_2 sin\theta_1 + a_z sin\theta_2) - a_z}{a_z} \times 100$$

In the case, $\theta_1 = 45^o$, $\theta_2 = 85^o$ (only 5^o misalignment) and $a_x = a_y = a_z$ which indicates that acceleration has the same range along with three orthogonal components, the percentage error is 11.9%. The error will increase greatly when the range of acceleration due to motion is much less then that due to gravity. For example, if $\theta_1 = 45^o$, $\theta_2 = 85^o$ (the same, only 5^o misalignment) and $a_x = 5a_y = 5a_z$ which assumes gravity is along the direction of a_x and the range of acceleration due to motion is only 20 % of gravity, then the percentage error goes up to 36.5%. This shows the importance of adopting a 3-axis accelerometer suite at any measurement point, and further explains the practical challenge of implementing the 9-axis accelerometer suite proposed by King detailed in Section 5.1.

5.3 Linear and Angular Acceleration as well as Angular Velocity from a 12-Axis Accelerometer Suite

The traditional IMU consisting of a 3-axis accelerometer installed at the COM and a 3-axis gyro on the body delivers COM linear acceleration ($\ddot{r_x}$, $\ddot{r_y}$, and $\ddot{r_z}$) and body angular velocity ($\dot{\alpha}$, $\dot{\beta}$, and $\dot{\gamma}$) in 6 independent dimensions. In order to obtain angular acceleration data ($\ddot{\alpha}$, $\ddot{\beta}$, and $\ddot{\gamma}$) as an input to a complete second order dynamical model for a rotational state, we propose a general method that algebraically computes six independent translational and rotational acceleration measurements as well as three independent angular velocity measurements from a 12-axis accelerometer suite using the kinematic relationships of rigid body motion as follows.

5.3.1 Methodology

The acceleration vector $\mathbf{a}_p$, in an inertial "world" frame of a point, p, rigidly attached to an accelerating "body" frame with origin, o, is a function of the body's angular velocity, ω, and angular acceleration, $\dot{\omega}$, as well as the translational acceleration of the origin, $\mathbf{a}_o$, of the body frame given by

$$\mathbf{a}_p = \mathbf{a}_o + \dot{\omega} \times \mathbf{r}_{op} + \omega \times (\omega \times \mathbf{r}_{op}), \qquad (5.7)$$

where $\mathbf{r}_{op}$, the fixed location of p relative to the body, is presumed known á priori. In general, we are interested in the motion of the body relative to the world, hence we seek to extract from measurements, the left hand quantities shown in (5.7), to derive the right side unknowns: the COM translational acceleration[3],

$$\mathbf{a}_{COM} = \mathbf{a}_o = \begin{bmatrix} \ddot{r_x} & \ddot{r_y} & \ddot{r_z} \end{bmatrix}^T,$$

and the angular acceleration and velocity,

$$\begin{aligned} \dot{\omega} &= \begin{bmatrix} \ddot{\alpha} & \ddot{\beta} & \ddot{\gamma} \end{bmatrix}^T \\ \omega &= \begin{bmatrix} \dot{\alpha} & \dot{\beta} & \dot{\gamma} \end{bmatrix}^T = \begin{bmatrix} \omega_1 & \omega_2 & \omega_3 \end{bmatrix}^T. \end{aligned}$$

[3]The original of body frame is usually assigned at the COM.

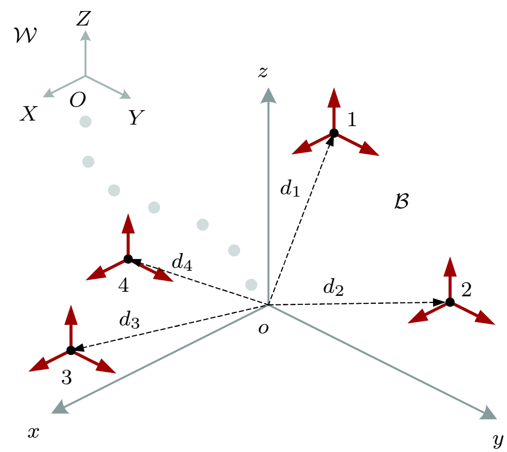

Figure 5.3: 12-axis accelerometer suite - measuring 3 DOF acceleration in 4 locations on robot body frame (brown thick arrows denote the acceleration to be measured)

Note that the latter variable appears in a quadratic form, hence (5.7) defines a function that is linear in the six unknowns, $\mathbf{a}_{COM}$, $\dot{\omega}$, and linear in

$$q(\omega) = \left[\begin{array}{cc} \omega_i^2 + \omega_j^2 & \omega_i\omega_j \end{array}\right]^T_{i<j \ in \ 1,2,3}, \tag{5.8}$$

the six distinct second degree monomials of $\omega \times \omega$ formed from the three unknowns of ω. In Section 5.3.4 we show how to invert the quadratic map q from ω to $\omega \times \omega$, thereby establishing that the determination of the nine unknowns in (5.7) reduces to a linear computation that we will proceed to detail—at the expense of requiring the increase of three additional measurements beyond the nine intrinsic dimensions of the data.

The proposed accelerometer suite depicted in Figure 5.3 yields a 12-dimensional vector of measurements,

$$\mathbf{a}_s \quad := \quad \left[\begin{array}{cccc} \mathbf{a}_1^T & \mathbf{a}_2^T & \mathbf{a}_3^T & \mathbf{a}_4^T \end{array}\right]^T$$

comprised of four distinct spatial acceleration vectors, following upon a very simple coupled calibration procedure from raw accelerometer outputs detailed in Section 5.2,

$$\mathbf{a}_k := \left[\begin{array}{ccc} a_{kx} & a_{ky} & a_{kz} \end{array}\right]^T_{k=1,2,3,4}, \tag{5.9}$$

obtained at the four locations specified by the position vectors,

$$d := \left[\begin{array}{cccc} d_1^T & d_2^T & d_3^T & d_4^T \end{array}\right]^T \in R^{12}.$$

In each case, $k = 1, 2, 3, 4$, the measured acceleration vector, $\mathbf{a}_k$, is linearly related to the twelve unknowns

$$\mathbf{x}_{var} \;=\; \left[\begin{array}{ccc} \mathbf{a}_{COM}^T & \dot{\omega}^T & q(\omega)^T \end{array}\right]^T \tag{5.10}$$

by a copy of (5.7) where the role of $\mathbf{r}_{op}$ is played by d_k, giving rise to the 12×12 linear system of equations

$$\mathbf{a}_s = \mathbf{C}(d)\mathbf{x}_{var}, \tag{5.11}$$

or in the expanded matrix form:

$$\begin{bmatrix} a_{1x} \\ a_{1y} \\ a_{1z} \\ a_{2x} \\ a_{2y} \\ a_{2z} \\ a_{3x} \\ a_{3y} \\ a_{3z} \\ a_{4x} \\ a_{4y} \\ a_{4z} \end{bmatrix} = \begin{bmatrix} 1 & 0 & 0 & 0 & d_{1z} & -d_{1y} & 0 & 0 & -d_{1x} & d_{1y} & d_{1z} & 0 \\ 0 & 1 & 0 & -d_{1z} & 0 & d_{1x} & 0 & -d_{1y} & 0 & d_{1x} & 0 & d_{1z} \\ 0 & 0 & 1 & d_{1y} & -d_{1x} & 0 & -d1z & 0 & 0 & 0 & d_{1x} & d_{1y} \\ 1 & 0 & 0 & 0 & d_{2z} & -d_{2y} & 0 & 0 & -d_{2x} & d_{2y} & d_{2z} & 0 \\ 0 & 1 & 0 & -d_{2z} & 0 & d_{2x} & 0 & -d_{2y} & 0 & d_{2x} & 0 & d_{2z} \\ 0 & 0 & 1 & d_{2y} & -d_{2x} & 0 & -d2z & 0 & 0 & 0 & d_{2x} & d_{2y} \\ 1 & 0 & 0 & 0 & d_{3z} & -d_{3y} & 0 & 0 & -d_{3x} & d_{3y} & d_{3z} & 0 \\ 0 & 1 & 0 & -d_{3z} & 0 & d_{3x} & 0 & -d_{3y} & 0 & d_{3x} & 0 & d_{3z} \\ 0 & 0 & 1 & d_{3y} & -d_{3x} & 0 & -d3z & 0 & 0 & 0 & d_{3x} & d_{3y} \\ 1 & 0 & 0 & 0 & d_{4z} & -d_{4y} & 0 & 0 & -d_{4x} & d_{4y} & d_{4z} & 0 \\ 0 & 1 & 0 & -d_{4z} & 0 & d_{4x} & 0 & -d_{4y} & 0 & d_{4x} & 0 & d_{4z} \\ 0 & 0 & 1 & d_{4y} & -d_{4x} & 0 & -d4z & 0 & 0 & 0 & d_{4x} & d_{4y} \end{bmatrix} \begin{bmatrix} \ddot{r_x} \\ \ddot{r_y} \\ \ddot{r_z} \\ \ddot{\alpha} \\ \ddot{\beta} \\ \ddot{\gamma} \\ \dot{\alpha}^2 + \dot{\beta}^2 \\ \dot{\alpha}^2 + \dot{\gamma}^2 \\ \dot{\beta}^2 + \dot{\gamma}^2 \\ \dot{\alpha}\dot{\beta} \\ \dot{\alpha}\dot{\gamma} \\ \dot{\beta}\dot{\gamma} \end{bmatrix}.$$

Since d is known á priori, the extraction of the desired acceleration and angular velocity data, $\mathbf{x}_{var}$, now hinges upon the rank and numerical condition of the "structure" matrix, $\mathbf{C}(d)$.

We observe that the determinant of the 12×12 matrix $\mathbf{C}(d)$, $det(\mathbf{C}(d))$, is given by the determinant of the "sensor simplex" array, $det(D)$:

$$det(\mathbf{C}(d)) = (2det(D))^3 \tag{5.12}$$

where $D := \left[\begin{array}{ccc} d_2 - d_1 & d_3 - d_1 & d_4 - d_1 \end{array}\right]$. Hence, so long as the accelerometer suite of Figure 5.3 defines a spatial tetrahedron with non-zero volume[4], it provides in principle a complete IMU—a means of extracting full rigid body acceleration and velocity data with no recourse to rate gyros.

In practice, we have found that the numerical condition of $\mathbf{C}(d)$ is very sensitive to the "shape" and "size" of the tetrahedron and its relative location to COM. Numerical exploration quickly reveals that useful numerical inverses, $\mathbf{C}^{-1}(d)$, are obtained when all four 3-axis accelerometer suites are installed with specific geometric relations to each other and with certain distances to the COM. Unfortunately, the numerical condition of $\mathbf{C}(d)$

[4]That is, the four accelerometers are in general position so there is no co-planar subset of any three of them

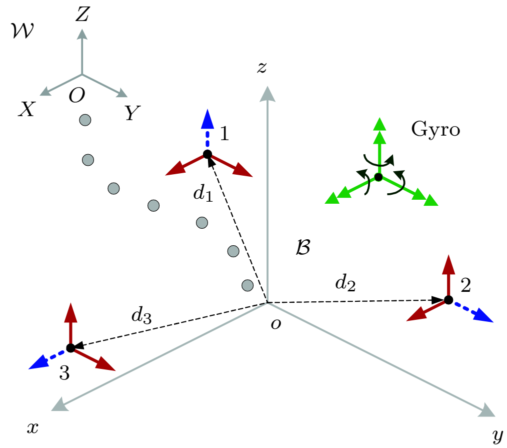

Figure 5.4: 9-axis accelerometer suite with gyro —measuring 3 DOF acceleration in 3 locations (brown thick arrows and blue dashed arrows denote the acceleration to be measured) as well as 3 DOF angular velocity (green thick double arrows) on the robot body frame

degenerates rapidly as any edge of the tetrahedron is shortened below unit length (meter). In particular, as we detail in Section 5.3.2, the largest volume tetrahedra inscribed within RHex's rectangular body yields very stiff structure matrices, $\mathbf{C}(d)$, whose large singular values are associated with the translational and rotational acceleration components of $\mathbf{x}_{var}$ and with uselessly small singular values associated with the rotational velocity components, $q(\omega)$, of $\mathbf{x}_{var}$. Consequently, in this investigation we rely upon measurements of ω arising from a MEMS gyro retaining only the acceleration components, $\mathbf{a}_{COM}$ and $\dot{\omega}$, of the accelerometer suite's estimate for $\mathbf{x}_{var} = \mathbf{C}^{-1}(d)\mathbf{a}_s$.

Since in current practical implementation we need the extra 3-axis gyro to provide angular velocity data due to an ill -structured matrix, we attempt an alternate method of applying 6-axis accelerometer suite data and 3-axis gyro data into (5.7) to construct a new 6×6 structure matrix in order to solve linear and angular acceleration:

$$\mathbf{a}_p - \omega \times (\omega \times \mathbf{r}_{op}) = \mathbf{a}_o + \dot{\omega} \times \mathbf{r}_{op}, \tag{5.13}$$

or in the expanded matrix form:

$$\begin{bmatrix} a_{1x} + d_{1x}(\dot{\beta}^2 + \dot{\gamma}^2) - d_{1y}(\dot{\alpha}\dot{\beta}) - d_{1z}(\dot{\alpha}\dot{\gamma}) \\ a_{1y} + d_{1y}(\dot{\alpha}^2 + \dot{\gamma}^2) - d_{1x}(\dot{\alpha}\dot{\beta}) - d_{1z}(\dot{\beta}\dot{\gamma}) \\ a_{1z} + d_{1z}(\dot{\alpha}^2 + \dot{\beta}^2) - d_{1x}(\dot{\alpha}\dot{\gamma}) - d_{1y}(\dot{\beta}\dot{\gamma}) \\ a_{2x} + d_{2x}(\dot{\beta}^2 + \dot{\gamma}^2) - d_{2y}(\dot{\alpha}\dot{\beta}) - d_{2z}(\dot{\alpha}\dot{\gamma}) \\ a_{2y} + d_{2y}(\dot{\alpha}^2 + \dot{\gamma}^2) - d_{2x}(\dot{\alpha}\dot{\beta}) - d_{2z}(\dot{\beta}\dot{\gamma}) \\ a_{2z} + d_{2z}(\dot{\alpha}^2 + \dot{\beta}^2) - d_{2x}(\dot{\alpha}\dot{\gamma}) - d_{2y}(\dot{\beta}\dot{\gamma}) \end{bmatrix} = \begin{bmatrix} 1 & 0 & 0 & 0 & d_{1z} & -d_{1y} \\ 0 & 1 & 0 & -d_{1z} & 0 & d_{1x} \\ 0 & 0 & 1 & d_{1y} & -d_{1x} & 0 \\ 1 & 0 & 0 & 0 & d_{2z} & -d_{2y} \\ 0 & 1 & 0 & -d_{2z} & 0 & d_{2x} \\ 0 & 0 & 1 & d_{2y} & -d_{2x} & 0 \end{bmatrix} \begin{bmatrix} \ddot{r_x} \\ \ddot{r_y} \\ \ddot{r_z} \\ \ddot{\alpha} \\ \ddot{\beta} \\ \ddot{\gamma} \end{bmatrix}.$$

This new matrix is only nonsingular if the 6-axis acceleration are measured from at least three locations[5]. However, this indicates that the coupled calibration detailed in Section 5.2 used to compensate the misaligned installation error is not feasible unless another 3-axis acceleration measure, total 9, is implemented as shown in Figure 5.4 with brown thick arrows and blue dashed arrows. In this situation we prefer to install yet another 3-axis acceleration measure, total 12, to let the derivation of linear and angular acceleration remain independent of gyro measurement. We can now treat angular acceleration and velocity as two independent sensing data to be imported into the EKF detailed in Section 6.3.1.

5.3.2 Structure Matrix $\mathbf{C}(d)$

Without loss of generality, imagine the shape of the robot body as a "rectangular prism" and the availability of space inside it. Numerical exploration reveals the condition number of the structure matrix, $\mathbf{C}(d)$, is minimized when four 3-axis accelerometer suites occupy 4 of 8 corners of this prism and when the geometrical center of the prism coincides with the COM. We also observe that the condition number is mainly determined by the shortest edge of the prism, and increases rapidly as the prism shrinks. It achieves the minimum ($\sqrt{2}$) when four 3-axis accelerometer suites located (in Cartesian coordinate, unit:meter if using MKS) as follows:

$$\begin{bmatrix} d_1^T \\ d_2^T \\ d_3^T \\ d_4^T \end{bmatrix} = \begin{bmatrix} -1 & -1 & -1 \\ -1 & 1 & 1 \\ 1 & -1 & 1 \\ 1 & 1 & -1 \end{bmatrix}, \tag{5.14}$$

also shown in Figure 5.5(a), and it goes up from $\sqrt{2}$ to $\{2, 4, 8, 16\}$ when the edge of "cube" goes down from 2 to $\{1, 0.5, 0.25, 0.125\}$.

The "best" condition number can be achieved in RHex's size, 25cm x 50cm x 15 cm, is $13\frac{1}{3}$. However, the practical implementation of the accelerometer suite within the limited available space left in RHex, as well as having been designed to keep COM low, thereby not matching the geometrical center, for stability, yields the high condition number of 41 in its current setup as shown in Figure 5.5(b). From Singular Value Decomposition of the structure matrix $\mathbf{C}(d)$, we observe that the subspaces spanned by small singular values point mostly to the last 4 elements on the unknown vector $\mathbf{x}_{var}$ in (5.11) resulting in the deterioration of the estimation of angular velocity. Therefore, in the practical implementation on RHex we inevitably adopt the gyro's output as the only data source of angular velocity, ω_g, to complete this advanced IMU.

[5]One example is shown in Figure 5.4 (brown thick arrows); another example is shown in Figure 5.1(a) (green solid arrows) detailed in Section 5.1.

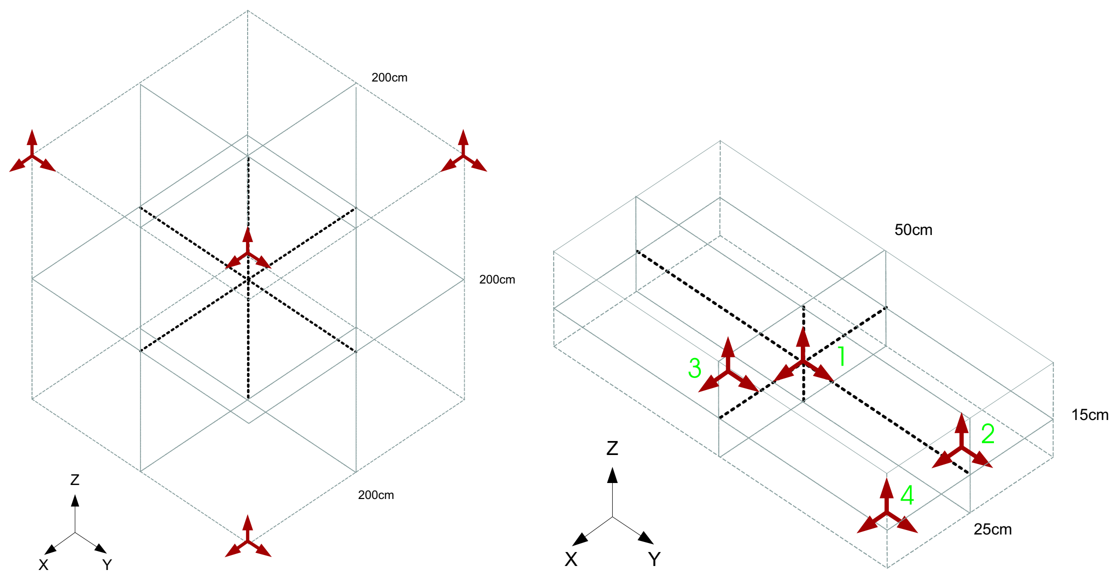

(a) (b)

Figure 5.5: Ideal and practical locations of the 12-axis accelerometer suite: (a) Sketch of ideal locations of the 12-axis accelerometer suites; (b) Sketch of actual locations of 12-axis accelerometer suites implemented on RHex (Thick dashed lines indicate principle axes)

5.3.3 Performance of Angular Acceleration from 12-Axis Accelerometer Suite

The practical implementation of a 12-axis accelerometer suite on RHex yields good linear and angular acceleration data but poor angular velocity data due to an ill conditioned structure matrix determined by the relative locations of accelerometers, which are constrained by the physical size of RHex. Therefore, in this section we will focus on the performance of angular acceleration derived from a 12-axis accelerometer suite by directly integrating the data and comparing it to the angular velocity data from the gyro. Figure 5.6, a typical run of robot locomotion, clearly shows the matching of two curves—one from integration of angular acceleration (cyan dashed-dot line), and the other from direct measure of gyro (magenta solid line). The well-matched high frequency components, slopes of the curve, indicate the correct estimate of angular acceleration derived from measured linear acceleration, and the drift of the cyan dashed-dot curve also reveals the typical accumulation error due to integration. This additional valuable information provides us with an independent channel for data fusion in order to provide better estimates of orientation state. The performance comparison of the systems with or without angular acceleration and with or without body pose sensor as sensory feedbacks will be detailed in Section 6.4.2.

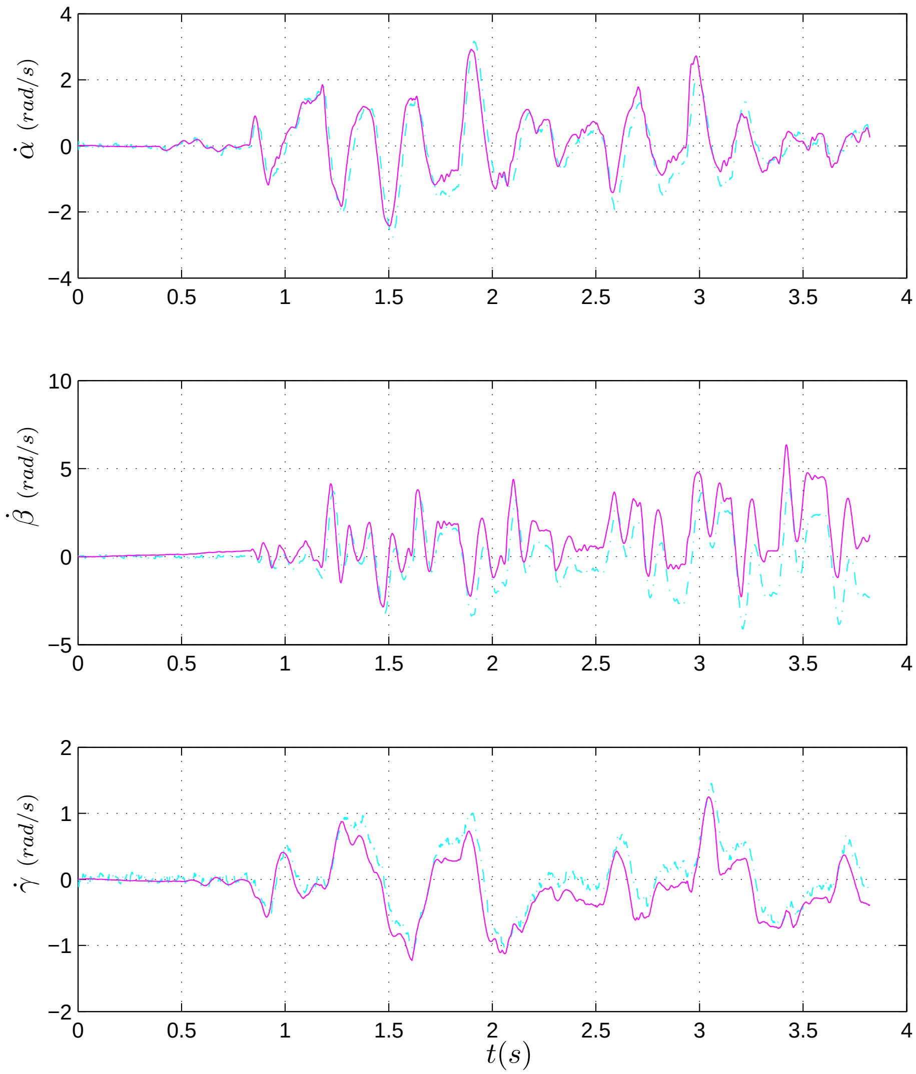

Figure 5.6: Angular velocity measured by gyro (solid line) and computed by integration of angular acceleration data from the 12-axis accelerometer suite (dashdot line)

5.3.4 Angular Velocity from a 12-Axis Accelerometer Suite

The process to obtain an invertible mapping for this quadratic system from $\omega \times \omega$ to ω cannot be solved kinematically by the six available equations alone since there exists at least one sign ambiguity for the unknowns. However, this is derivable with given the initial condition as well as, with the availability of angular acceleration derived from the other six equations in the same 12-axis accelerometer suite. Without loss of generality, assuming at time t_i the state of angular acceleration and angular velocity are available, the procedure to solve angular velocity at t_{i+1} is as follows: First, derive "estimated" angular velocity by angular velocity and angular acceleration at t_i using a constant acceleration model—$\omega_i(t_{i+1}) = \omega_i(t_i) + \dot{\omega}_i(t_i) * (t_{i+1} - t_i)$. Second, adopt the sign of this estimated angular velocity as the correct sign identification for angular velocity at t_{i+1}. Finally, choose three scalar components from solved $q(\omega)$, either $\omega_i \omega_j$ or $\omega_i^2 + \omega_j^2$ where $i < j; i, j = \{1, 2, 3\}$, to solve angular velocity (ω), or combine both to construct a complete square—$(\omega_i^2 + \omega_j^2) + 2\omega_i \omega_j = (\omega_i + \omega_j)^2$, and solve the "fused" angular velocity. Theoretically, no matter which three scalar components we select, it should yield the same angular velocity. In practice the existence of noise may deteriorate the measurement which further suggests the advantage of using the "fused" solution from all six components.

CHAPTER 6

Sensor Data Fusion for Body State Estimation with Dynamical Gaits

This chapter introduces a hybrid 12-dimensional full body state estimator for a hexapod robot executing a dynamical gait in steady state on level terrain. We will focus on alternating tripod jogging gaits because of its familiarity and importance in RHex, but the computations below generalize to a family of gaits characterized by two conditions: A) regularly alternating ground contact and aerial phases of motion; B) when in stance, the body is supported by at least three legs with non-collinear toes without toe slippage[1]. We use a repeating sequence of continuous time dynamical models that are switched in and out of an Extended Kalman Filter to fuse measurements from a body pose sensor detailed in Chapter 4 and an advanced inertial measurement unit detailed in Chapter 5.

Section 6.1 introduces notation and illustrates the nature of the open loop stabilizing ("jogging") gait [WLK04] we will study. Section 6.2 summarizes the acquisition of partial state (body pose from a leg pose sensor; linear/angular acceleration and angular velocity from advanced IMU) from raw sensor data. Section 6.3 describes the various dynamical models in each phase of a stride from which we construct our statistical filters for full body state along with the details of how to fuse the two independent sensing sources (leg pose sensor and IMU) summarized in Section 6.2. Section 6.4 examines the accuracy of the resulting body state estimator implemented on RHex.

6.1 Dynamical Locomotion (Jogging Gait)

Determining the right dynamical model for the jogging gait promises to be a complicated task since the physical robot acts as a Lagrangian system with 3^6 different models depending on touchdown-stick/touchdown-slip/liftoff conditions on each leg. Lacking sensing ability to detect toe slippage as well as unknown stability condition under fast switching among a large number of models, we defer the fundamental problem of estimator model selection and

[1] As mentioned before, this condition guarantees that the toe contacts yield a well defined coordinate system fixed in the world frame in order to derive body pose from leg configuration detailed in Chapter 4.

switching discussed above by recoursing to a succession of intuitively appropriate dynamical representations of the "virtual biped" that emerges from well tuned jogging controllers [WLK04]. We introduce three distinct models in four successively repeating phases—tripod stance phase, liftoff transient phase, aerial phase, and touchdown transient phase.

Consider the typical sequence of leg contact conditions, depicted in the lower half of Figure 6.1 that occurs during steady state operation in stable dynamical locomotion. During the i^{th} stride interval, $D(i){:=}[t_1(i)\ \ t_5(i)]{\subset}R$, a tripod stance interval, $\Upsilon_S(i){:=}[t_1(i)\ \ t_2(i)]$, is succeeded by a period of time when the legs begin to liftoff, $\Upsilon_L(i){:=}[t_2(i)\ \ t_3(i)]$, followed by an interval of aerial flight, $\Upsilon_A(i){:=}[t_3(i)\ \ t_4(i)]$, then touching down through another period of varied leg contacts, $\Upsilon_T(i){:=}[t_4(i)\ \ t_5(i)]$, to the fixed tripod stance interval $\Upsilon_S(i{+}1)$ of the next stride, $D(i{+}1)$. We conceive of the liftoff and touchdown intervals, $\Upsilon_L(i)$ and $\Upsilon_T(i)$, as "transients" because they typically exhibit complex sequences of successive leg contacts that reveal little consistent pattern from run to run (or, often, even from stride to stride). In practical implementation, the crucial leg contact information required to detect the onset and termination of each of these phases of a stride may be gleaned directly from the individual leg touchdown/configuration sensors. The upper half of Figure 6.1 shows the relation between these four phases and leg positions of two tripods generated by a custom Buehler Clock [SBK01] from our practical implementation on RHex.

With only one active DOF on each leg, the standard way to generate a continuous time jogging gait in RHex is to operate the clock of leg rotation of two tripods with 180^o offset in the custom Buehler Clock [SBK01] detailed in Appendix D. This clock is comprised of slow rotation period for ground contact and a quick return period to maintain continuous locomotion (small slope and large slope accordingly in top part of Figure 6.1). The aerial phases occur between previous just-lifted tripod and next going-to touchdown tripod. Practically, of course, three legs of each tripod would not liftoff and touchdown at the same time, resulting in the existence of transients with one or two legs contacting the ground between those two phases (thin lines between thick lines in Figure 6.1).

6.2 Partial State Directly from Sensor

This section briefly introduces the methodology of obtaining partial state directly from raw sensor data before being imported into a filter to recover the full state.

6.2.1 Body Pose from Leg Configuration Sensor

Full 6 DOF body pose (COM displacement in lateral(r_x), fore/aft (r_y), vertical (r_z) directions and body orientation in pitch (α), roll (β), and yaw (γ)) for a hexapod robot in each tripod stance can be derived from a novel leg configuration measurement system detailed in Section 3.6 and Section 4.1.1 by using a conventional (memoryless) kinematic model generally expressed in the form:

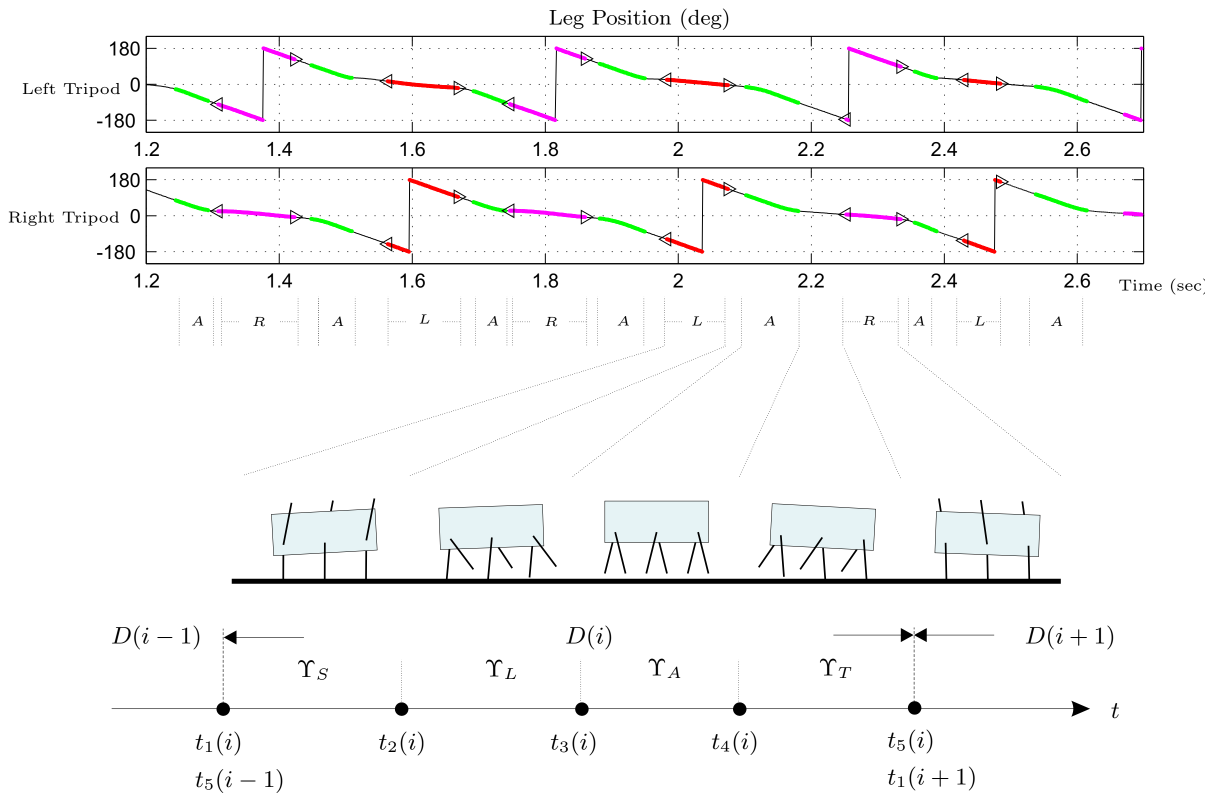

Figure 6.1: Conceptual diagram of four consecutive intervals during the i^{th} jogging stride, $D(i)$, with figure on top showing the relation between leg positions (0^o = vertically downward; $\pm 180^o$ = vertical upward) and four phases (intervals) collected from practical RHex experimental data—aerial phase ($|A|$); left tripod stance phase ($\vdash L \dashv$, between $\triangleleft\ \triangleright$); right tripod stance phase ($\vdash R \dashv$, between $\triangleleft\ \triangleright$); thin line between different phases: liftoff/touchdown transient phases ($||$).

$$\begin{bmatrix} r_x & r_y & r_z & \alpha & \beta & \gamma \end{bmatrix}^T = f_b = f_{bodypose}(\mathbf{s}_i, \mathbf{p}_i), \tag{6.1}$$

where $i = 1, 3, 5$ or $i = 2, 4, 6$ denotes left/right tripod, $\mathbf{s}_i$ denotes the sensory measurements available regarding the configuration of the kinematic chain connecting the robot body to the i^{th} toe, and $\mathbf{p}_i$ denotes the vector from COM to hip of i^{th} leg. In the case of RHex with one actuated rotational DOF associated with each compliant leg, $\mathbf{s}_i$ can be denoted as

$$\mathbf{s}_i(\theta_i, \epsilon_{ij}) = \mathcal{N}_{\mathcal{C}_i\mathcal{B}}(\theta_i) \circ \mathcal{M}_{SD\_i}(\epsilon_{ij})$$

as shown in (4.1) where $\mathcal{N}_{\mathcal{C}_i\mathcal{B}}$ denotes the i^{th} leg position from encoder measurement θ_i, and $\mathcal{M}_{SD\_i}$ denotes a memoryless transformation from (data driven phenomenological) models relating leg strain ϵ_{ij} to i^{th} leg configuration detailed in Section 4.1.1.

6.2.2 Linear/Angular Acceleration and Angular Velocity from IMU with 12 DOF Accelerometer Suite and 3 DOF Gyro

Theoretically, linear/angular acceleration and angular velocity can be delivered by the 12 DOF accelerometer suite expressed in a general form:

$$\begin{bmatrix} \ddot{r_x} & \ddot{r_y} & \ddot{r_z} & \ddot{\alpha} & \ddot{\beta} & \ddot{\gamma} & \dot{\alpha} & \dot{\beta} & \dot{\gamma} \end{bmatrix}^T = f_{12Accel}(\mathbf{a}_k),\ _{k=1,2,3,4}. \tag{6.2}$$

However, as detailed in Section 5.3, in practical implementation in RHex, the constrained physical geometry results in a dubious angular velocity measurement:

$$\begin{bmatrix} \dot{\alpha} & \dot{\beta} & \dot{\gamma} \end{bmatrix}^T = f_w(\mathbf{a}_k),\ _{k=1,2,3,4}. \tag{6.3}$$

Consequently, in this investigation we rely upon measurements of angular velocity arising from a MEMS gyro retaining only the acceleration components (expressed in two separate functions) of the accelerometer suite's estimate expressed in general forms:

$$\begin{aligned} \begin{bmatrix} \ddot{r_x} & \ddot{r_y} & \ddot{r_z} \end{bmatrix}^T &= f_a(\mathbf{a}_k),\ _{k=1,2,3,4} \\ \begin{bmatrix} \ddot{\alpha} & \ddot{\beta} & \ddot{\gamma} \end{bmatrix}^T &= f_r(\mathbf{a}_k),\ _{k=1,2,3,4} \\ \begin{bmatrix} \dot{\alpha} & \dot{\beta} & \dot{\gamma} \end{bmatrix}^T &= f_{gyro}. \end{aligned} \tag{6.4}$$

6.3 Fusion Algorithm for Full Body State Estimation

Tradeoffs between the performance (the accuracy of its measurements and its reliability) and cost (actual dollars, required "real estate", and ease of use) of a sensor suite are governed by tightly inter-related issues arising from geometric as well as technological considerations. Once the sensor is chosen, however, the only possibility for improved state estimates depends on the choice of estimation model and algorithm. The design of estimation algorithms for nonlinear dynamical systems has spawned a huge body of literature whose consideration lies well beyond the scope of this dissertation. Hence, we concentrate our efforts on a well understood and highly regarded standard, the Extended Kalman Filter (EKF), and devote the remainder of this chapter to a comparison of estimates arising from different dynamical models that make various use of the available sensor suite.

As discussed in Section 6.1, we adopt a greatly simplified view of hexapod jogging by positing a succession of low dimensional models presumed to capture the essential features of the robot's rigid body dynamics as determined by an idealized periodic sequence of leg contact conditions. We trigger the succession of one model by the next using a "hard switch"—a deterministic predicate over the raw sensory data—and initialize the successor using an exact copy of the predecessor's final state. In Section 6.5, we will initiate a discussion from a more formal point of view and seek to implement theoretically motivated switching procedures based upon a comparison of the multiple models' prediction errors against which the results of this preliminary inquiry may be compared.

We are also interested in assessing the relative value of the two sensing modalities, and will adjust the details of the successive estimation models to accommodate the presence or absence of appropriate subsets of the complete sensor suite. We find it most natural to treat the leg pose sensor system, operative only during intermittent stance phases, as a "drift-corrector" for the IMU sensor that runs continually through aerial as well as ground contact phases. At the same time we are also interested in the effect of the extra angular acceleration input to the traditional IMU system and to the final fused system. We seek to determine whether one of these two subsystems is "better" than the other and whether two operating together in this manner are better than either one alone.

In this section we first briefly review the EKF structure as a means of establishing notational conventions. Models and resulting filters for the rotational degrees of freedom are presented in Section 6.3.2 and those addressing the translational degrees of freedom in Section 6.3.3. Finally, Section 6.3.4 presents our methodology to compute full body state from each of the two independent sensing sources alone.

6.3.1 Notation Associated with the Extended Kalman Filter

Given a discrete time-invariant plant

$$\mathbf{x}_{k+1} = f(\mathbf{x}_k, \mathbf{u}_k, \mathbf{w}_k)$$

with measurement

$$\mathbf{y}_{k+1} = h(\mathbf{x}_k, \mathbf{v}_k)$$

where the process noise $\mathbf{w}_k$ and measurement noise $\mathbf{v}_k$ are white with zero means and covariance defined by $\mathcal{E}[\mathbf{w}_k \mathbf{w}_k^T] = \mathbf{Q}_k$ and $\mathcal{E}[\mathbf{v}_k \mathbf{v}_k^T] = \mathbf{R}_k$, an EKF incorporates two steps: a time update (á priori estimate),

$$\begin{array}{lcl} \mathbf{x}_{k+1}^- & = & f(\mathbf{x}_k^-, \mathbf{u}_k, 0) \\ \mathbf{P}_{k+1}^- & = & \Phi_k \mathbf{P}_k^+ \Phi_k^T + \mathbf{Q}_k \\ \text{with} & & \Phi_k = \frac{\partial f}{\partial x} \mid_{\mathbf{x}_k^+} \\ & & \Gamma_k = \frac{\partial f}{\partial x} \mid_{\mathbf{u}_k} \end{array} \tag{6.5}$$

and a measurement update (posteriori estimate)

$$
\begin{array}{lcl}
\mathbf{K}_{k+1} & = & \mathbf{P}_{k+1}^{-}\mathbf{H}_k^T(\mathbf{H}_k\mathbf{P}_{k+1}^{-}\mathbf{H}_k^T + \mathbf{R}_k)^{-1} \\
\mathbf{x}_{k+1}^{+} & = & \mathbf{x}_{k+1}^{-} + \mathbf{K}_{k+1}(\mathbf{z}_k - \mathbf{H}_k\mathbf{x}_{k+1}^{-}) \\
\mathbf{P}_{k+1}^{+} & = & \mathbf{P}_{k+1}^{-} - \mathbf{K}_{k+1}\mathbf{H}_k\mathbf{P}_{k+1}^{-} \\
\text{with} & & \mathbf{H}_k = \frac{\partial h}{\partial x} \mid_{\mathbf{x}_k^{+}}
\end{array} \tag{6.6}
$$

where $\mathbf{P}_k$ is error covariance matrix, $\mathbf{K}_k$ is the so called Kalman gain, and $\mathbf{z}_k$ is the sensor measurement (partial state directly from sensor shown in Section 6.2). Upon initializing the value of state, $\mathbf{x}_0$, and error covariance matrix, $\mathbf{P}_0$, the (Extended) Kalman Filter continuously delivers the best state "optimal" estimates by consecutively performing these two updates at each time stamp.

The body pose measurement noise covariance arising from the leg pose sensor ($\mathbf{R}_l$), along with the linear/angular acceleration and angular velocity noise covariance arising from the 12 DOF accelerometer suite ($\mathbf{R}_a$, $\mathbf{R}_r$, and $\mathbf{R}_w$) are propagated at nominal points ($\mathbf{s}_0$ and $\mathbf{a}_0$) of raw sensor noise ($\mathbf{R}_{\mathbf{s}_i}$ and $\mathbf{R}_{\mathbf{a}_k}$) from empirical measurement:

$$
\begin{array}{lcll}
\mathbf{R}_l & = & \mathbf{J}_l\mathbf{R}_{\mathbf{s}_i}\mathbf{J}_l^T & \text{with } \mathbf{J}_l = \frac{\partial f_b}{\partial \mathbf{s}_i} \mid_{\mathbf{s}_0} \;\; {\scriptstyle i=1,3,5} \text{ or } {\scriptstyle i=2,4,6} \\
\mathbf{R}_a & = & \mathbf{J}_a\mathbf{R}_{\mathbf{a}_k}\mathbf{J}_a^T & \text{with } \mathbf{J}_a = \frac{\partial f_a}{\partial \mathbf{a}_k} \mid_{\mathbf{a}_0} \;\; {\scriptstyle k=1,2,3,4} \\
\mathbf{R}_r & = & \mathbf{J}_r\mathbf{R}_{\mathbf{a}_k}\mathbf{J}_r^T & \text{with } \mathbf{J}_r = \frac{\partial f_r}{\partial \mathbf{a}_k} \mid_{\mathbf{a}_0} \;\; {\scriptstyle k=1,2,3,4} \\
\mathbf{R}_w & = & \mathbf{J}_w\mathbf{R}_{\mathbf{a}_k}\mathbf{J}_w^T & \text{with } \mathbf{J}_w = \frac{\partial f_w}{\partial \mathbf{a}_k} \mid_{\mathbf{a}_0} \;\; {\scriptstyle k=1,2,3,4} \;.
\end{array}
$$

The noise covariance of angular velocity from gyro ($\mathbf{R}_g$) is directly measured from sensor noise empirically.

6.3.2 Computation of Rotational State

We find it convenient to adopt the quaternion representation of rigid body rotations, $q \in S^3$, (i.e., unit vectors in R^4), in which case velocities are tangent vectors to the sphere, $\omega \in R^3$, yielding the complete rotational state representation as

$$
\mathbf{x}_7 = \begin{bmatrix} q_0 & q_1 & q_2 & q_3 & \omega_x & \omega_y & \omega_z \end{bmatrix}^T. \tag{6.7}
$$

When we introduce angular acceleration inputs from the 12 DOF accelerometer suite to this model, we require an appropriately "inflated" view of state

$$
\mathbf{x}_{10} = \begin{bmatrix} q_0 & q_1 & q_2 & q_3 & \omega_x & \omega_y & \omega_z & \dot{\omega}_x & \dot{\omega}_y & \dot{\omega}_z \end{bmatrix}^T. \tag{6.8}
$$

Following a long tradition in inertial guidance literature [BDW95], for all phases of the recurring gait cycle we adopt a naive constant acceleration model for á priori estimate (6.5), that simply asserts that the position is the integral of velocity which is in turn the integral of acceleration.

Differing sensory feedback structures yield different posteriori estimates. We would like to evaluate the following 3 models with different sensor feedback applied to fusion schemes for three phases of jogging locomotion (tripod stance, transient, and aerial phases):

- **Advanced IMU (AIMU)**

  With both angular velocity/acceleration available, the 10-element state shown in (6.8) for EKF computation is adopted, and the sensor measurements ($\mathbf{z}$) and the measurement matrix ($\mathbf{H}$) change to

$$\begin{aligned} \mathbf{z}_{AIMU} &= \begin{bmatrix} \omega_x & \omega_y & \omega_z & \dot{\omega}_x & \dot{\omega}_y & \dot{\omega}_z \end{bmatrix}^T \\ \mathbf{H}_{TIMU} &= \begin{bmatrix} \mathbf{O}_{6\times 4} & \mathbf{I}_{6\times 6} \end{bmatrix}. \end{aligned} \tag{6.9}$$

- **Fusion of Traditional IMU and Leg Pose Sensor (LPS)**

  The structure of EKF is similar to that of the traditional IMU (use $\mathbf{x}_7$ shown in (6.7)), but with additional body pose feedback:

$$\begin{aligned} \mathbf{z}_{TIMU+LPS} &= \begin{bmatrix} q_0 & q_1 & q_2 & q_3 & \omega_x & \omega_y & \omega_z \end{bmatrix}^T \\ \mathbf{H}_{TIMU+LPS} &= \mathbf{I}_{7\times 7}. \end{aligned} \tag{6.10}$$

  where $\begin{bmatrix} q_0 & q_1 & q_2 & q_3 \end{bmatrix}^T = f_q(\alpha, \beta, \gamma)$ is the quaternion representation of an orientation state obtained from the leg pose sensor (partial output of f_b shown in (6.1)). Note that this mode is available only in the tripod stance phase due to the availability of the body pose sensor.

- **Fusion of Advanced IMU and Leg Pose Sensor**

  The availability of sensor measurements in all 10-element states yields the sensor measurements ($\mathbf{z}$) being equal to the state vector shown in (6.8), which results in the measurement matrix ($\mathbf{H}$) being the identity:

$$\begin{aligned} \mathbf{z}_{AIMU+LPS} &= \mathbf{x}_{10} \\ \mathbf{H}_{AIMU+LPS} &= \mathbf{I}_{10\times 10}. \end{aligned} \tag{6.11}$$

  This mode is also available only in tripod stance phase.

6.3.3 Computation of Translational State

The procedure to apply EKF for fusion on the translational state is similar to it's application to rotational state but with a couple of major differences: First, the translational state in three orthogonal directions can easily be modeled separately and linearly (EKF simplified to KF); second, in contrast to the rotational degrees of freedom, there is no intrinsic sensory measure of translational velocity (measurement is only available in displacement and acceleration); and third, the use of body acceleration data must be mediated by the rotational estimates relative to the inertial frame (depending on orientation state). Due to limited selection of sensor feedback, here we focus on the evaluation of different simple models for á priori estimates.

Since acceleration is the principle measurement in translational state among all three phases instead of (angular) velocity as in rotational state, the state vector for simple 1 DOF models yields

$$\mathbf{x}_3 = \begin{bmatrix} r & \dot{r} & \ddot{r} \end{bmatrix}^T. \tag{6.12}$$

Proceeding with the same naive assumption of constant acceleration, the 1 DOF model associated with this state vector without any external input ($\mathbf{u} = 0$) used in á priori estimate in EKF is

$$\Phi_{acl} = \begin{bmatrix} 1 & \Delta t & \frac{1}{2}\Delta t^2 \\ 0 & 1 & \Delta t \\ 0 & 0 & 1 \end{bmatrix}, \tag{6.13}$$

where Δt is time difference between the current measurement and the previous one. One DOF constant velocity model, another common choice based on naive assumption, without terms associated with acceleration is simply

$$\Phi_{vel} = \begin{bmatrix} 1 & \Delta t & 0 \\ 0 & 1 & 0 \\ 0 & 0 & 0 \end{bmatrix} \tag{6.14}$$

where the acceleration state is kept for usage in sensor feedback and easier model propagation through different phases.

One simple and useful 1 DOF model with physical principles used in aerial phase is the ballistic model, which is a constant velocity model ($\Phi_{bal} = \Phi_{vel}$) without external input ($\mathbf{u} = 0$) in lateral/forward directions and with gravity as external input ($\mathbf{u} = g$, gravity constant) in the vertical direction with input vector as

$$\Gamma_{bal} = \begin{bmatrix} \frac{1}{2}\Delta t^2 & \Delta t & 1 \end{bmatrix}^T \tag{6.15}$$

Unlike the rotational state with three kinds of sensor data for feedback, translational state only has two—with/without leg pose sensor coped with continuous IMU measure:

$$\begin{aligned} \mathbf{H}_{IMU} &= \begin{bmatrix} 0 & 0 & 1 \end{bmatrix} \\ \mathbf{H}_{IMU+LPS} &= \begin{bmatrix} 1 & 0 & 0 \\ 0 & 0 & 1 \end{bmatrix} \end{aligned} \tag{6.16}$$

Another interesting model where the leg pose sensor is available during tripod phase is a constant velocity model ($\Phi_{ext} = \Phi_{vel}$) with IMU data as external inputs ($\Gamma_{ext} = \Gamma_{bal}$), where the feedback vector is simply $\mathbf{H}_{LPS} = \begin{bmatrix} 1 & 0 & 0 \end{bmatrix}$.

6.3.4 Full Body State from Each Sensor Alone

Full body state can be estimated by each sensor alone (body pose sensor or IMU) without combining with other sensors under certain model assumptions. This section illustrates the above methodology to serve as the baseline for performance comparison.

Body State from Leg Pose Sensor

During the tripod stance phase ($\Upsilon_{S(i)}$) shown in Figure 4.2, the leg configuration sensor delivers 6 DOF body pose data with respect to that of the initial touchdown moment ($t_1(i)$), detailed in Section 4.1.1. The pose and velocity state derived by differentiating the pose information at the take-off instant, detected by the same leg configuration sensor, can be further used as the initial condition (I.C.) for the following transient phase, which continuously provides full state based on an assumed constant velocity model (rather than the alternative constant acceleration model due to significant noise effects in differentiation to obtain takeoff acceleration). Similarly, the state at the end of the take-off transient phase passes to the following aerial phase with a physics-based ballistic model, followed by another transient phase again before landing. With this methodology the full 12 DOF state estimates can be provided continuously by the leg pose sensor.

Body State from Traditional IMU

Full body state can be derived from traditional IMU (TIMU) data in various ways: from fundamental double/single integration of raw accelerometer/gyro output, by applying a more standard method EKF described in Section 6.3.1 for further filtering, or through a higher level algorithm by using EKF with multi-model switching (hybrid system) detailed in Section 6.5, or by a purely customized algorithm suitable for specific tasks and applications. In order to keep up with the consistency of our simple-model strategy and establish a standard for baseline comparison, we proceed with the same naive constant acceleration model in the current development. Since only one sensory data is available in each dimension (linear acceleration available for translational state and angular velocity available for rotational state), EKF computation serves only for filtering without fusion.

In the rotational state the 7-element state vector shown in (6.7) is sufficient, where sensor measurement ($\mathbf{z}$) and measurement matrix ($\mathbf{H}$) appear to be

$$\begin{aligned} \mathbf{z}_{TIMU} &= \begin{bmatrix} \omega_x & \omega_y & \omega_z \end{bmatrix}^T \\ \mathbf{H}_{TIMU} &= \begin{bmatrix} \mathbf{O}_{3\times 4} & \mathbf{I}_{3\times 3} \end{bmatrix}. \end{aligned} \quad (6.17)$$

In the translational state the prediction model and measurement vector are used independently in each of 3 dimensions has been shown in (6.13) and (6.16) accordingly.
It has long been remarked in the literature that since its dynamical model is unobservable, the associated Kalman Filter of this "IMU-only" system does not guarantee better performance than direct integration. Of course, the naive assumption of white noise and the likelihood of an inaccurate initial error covariance matrix add to the accumulation of error.

6.4 Performance Evaluation

6.4.1 Experiment Setup

We have evaluated these estimators experimentally on a version of RHex (50 cm x 20 cm x 30 cm) pictured in Figure 2.5, incorporating the required sensors which include: the customized leg pose sensor (delivering full body pose) detailed in Section 4.1.1, a 3 DOF rate gyro (by three 1 DOF MEMS gyro ADXRS300 from Analog Device, delivering angular velocity) and a 12 DOF accelerometer (by eight 2 DOF MEMS accelerometer ADXL210 from Analog Device, delivering linear/angular acceleration). In principle, the advanced IMU can play the role of a complete inertial sensor, delivering three components of body state (linear and angular acceleration as well as angular velocity) without the need for a gyro as long as the "sensor simplex" satisfies the volume property introduced in Section 5.3. While RHex's dimensions permit a sensor arrangement that formally satisfies this requirement, we detail in Section 5.3.2 how the robot's relatively small body constrains the numerical conditioning of the resulting regression problem severely enough to preclude the use of angular velocity estimates so derived. Consequently, we find it essential to use the rate gyro data included in the IMU package.

To assess performance improvements resulting from the fusion of leg pose and IMU data, we have run RHex under the GTMS detailed in Section 4.2, the same system we use to evaluate the body pose estimation by leg configuration sensor detailed in Chapter 4. This yields another set of 12 DOF body state (6 DOF from position measurement and 6 DOF from their derivatives) for comparison. We quantify performance by presenting the standard RMS error given in (4.6) which we redisplay here:

$$f_{RMSE}(\mathbf{d}, \hat{\mathbf{d}}) := \sqrt{(\left|\left|\mathbf{d} - \hat{\mathbf{d}}\right|\right|_2^2 / N)}$$

where $\mathbf{d} = (\mathbf{d}_1, ..., \mathbf{d}_N)$ and $\mathbf{d}_i := (r_x, r_y, r_z, \alpha, \beta, \gamma)_i$ represents the configuration trajectory with length N from the GTMS, while $\hat{\mathbf{d}}$ denotes the corresponding configuration trajectory estimate output from the algorithm.

The common sensor data for all models and associated GTMS output is recorded over the course of 2-meter long experimental runs and then processed offline to assess model performance. RHex's relatively constrained kinematics precludes the exercise of its yaw

Table 6.1: Empirical Phase Relations in RHex Jogging Gait

Phases in one complete stride		
Phases	Average time (ms) mean (std)	Percentage of time (%) mean (std)
Tripod Stance	96.1 (5.9)	44.4 (2.7)
Liftoff Transient	29.0 (4.9)	13.4 (2.3)
Aerial	55.2 (6.6)	25.5 (3.0)
Touchdown Transient	36.0 (5.5)	16.7 (2.6)
Total	216.3 (2.3)	100.0

degree of freedom, barring intentional excitation of slipping motion on particular toes such as would be required for turning. In consequence, because turns are difficult to execute repeatably under the current open loop gait controller, we perform straight-line experimental runs on flat terrain. This simplified evaluation protocol avoids the need for another (complex and necessarily empirical) model that describes turning. Similarly, since we are only concerned with stable gaits in this paper, we analyze data gathered only during steady state conditions following the transient from standstill to exclude irregular model switching sequences and the attendant model errors that would not be captured well within the EKF's Gaussian noise framework. Table 6.1 summarizes RHex's absolute and relative phase timing measured at 1 KHz averaged over 10 experimental runs, providing a feel for how quickly the phases switch and how many data points are available in each phase. Individual leg strain measurements are used to estimate the constituent leg touchdown and liftoff times. The small variation of total time demonstrates the overall reliability of the steady state stride excited by the Buehler clock detailed in Section 6.1, whereas the larger relative variations of each phase suggest the imperfections in the gait stability that result from this feedforward control scheme.

6.4.2 Performance on the Rotational State

Besides the performance of three baseline systems—leg pose sensor only (a), IMU with directly integration only (b), and IMU with EKF (c, $\mathbf{G}_{TIMU} + \mathbf{T}_{TIMU} + \mathbf{A}_{TIMU}$)—we would like to compare three different fusion scenarios where models for the tripod stance phase ($\mathbf{G}$), the transient phase ($\mathbf{T}$), and the aerial phase ($\mathbf{A}$) are selected separately:

- (D), $\mathbf{G}_{AIMU} + \mathbf{T}_{AIMU} + \mathbf{A}_{AIMU}$ — advanced IMU with EKF in all three phases, fusion of angular velocity/acceleration data
- (E), $\mathbf{G}_{TIMU+LPS} + \mathbf{T}_{TIMU} + \mathbf{A}_{TIMU}$ — case (c) plus measurement from leg pose sensor in tripod stance phase, fusion of angular velocity and orientation data

- (F), $\mathbf{G}_{AIMU+LPS} + \mathbf{T}_{AIMU} + \mathbf{A}_{AIMU}$ — case (D) plus measurement from leg pose sensor in tripod stance phase, fusion among angular velocity/acceleration and orientation data

Table 6.2[2] lists the statistical results (mean and standard deviation from 10 experimental runs) of the RMS error between the data from output of the algorithm and that from GTMS for all 6 rotational states, including body orientation in pitch (α), roll (β), yaw (γ), and their derivatives ($\dot{\alpha}$, $\dot{\beta}$, and $\dot{\gamma}$). Our major observations can be summarized as follows:

- Leg pose sensor (a) has good orientation estimation in the tripod stance phase detailed in Section 4.3.4; however, its performance for overall jogging locomotion is poor due to the lack of sensor information in the remaining three phases. This poor performance occurs when the state information is computed from either an incorrect model or a poor estimate of the take off velocity. This can be observed by the good data match to the GTMS between triangles ($\triangleleft\, \triangleright$), denoting the tripod stance phase. In the remaining phases one can observe a bad estimation curve as shown in Figure 6.2.

- The similar performance of the IMU with direct integration (b) and with KF (c) under the same sensor source (angular velocity) validate the claim made in Section 6.3.4.

- With one more sensor (angular acceleration) fedback into EKF helping to "smooth" data, the performance of angular velocity in case (D) is better than that of the original case (c). We do not see much difference in the orientation state between cases (c) and (D), probably due to the fact that the estimation is dominated by the sensor measurement of angular velocity, from the same source.

- With the help from the leg pose sensor in cases (E)(F) during tripod stance phase acting as a "recalibration" mechanism to reset drift in the IMU, the final observable system has much better and bounded estimation in orientation state than the original systems (c)(D). Similarly, we do not see much difference in the velocity state between cases (c) and (E), probably due to the same reason—estimation of the state is dominated by the sensor measurement of angular velocity, from the same source.

- Even though the velocity performance in case (F) is not as promising as in case (D) due to the effect of measurement from leg pose sensor, the ultimate system (F) with sensor feedback in all states delivers the most balanced estimation.

- Despite the algorithm's capability of fusion in the yaw state, RHex's mechanism constraints precludes the yaw motion, causing the implemented leg pose sensor to lack sensitivity in the yaw direction. Therefore, γ and its derivative $\dot{\gamma}$ in cases (E)(F) are

[2] Small letters (a), (b), (c) indicates that each state in this system is provided by model with single sensing source without fusion; on the other hand, capital letters (D), (E), (F) indicates that each state has at least two sensing sources for data fusion.

Table 6.2: RMS Error of Rotational Body State Estimation according to Leg Pose Sensor/IMU alone and Different Fusion Algorithms/Models detailed in Section 6.3.4 and Section 6.3.2

	Model Type	Body State - Angular Velocity			Body State - Orientation		
		$\dot{\alpha}$ (deg/s) mean (std)	$\dot{\beta}$ (deg/s) mean (std)	$\dot{\gamma}$ (deg/s) mean (std)	α (deg) mean (std)	β (deg) mean (std)	γ (deg) mean (std)
a	Leg Pose Sensor	43.41 (6.47)	74.34 (6.35)	N/A N/A	1.65 (0.29)	5.30 (0.58)	N/A N/A
b	IMU (direct integration)	16.17 (4.05)	41.26 (7.73)	9.07 (1.70)	1.40 (0.80)	2.31 (0.73)	1.17 (0.59)
c	IMU (with EKF)	16.21 (4.06)	41.24 (7.75)	9.07 (1.66)	1.42 (0.79)	2.38 (0.79)	1.09 (0.56)
D	$\mathbf{G}_{AIMU} + \mathbf{T}_{AIMU} + \mathbf{A}_{AIMU}$	14.65 (3.88)	34.19 (7.22)	8.43 (1.53)	1.47 (0.82)	2.32 (0.73)	1.19 (0.60)
E	$\mathbf{G}_{TIMU+LPS} + \mathbf{T}_{TIMU} + \mathbf{A}_{TIMU}$	16.52 (4.40)	41.24 (7.78)	9.07 (1.66)	0.96 (0.21)	1.71 (0.49)	1.09 (0.56)
F	$\mathbf{G}_{AIMU+LPS} + \mathbf{T}_{AIMU} + \mathbf{A}_{AIMU}$	15.32 (3.84)	37.07 (7.52)	8.43 (1.53)	0.96 (0.20)	1.75 (0.48)	1.19 (0.60)

directly obtained from IMU measurements, as in cases (c)(D), without fusion with leg pose sensor.

- Figure 6.2 also shows the typical situation of the IMU only system—inconsistent drifting in the orientation state in each experimental run due to blind integration[3], which can also be checked by larger standard deviation in cases (c)(D) than in cases (E)(F) with support of the leg pose sensor.

6.4.3 Performance on the Translational State

As can be seen gyro acts as the major sensing source for the rotational state, which directly yields the deployment of constant velocity model in á priori estimates (like cases (c)(D) in Section 6.4.2). Similarly, accelerometer acts as the dominant player in the translational measurement, leading us to adopt a constant acceleration model in á priori estimates in (6.5). At the same time, the ballistic model widely used in free drop motion (aerial phase) implies that the "constant velocity model" (no external force) may also be a good candi-

[3]In this experiment set, pitch and yaw has obvious drift but roll seems to track well.

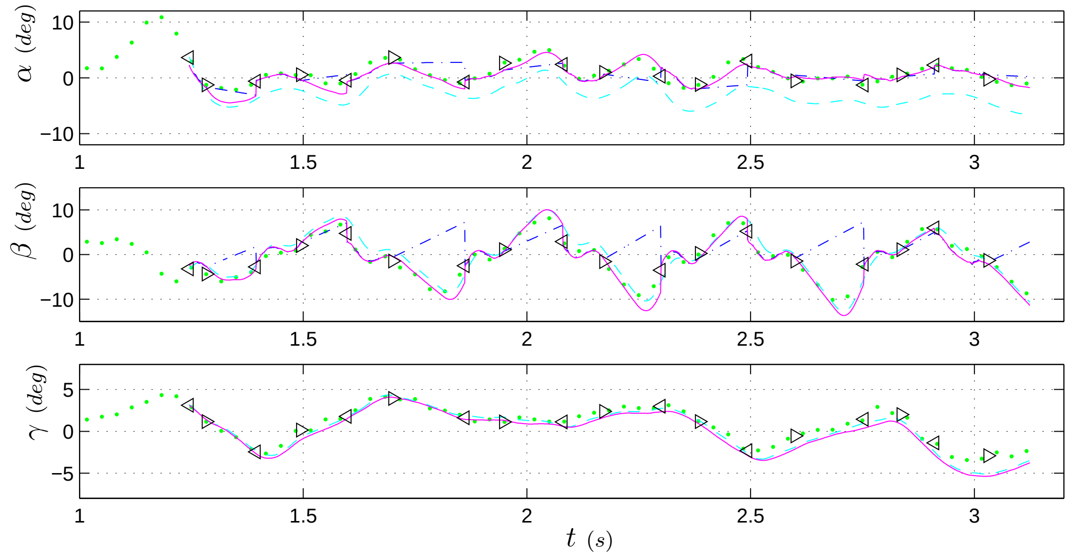

Figure 6.2: Body orientation (pitch (α), roll (β), and yaw (γ)) measured by GTMS (dotted line), leg pose sensor (a, dashdot line), fusion algorithm (D, dashed line, advanced IMU with EKF, $\mathbf{G}_{AIMU} + \mathbf{T}_{AIMU} + \mathbf{A}_{AIMU}$), and fusion algorithm (F, solid line, advanced IMU with EKF with leg pose sensor feedback during tripod stance phase, $\mathbf{G}_{AIMU+LPS} + \mathbf{T}_{AIMU} + \mathbf{A}_{AIMU}$) according to Table 6.2. The plot of (b)(c) and (E) are omitted since their performance in orientation are similar to (D) and (F) accordingly. RHex's mechanism constraints precluding yaw motion yields no yaw reading in the leg pose sensor (dashdot line), so the state of yaw from fusion algorithm (E)(F) are directly adopted from (c)(D) accordingly (magenta linea are the same as dashed line). The interval between triangles (◁ ▷) denotes the tripod stance phase determined by leg pose sensor.

date to estimate COM locomotion. Thus, we would like to evaluate both models in all three phases—tripod stance, aerial, and transient—where the constant velocity model in vertical direction during aerial phase will import gravity externally to simulate ballistic motion. In addition, constant velocity model during tripod stance phase will cope with IMU measurement externally ($\mathbf{u}$) (hereafter referred as the IMU integration model, meaning the external forces can be roughly captured by the IMU) with only the leg pose sensor as the feedback measurement ($\mathbf{z}_{LPS}$). Therefore, in addition to the performance of the three baseline cases, there exists eight different scenarios generated by the combination of two different models in each of three different phases ($2^3 = 8$)—constant acceleration model ($\mathbf{G}_{IMU+LPS}$) with both sensors for feedback measurement (using $\mathbf{H}_{IMU+LPS}$ shown in (6.16)) and IMU integration model ($\mathbf{G}_{ext}$) with leg pose sensor as feedback ($\mathbf{H}_{LPS}$) in tripod stance phase, constant acceleration model ($\mathbf{A}_{acl}$) and ballistic model ($\mathbf{A}_{bal}$) both with IMU as feedback ($\mathbf{H}_{IMU}$) in aerial phase, and constant acceleration and velocity models ($\mathbf{T}_{acl}/\mathbf{T}_{vel}$) both with IMU as feedback ($\mathbf{H}_{IMU}$) in transient phase. In the following discussion, these 8 fusion methods with different models are numbered from (D) to (K) as the reference index according to the list in Table 6.3. Unlike the rotational state with at least two sensor measurements in all phases for data fusion, the translational state processes data fusion only in the tripod stance phase while the remaining phases are estimated by one sensor data (accelerometer) smoothed by the KF.

Figure 6.3 plots COM displacement from some output of algorithm and GTMS (green dot) and the result of various estimation algorithms presented here for a typical experiment. Table 6.3 lists the statistical results (mean and standard deviation from 10 experimental runs) of RMS error between data from output of the various algorithms and that from GTMS for all 6 DOF translational body states, including COM displacement in lateral (r_x), fore/aft (r_y), vertical (r_z) directions, and their derivatives ($\dot{r_x}$, $\dot{r_y}$, and $\dot{r_z}$). Our major observations can be summarized as follows:

- Figure 6.3 shows that the resultant state computation from the leg pose sensor (blue dash-dot line) is accurate in displacement but relatively poor in velocity derived from a noisy derivative process from displacement and orientation data. In contrast, the IMU (cyan dash line) performs oppositely—good in velocity[4] (especially in r_x), but very poor in displacement derived from a noisy double integration process possibly with accumulated error. Dramatically different characteristics between these two sensors serves as the fundamental motivation for fusing sensor data for better state estimation. Table 6.3 also demonstrates the better performance of the leg pose sensor in the displacement state. Although the IMU provides accurate tracking of the velocity state as seen in Figure 6.3, small tracking errors seem are exasperated by the integration over time, resulting in worse RMS error as shown in table. Never-the-less, this still suggests that proper "recalibration" of the IMU data can reset the drift resulting in better velocity estimation.

- It is understandable that the Kalman Filter does not guarantee better performance in every aspect since it "blends" the performance of the prediction model with that of the true measurement correction based on unrealistic assumptions of white noises and hard-to-judge model covariance as well as it needs time to go through transient till stabilization. It is even more of a challenge to use EKF for locomotion that requires hybrid models performing in sequence with fast switching. In this case the performance is determined by many factors—not only by the standard concerns about selections of models, types of measurement feedback, and assumptions of KF detailed in Section 6.3.1, but also by the time required to pass transient stage, as well as by the flow of state and model covariance passing through different phases. Nevertheless, the Kalman Filter still perform robustly and is able to deliver better estimates for most

[4]Velocity can be identified by slope or high frequency components in the plot of displacement or orientation v.s. time.

Table 6.3: RMS Error of Translational Body State Estimation according to Leg Pose Sensor/IMU alone and Different Fusion Algorithms/Models detailed in Section 6.3.4 and Section 6.3.3

	Model Type	Body State - COM Velocity					
		COM Velocity			COM displacement		
		$\dot{r_x}$ (cm/s) mean (std)	$\dot{r_y}$ (cm/s) mean (std)	$\dot{r_z}$ (cm/s) mean (std)	r_x (cm) mean (std)	r_y (cm) mean (std)	r_z (cm) mean (std)
a	Leg Pose Sensor	21.84 (1.75)	17.39 (4.30)	14.88 (1.63)	4.16 (3.52)	5.42 (3.36)	0.82 (0.14)
b	IMU (direct integration)	30.72 (19.44)	20.29 (15.64)	10.30 (3.23)	22.33 (14.26)	16.10 (14.39)	5.00 (3.95)
c	IMU (with KF)	32.29 (21.10)	20.46 (15.32)	10.60 (3.30)	23.60 (14.80)	16.14 (14.18)	5.25 (4.00)
D	$\mathbf{G}_{IMU+LPS} + \mathbf{T}_{acl} + \mathbf{A}_{acl}$	10.48 (3.74)	7.41 (2.41)	9.83 (3.23)	4.74 (3.17)	5.85 (3.74)	1.10 (0.41)
E	$\mathbf{G}_{IMU+LPS} + \mathbf{T}_{acl} + \mathbf{A}_{bal}$	9.60 (2.65)	7.36 (2.63)	9.80 (3.25)	6.32 (3.07)	5.26 (3.78)	1.35 (0.54)
F	$\mathbf{G}_{IMU+LPS} + \mathbf{T}_{vel} + \mathbf{A}_{acl}$	17.83 (8.75)	8.30 (2.19)	15.72 (3.12)	7.15 (8.01)	5.82 (3.40)	3.07 (0.84)
G	$\mathbf{G}_{IMU+LPS} + \mathbf{T}_{vel} + \mathbf{A}_{bal}$	15.53 (8.16)	7.54 (1.88)	20.03 (3.37)	7.44 (7.61)	5.07 (3.44)	4.77 (1.06)
H	$\mathbf{G}_{ext} + \mathbf{T}_{acl} + \mathbf{A}_{acl}$	29.30 (4.38)	14.32 (2.68)	20.85 (2.96)	4.36 (2.97)	5.29 (3.30)	1.79 (0.18)
I	$\mathbf{G}_{ext} + \mathbf{T}_{acl} + \mathbf{A}_{bal}$	29.17 (4.32)	14.12 (2.60)	19.79 (2.94)	4.47 (3.03)	5.29 (3.31)	1.72 (0.16)
J	$\mathbf{G}_{ext} + \mathbf{T}_{vel} + \mathbf{A}_{acl}$	27.20 (3.97)	14.18 (2.62)	15.83 (2.60)	3.95 (2.27)	5.32 (3.31)	1.38 (0.14)
K	$\mathbf{G}_{ext} + \mathbf{T}_{vel} + \mathbf{A}_{bal}$	27.07 (3.91)	14.00 (2.52)	15.03 (2.53)	4.06 (2.33)	5.33 (3.31)	1.32 (0.13)

states as shown in Table 6.3 and Figure 6.3. One way to solve this problem is to use Interacting Multiple Model (IMM) technology, to be introduced in Section 6.5, which computes multimodels simultaneously and mixes models' outputs based on a weight determined by error covariance. While this solves the problem of discontinuity, some downside arises—first, when empirical operation the robot performs "hard" (quick) switching between different modes, the algorithm yields a longer "transient" time since the mode change is determined by the the slow and smooth change of the value of error covariance; second, the computational power required to compute all models in all situations becomes a real problem if the "model bank" is large unless there is a second algorithm to determine the on/off of models. Results of fusion algorithm from cases (D) to (K), cases (D) and (E) show the best performance and also strong reveal the merit of sensor fusion.

- Better performance is obtained in case (D) (magenta solid line shown in Figure 6.3) by adopting a constant acceleration model with IMU feedback in all three phases consistently, and with extra leg pose sensor feedback in tripod stance phase as "recalibration." This reveals the importance of the flow of the state and covariance matrix. The EKF continuously delivers estimates based on all previous weighted measures. Therefore, in the hybrid system when we change model or feedback structure by a "hard switch" from the previous one to the current one we will introduce discontinuity between states since the new estimates will suffer sudden changes of structure and the EKF needs to go through a transient phase until the filter converges. In this case, two important issues arise: first, the transient time to stabilize the estimation process in new model needs to be short enough so the estimates can begin to deliver accurate state predictions for some period of time in this "mode" (or "phase" in our terminology) before the robot switches to the next mode; second, changing feedback measurements will significantly change the structure of the EKF, resulting in longer transient times. Thus, choosing a good model in a specific phase which is not consistent with the remaining models may not result in better overall performance since better estimates delivered in the shorter stable period are deteriorated by bad estimates delivered in the longer transient time. Thus, putting efforts on choosing a better model suitable for a specified mode/phase may not be an obvious better decision.

- Similar performance between constant acceleration model in case (D) and ballistic model in case (E) in aerial phase (also (F) to (G), (H) to (I), and (J) to (K)) is expectable since the measurement of acceleration should show "ballistic flight" in the aerial phase if the sensor works correctly. This comparison can also be used to check quality of sensor and conditions of installation and calibration.

- Using the IMU as external input in cases (H)(I)(J)(K) turns out to be a bad choice due to following reasons: First, bad velocity estimation confirms that the mechanism of the KF weights more and more on the measurement feedback (i.e. the leg pose sensor) with time propagation, resulting in the decreasing contribution from the IMU. Second, the different characteristics in the models causes huge discontinuities of state estimates during model switch, resulting in a longer transient time to stabilize. One of the outputs in this group (case (I)) plotted in Figure 6.3 (black dot line) reveals

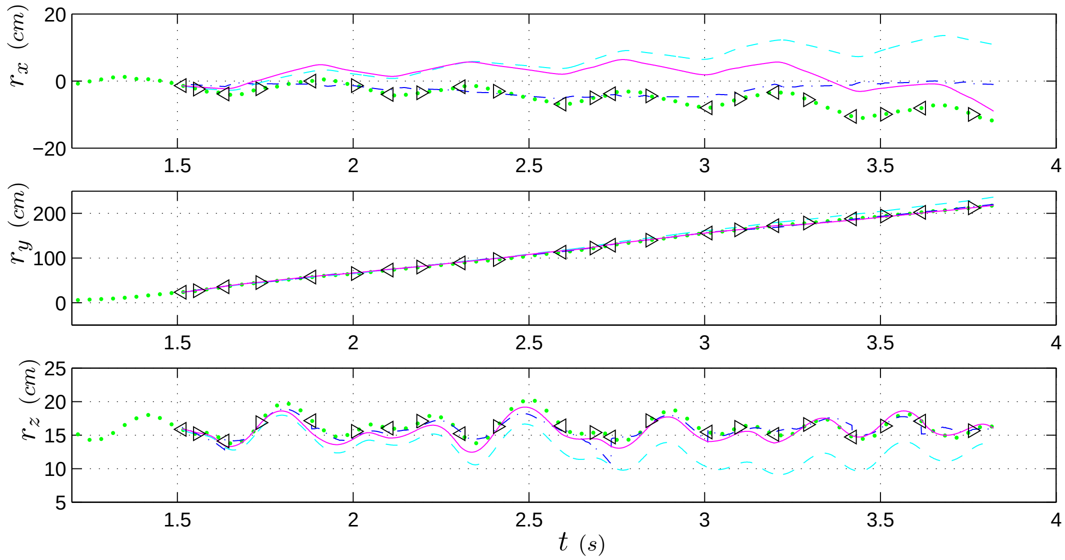

Figure 6.3: Translational COM displacement (lateral (r_x), fore/aft (r_y), and vertical (r_z)) measured by GTMS (dotted line), leg pose sensor (a, dashdot line), IMU with KF (c, dashed line), and fusion algorithm (D, solid line, $\mathbf{G}_{IMU+LPS} + \mathbf{T}_{acl} + \mathbf{A}_{acl}$). Plot of IMU directly integration (b), fusion algorithm (E), and fusion algorithm (H) are omitted due to their similar performance to (c), (D), and (I) accordingly. Plot showing the difference due to model change in the transient phase ((F)(G) to (D)(E), (J)(K) to (H)(I)) are also omitted to reduce the complexity of the figure. The interval between triangles ($\triangleleft$ $\triangleright$) denotes the tripod stance phase determined by leg pose sensor.

this phenomenon clearly.

- Better performance in cases (D)(E) than in cases (F)(G) indicates the existence of force interaction to the ground during the transient phase, since the constant velocity model which impedes the flow of the acceleration state in á priori estimate causes longer transient time.

Generally speaking, the system with constant acceleration models in all four phases and with all available sensors for feedback has the best and most balanced performance.

6.5 Context-based State Estimation

From the beginning of this chapter until the previous section we explain how to develop a body state estimator on a hexapod robot within dynamical gaits (i.e. jogging locomotion) by fusing the data from the leg pose sensor and the IMU. The algorithm itself is quite generic, suitable for a wide range of locomotion with periodic modes (ground, transient, aerial, transient, ground...), jogging, or running fast, and jogging or running with or without turning simultaneously. However, as we mentioned before, using the leg sensor to make the system stable (observable) requires time and effort to develop the leg sensory system. For a robot like RHex it is a difficult task since we need to get leg configuration from continuous-compliant members as well as to transfer sensory data back to the robot body by wireless communication. This task may become easier in the future robots with high DOF rigid legs can inject enough energy into the legs to use them as springs. Limited power density in motors, however, remains a difficult problem to solve. Thus, the alternative approach is to deal with the model and algorithm selections—focusing on software instead of hardware. This may be a low-cost solution if considering implementation in large volumes.

The standard technology to use single (minimum) sensor to estimate the locomotion with different modes is interacting multiple models (IMM) [May79, CA78]. It runs all the possible models simultaneously and judges the accuracy of models by an error covariance matrix between sensor measures and estimated state by models based on the fact that the correct model should provide better estimates. In our case for state estimation with multimodes, the typical choice of sensor is the IMU due to its suitability and accessability. IMM is simple and effective; however, it also comes with a couple of drawbacks. First, it requires powerful computation ability, especially the bank of modes is large. Second, model accuracy is very important since it not only determines the state but also uses its error covariance to judge its effectiveness, especially for the unobservable systems in our case. The selection of model for each mode is strongly dependent on the robot locomotion which is difficult to justify, so our work is focused on how to switch the modes more accurately.

We introduce the "context-based" body state estimation[5] for a hexapod robot executing the same jogging gait in steady state on level terrain. The approach consists of identifying the robot's mode of operation (hybrid system) by classifying the output of onboard sensors into mode-specific contexts. For example, consider the estimation for the vertical state, the acceleration during ground phase (like a SLIP system) and aerial phase (free drop) has significantly different ranges; thus, we can set the threshold on the vertical acceleration to help determine the correct modes and switch the models accordingly. The other context we have tried is leg touchdown information, actually providing correct timing to switch modes. The "context" provides better timing for switching, and it is also utilized to switch on/off the modes in order to save computation power.

This algorithm is still under development by our colleagues at CMU, but the initial results can be summarized as follows. Six-dimensional state are currently modeled separately with 1 DOF simple data driven models, where the parameters are fit particularly to the specific motion. The states in the vertical direction is modeled as SLIP and ballistic models (similar to the motion of pogostick). The performance of estimation by using the leg touchdown sensor as a context is better than that using the accelerometer [SRCL05], but the result is still 50% worse than that utilizing sensor fusion technology, as shown in

[5]In collaboration with Sarjoun Skaff and Alfred Rizzi at Carnegie Mellon University (CMU).

Section 6.4. Two major reasons for this are: first, the system is unobservable which implies the data drifting problem. Second, by using only two modes (ground and aerial), ignores the transient modes which consume around 30% of time in each cycle. Furthermore, it underuses the available information of individual leg touchdown. Pitch, roll, yaw, and COM lateral state are all modeled by simple spring mass systems with periods equivalent to the oscillation of locomotion. Fore/aft state is modeled as a 1st order system since the velocity is nearly constant.

The performance of state estimation is strongly coupled to a specific motion since the parameters of models are empirically tuned. For example, jogging locomotion with different periods should be modeled as different SLIPs with different parameters. Thus, it may be necessary to build a large "model bank" in order to cover a wide range of locomotion. From this point of view, using sensor fusion to make a system observable is a more general approach for this type of state estimation.

CHAPTER 7

Conclusion and Future Work

7.1 Conclusion

This thesis tackles the open problem of building a sensory system for a legged robot with a wide range of motion and various behaviors. The work in this thesis is unique in that it is the first known time this data has been generated for a legged robotic system. The work in this thesis details the development process of the sensory system, complete from the high level conceptual architecture to the low level engineering implementation. This framework concludes that the desired sensing information in a hexapod robot, to be utilized in a feedback controller toward the development of dynamic behaviors, should include full body states on center of mass (COM), foot touchdown information, leg configuration, ground reaction force, and body inertia forces and torques. In this work, we have implemented three different kinds of sensors, including eight 2-axis MEMS accelerometers, three 1-axis MEMS gyroscopes, and six or twelve strain gauges, depending on the use of 4-bar or half-circle legs, on the experimental platform, hexapod RHex [BSK02], and have evaluated the performance of the algorithms on real robot systems.

We introduce a novel approach to implement strain gauges together with simple data driven phenomenological polynomial models to simultaneously deliver information of leg touchdown, leg configuration, and ground reaction force suitable for legged robots with compliant legs. Leg configuration of the 1 degree of freedom (DOF) 4-bar leg [Moo01] on RHex [SBK01] is successfully estimated by one strain gauge, through linear mapping both on the benchtop experimental apparatus and real robot operation, where the foot touchdown information is also successfully delivered by an empirically set threshold on the leg configuration. Using a high speed visual ground truth measurement system (GTMS), we have shown that the leg configuration model used to interpret the strain data achieves very high accuracy in realistic operating conditions [LKK05a,LKK03]—e.g., effective length errors of less than 2%. Leg configuration and ground reaction force of the 2-DOF half-circle leg is also successfully obtained by two strain gauges through linear-quadratic mapping on the benchtop experimental table. The model evaluation on the operating robot is beyond the scope of this thesis due to the limited bandwidth of wireless communication, LegNet [Kom05], between legs and the robot body.

We develop a full body pose estimator for a walking hexapod robot based on the kinematic configuration of its legs structured in a two layer hierarchy. The lower layer relates leg configuration to body pose within a single stance while the higher layer recursively composes consecutive single stance measurements to achieve complete legged odometry—continuous pose computation across multiple steps [LKK05a, LKK04]. We have implemented this algorithm on the robot RHex utilizing strain measurements of its 4-bar legs communicated over a wireless communications network described above[1]. Using a separate conventional frame rate visual GTMS we have evaluated the performance of the resulting low level single stance pose estimator and the high level legged odometry system at various speeds and conditions of surface friction. The body pose estimator is shown to perform well at all speeds over normal ground conditions—achieving, for example, five times more accurate legged odometry than computed from averaged open loop distance-per-stride estimates. The estimator continues to function well over a variety of ground conditions, with the onset of significant performance degradation on the most slippery surfaces, like soaped plastic, whose coefficient of friction is less than a third that of normal linoleum. This pose computation algorithm cannot function if the operating regime includes an aerial phase as is typical of RHex's most useful dynamical gaits [Sar02]. To remedy this shortcoming, this thesis has introduced another sensor suite—the inertial measurement unit (IMU), including linear accelerometers and rotational rate gyroscopes, to complement the leg kinematic configuration sensor introduced here. This multiple array of sensor modalities not only allows us to perform pose estimation during aerial phases but also to generalize the estimation to full 12-DOF state in a wider range of locomotion.

We then introduce a novel 12-axis accelerometer suite theoretically capable of delivering linear/angular acceleration and angular velocity, fulfilling the idea of "advanced IMU", by using the kinematic relationships of rigid body motion without integration or differentiation. This suite provides additional angular acceleration measurement compared to the traditional IMU, avoiding the need for gyroscopes and for localization of the accelerometer at the COM on the robot's body, and simplifies installation and calibration. The partial state provided by the advanced IMU not only yields body inertia force and torque information but also delivers essential sensory feedback for body state estimation. We have implemented this sensory suite on RHex, and have successfully obtained linear and angular acceleration but not angular velocity due to its impracticality in the present setting as a result of numerical ill-conditioning consequent upon the small baseline RHex's body affords. Therefore, along with the traditional 3-axis rate gyroscope this 12-axis accelerometer comprises the advanced IMU that we join in this thesis to our previous leg pose sensor.

We also develop a hybrid full 12-DOF body state estimator for a hexapod robot execut-

[1]Note, in consequence of RHex's constrained kinematics, as explained in Section 4.3, we have not exercised its yaw degree of freedom in this study.

ing a steady jogging gait on level terrain with a significant aerial phase [LKK05c,LKK05b]. We use a repeating sequence of continuous time dynamical models—three distinct models in four successively repeating phases: tripod stance phase, liftoff transient phase, aerial phase, and touchdown transient phase—that are switched in and out of an Extended Kalman Filter to fuse measurements from a low-cost MEMS-based advanced IMU and a novel leg-strain-based body pose estimator installed on a copy of the robot RHex. The estimator is presently implemented offline on data collected by the above sensors in order to compare the performance of different models in the filter. The proper fusion of the data yields state estimates that agree with measurements taken by an offboard GTMS, whereas, in contrast, neither sensing modality yields comparable accuracy when used in isolation. The associated computational costs are not excessive and the algorithm is now ready for online implementation on RHex in conjunction with more aggressive state based feedback controllers [Sar02,SK03]. The sensor suite is quite generic, and we are proceeding with an implementation of this algorithm upon other legged running machines as well. Our results corroborate the notion that two distinct sensory modalities with complementary strengths and weaknesses should yield better state estimates in combination than either can deliver alone. The leg pose sensor cannot function in flight but delivers reliable position information during stance—when the legs do not slip. However velocity data can only be derived from numerical differentiation which is bound to inject noise. In contrast, the IMU operates continually through flight and stance, and offers reliable velocity information—so long as the gyroscopes do not saturate. Nevertheless, position data can only be derived from numerical integration and an increasing drift arising from integration error is likely. For both translational and rotational states, performance is significantly increased when both sensor modalities are fused appropriately. Using the "grounded" leg pose sensor to complement drifting IMU based estimates of pitch and roll, and to correct COM vertical displacement estimates provides a "recalibration" in stance that insures bounded estimation errors in the final outputs. IMU integration drift in the remaining state components can also be mitigated over short distances by this leg-based "recalibration" but slipping toes will eventually degrade absolute horizontal displacement estimates in analogy to the well known problems of odometry in wheeled vehicles [LKK03]. To eliminate the drift over longer ranges, we would require such modalities as a global positioning system (GPS), for COM lateral and fore/aft motion, with a magnetometer, for yaw motion, or a vision system for absolute localization. In spite of that, these systems that provides absolute positioning have less impact relating to the robot's dynamical behavior and stability.

7.2 Future Work

Equipped with the fusion algorithm we have described, we believe that the combined leg pose sensor and advanced IMU provide a ready platform for "slow", i.e. stride-to-stride level, real time feedback control of steady state gait parameters. Our near term plans are to begin experimental work of this kind. Before these sensors can provide state estimates suitable for “fast”, within-stride, control of badly perturbed transient body states, there are two additional improvements that are needed.

First, we will need to develop more physically realistic dynamical models of the transient states, a simple example being the spring loaded inverted pendulum (SLIP) model for the tripod stance phase [AKH04]. The fundamental questions remains—can we find a suitable SLIP model to deliver better state estimation which we will use as sensory feedback for the controller? Or do we need to develop the feedback controller first to “anchor” the robot behavior to the SLIP template? Our initial experience of fitting the robot’s current jogging behavior to the SLIP reveals the following clues regarding how close the current behavior is to the SLIP model and how we might get closer. First, the robot operates in full 6-dimensional space involving ± 10 deg pitch and ± 5 roll motion due to unbalanced and unsynchronized spring compression among three touchdown legs. These effects, however, are ignored by the 3-dimensional SLIP in sagittal plane [AKH04] or the 3-space SLIP with point mass. Thus, how to “project” the 6-dimensional motion into 3-dimensional SLIP motion is a noneligible issue. Second, the question lies on “how to inject energy into this lossy system correctly so that it will behave as an energy-conservative system like SLIP.” In RHex’s case, the direction where energy is injected, the motor power, is not the direction where energy is lost, the leg damping, but at least one can use energy injection in as a way to help recover energy loss. For example, the forward speed of SLIP is entirely determined by dynamics but in RHex it is determined by the constant-speed leg swing motion according to the Buehler Clock. Thus, we are likely able to adjust the leg swing pattern to match the SLIP motion. Furthermore, SLIP provides a good template for the robot to start with due to its simplicity and physical-based property. In addition to models in tripod stance phase, we are convinced that there is a need for more complex combinations of physically motivated ground contact models during the touchdown and liftoff transient phases to improve state estimation and reduce transient in each phase.

Second improvement requires additional algorithmic means of triggering the hybrid dynamics switching protocols that were effected in this thesis only by reference to the leg pose sensor’s cues. We believe that the interacting multiple model (IMM) approach [SRCL05] holds significant promise in this context.

APPENDICES

APPENDIX A

Experimental Data Plots

This appendix provides sensory data plots from four typical experimental runs of RHex within four different gaits (one for each), including jogging, slow walking, medium walking, and fast walking gaits.

The body state estimator for a robot within a jogging gait developed in Chapter 6 utilizes all of the available sensory data on RHex, which includes the strain-based leg configuration sensor shown in Figure A.1, the motor shaft orientation sensor (encoder) shown in Figure A.2, COM acceleration shown in Figure A.4, body angular acceleration shown in Figure A.5, and body angular velocity shown in Figure A.6. COM linear acceleration and body angular acceleration are derived from 12 raw linear accelerations as shown in Figure A.3 measured from the 12-axis accelerometer suite, while angular velocity is delivered by the MEMS gyroscope sensor. Three dimensional coordinates of three markers detected by the ground truth measurement system (GTMS) for performance comparison are shown in Figure A.7.

The body pose estimator for a robot within walking gaits, developed in Chapter 4, only requires the information of toe coordinates with respect to the COM. In RHex's case this can be achieved by utilizing a strain-based leg configuration sensor and motor shaft orientation sensor (encoder). Thus, two sensory data sources together with data from the GTMS are also provided in this appendix. These nine plots from three data multipled by three different walking speeds are shown from Figure A.8 to Figure A.16.

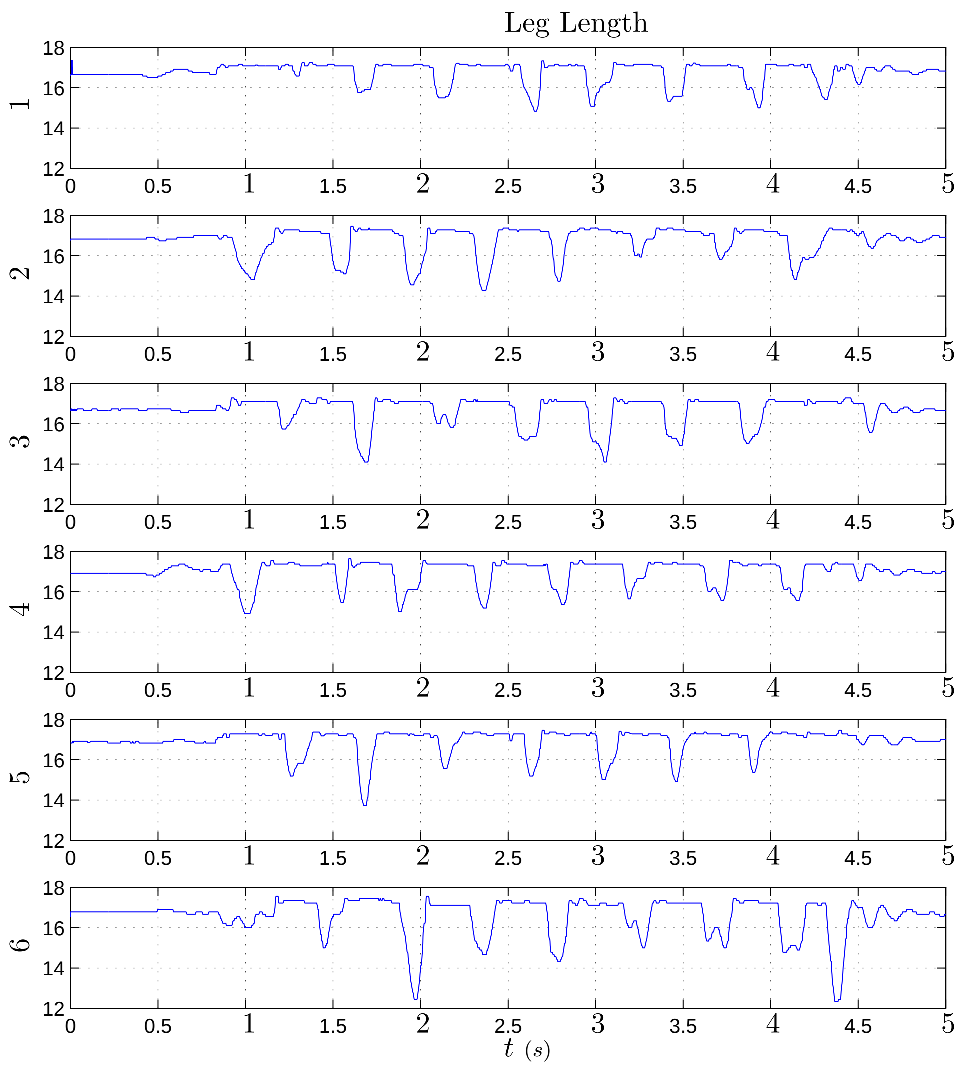

Figure A.1: Experimental data: leg length (jogging gait); 1: left front leg, 2: left middle leg; 3: left hind leg; 4: right front leg; 5: right middle leg; 6: right hind leg

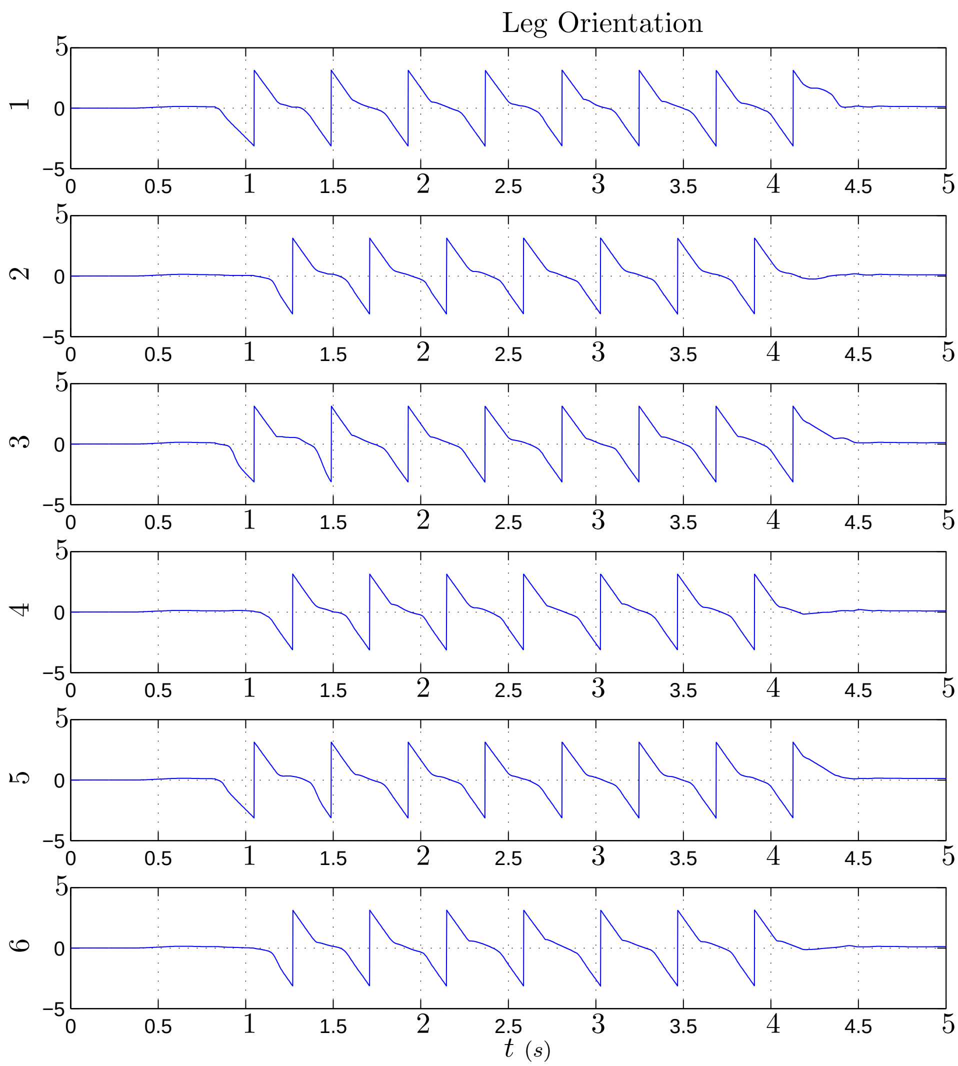

Figure A.2: Experimental data: leg orientation (jogging gait); 1: left front leg, 2: left middle leg; 3: left hind leg; 4: right front leg; 5: right middle leg; 6: right hind leg

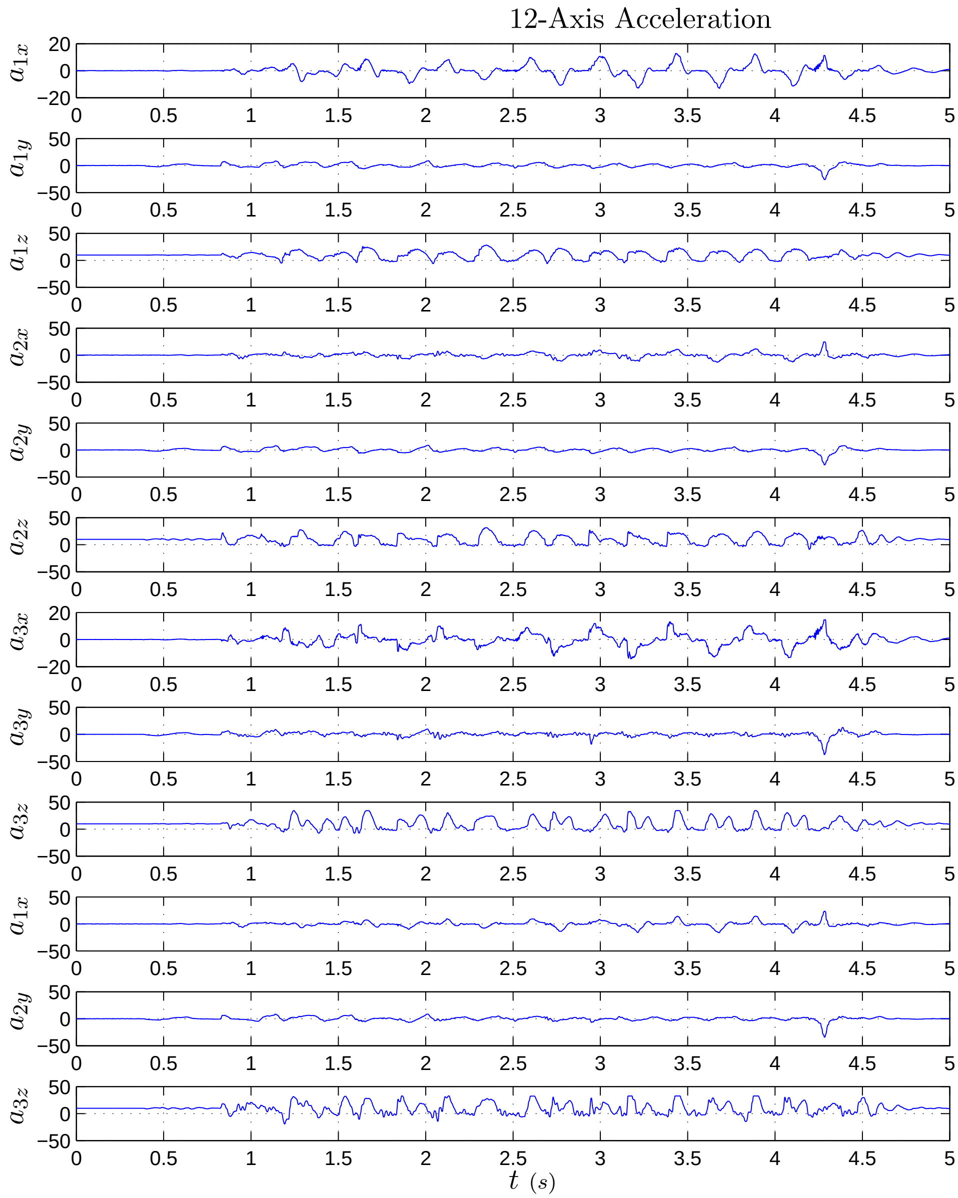

Figure A.3: Experimental data: acceleration from the 12-axis accelerometer suite (in body frame, jogging gait); the locations of these four 3-axis accelerometer suites ($a_{ij}, i = 1, 2, 3, 4, j = x, y, z$) installed on RHex can be found in Figure 5.5; x: lateral direction; y: fore/aft direction; z: vertical direction; label is consistent with (5.9) in Chapter 5

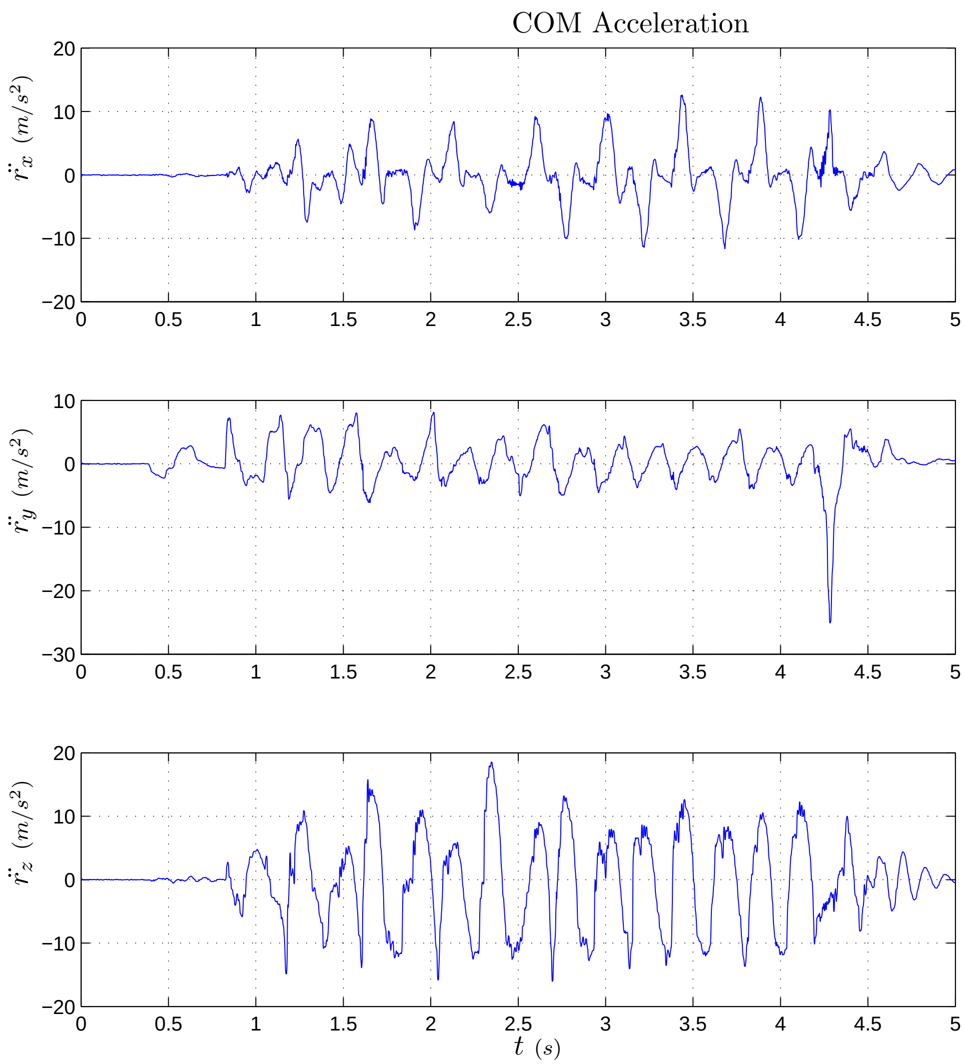

Figure A.4: Experimental data: COM acceleration from 12-axis accelerometer suite (in body frame, jogging gait); $\ddot{r_x}$: lateral direction; $\ddot{r_y}$: fore/aft direction; $\ddot{r_z}$: vertical direction

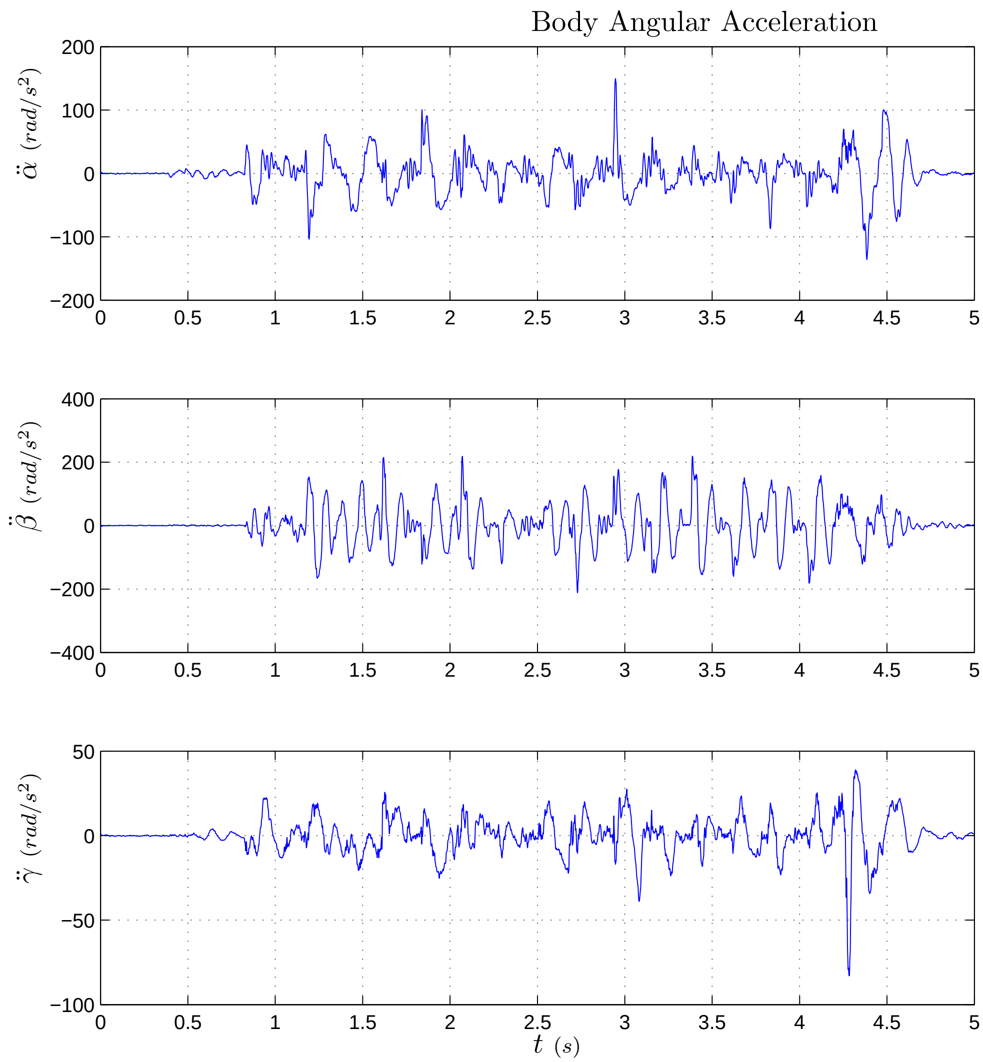

Figure A.5: Experimental data: body angular acceleration 12-axis accelerometer suite (in body frame, jogging gait); $\ddot{\alpha}$: pitch; $\ddot{\beta}$: roll; $\ddot{\gamma}$: yaw

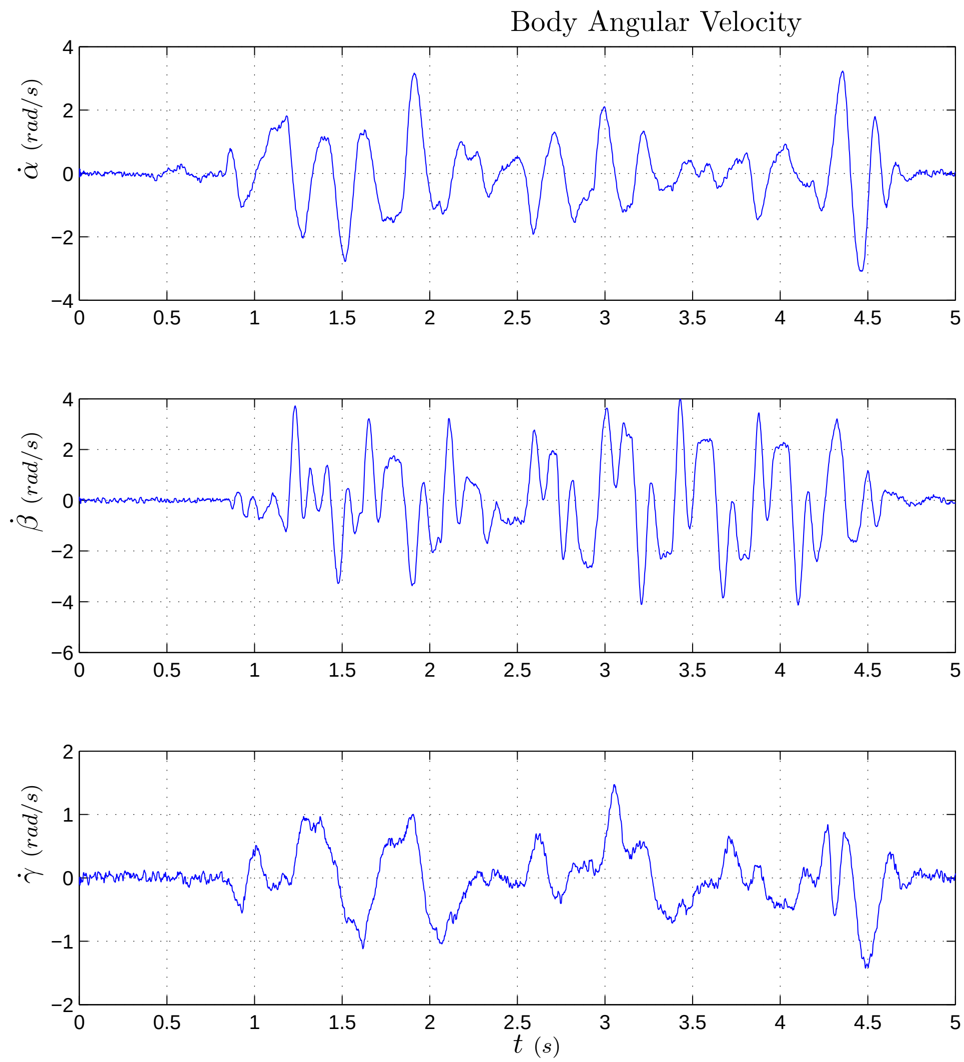

Figure A.6: Experimental data: body angular velocity from MEMS gyroscope (in body frame, jogging gait); $\ddot{\alpha}$: pitch; $\ddot{\beta}$: roll; $\ddot{\gamma}$: yaw

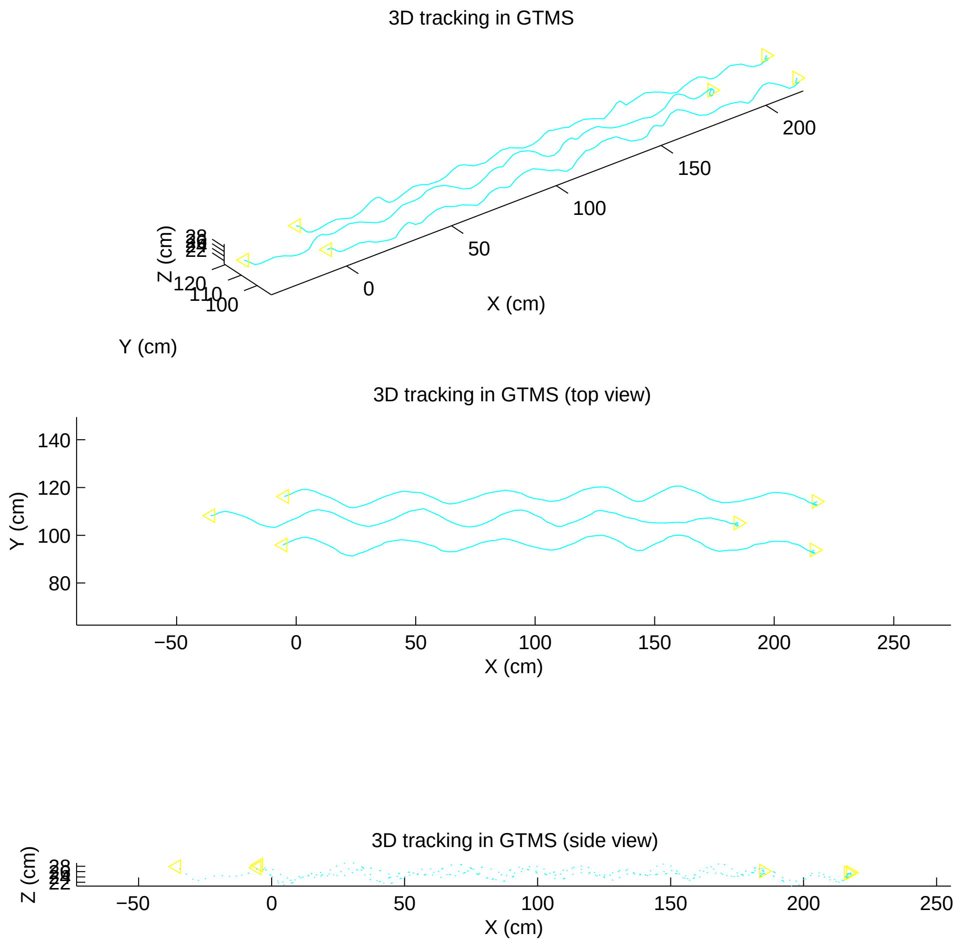

Figure A.7: Experimental data: GTMS tracking (jogging gait); three curves indicate the trajectories of three markers installed on RHex shown in Figure 4.5; X,Y,Z here indicate the absolute GTMS world frame (not the same as world frame) for RHex, which coincides with the coordinates and uses the orientation of RHex when RHex is standing on the ground before running

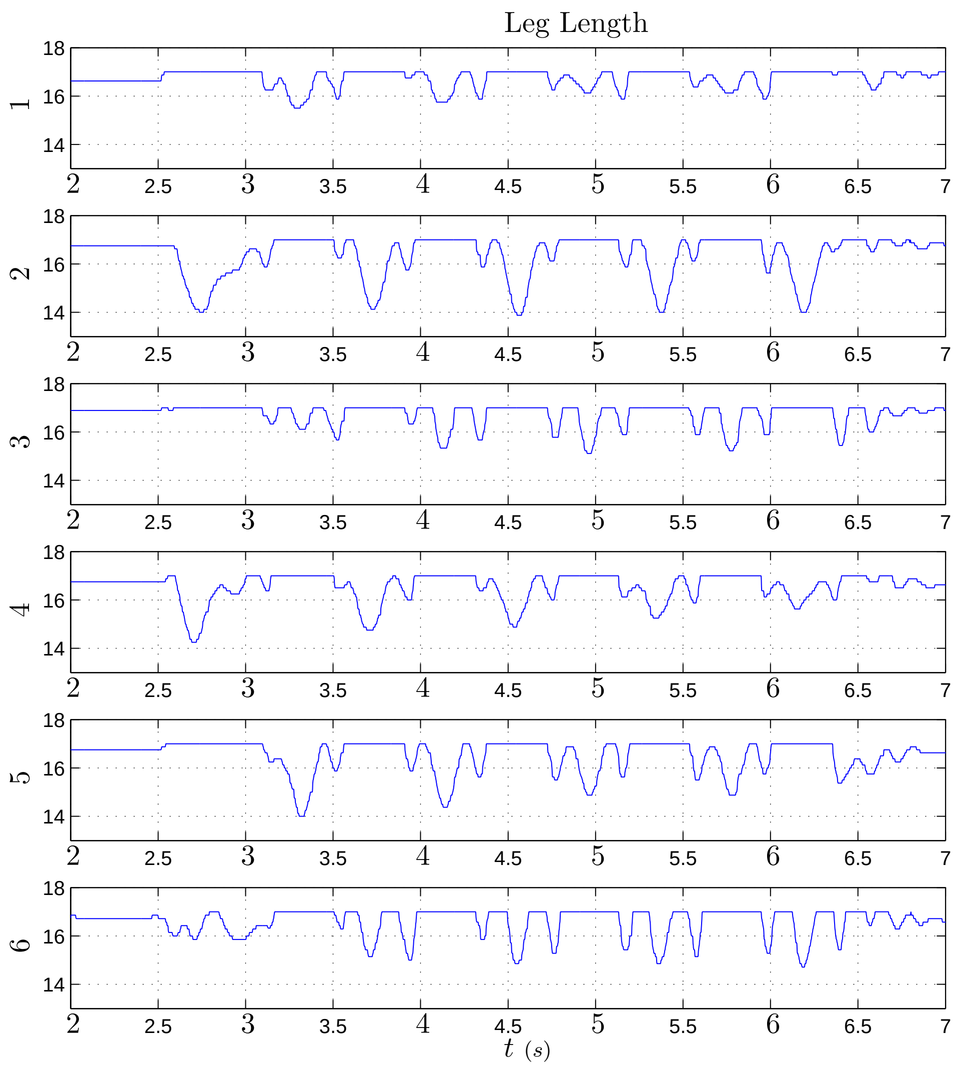

Figure A.8: Experimental data: leg length (slow walking gait); 1: left front leg, 2: left middle leg; 3: left hind leg; 4: right front leg; 5: right middle leg; 6: right hind leg

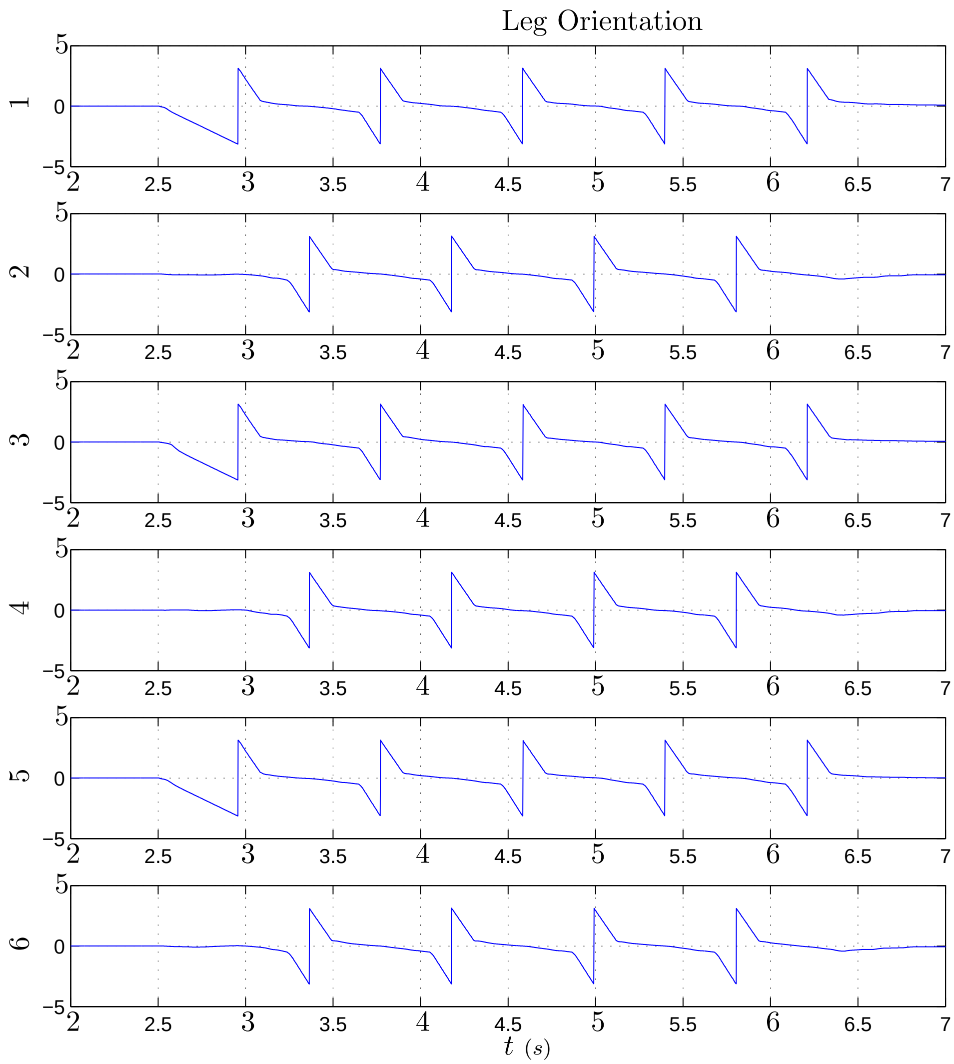

Figure A.9: Experimental data: leg orientation (slow walking gait); 1: left front leg, 2: left middle leg; 3: left hind leg; 4: right front leg; 5: right middle leg; 6: right hind leg

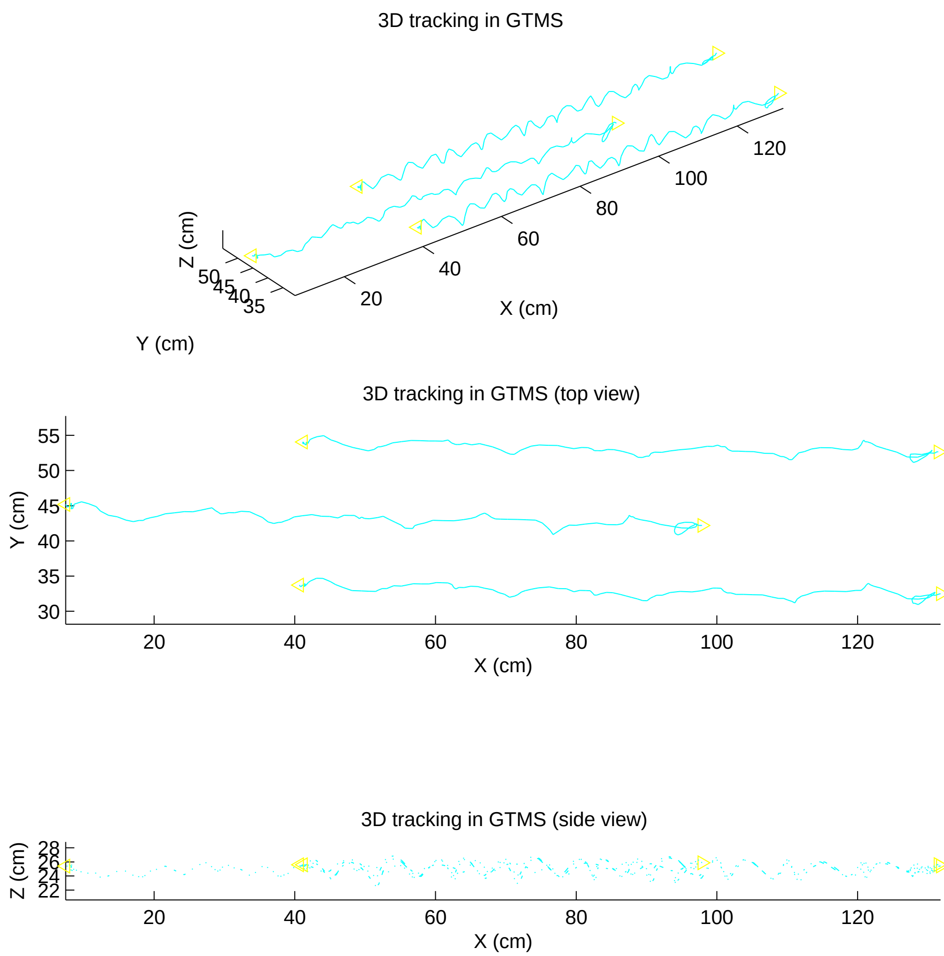

Figure A.10: Experimental data: GTMS tracking (slow walking gait); three curves indicate the trajectories of three markers installed on RHex shown in Figure 4.5; X,Y,Z here indicate the absolute GTMS world frame (not the same as world frame) for RHex, which coincides with the coordinates and uses the orientation of RHex when RHex is standing on the ground before running

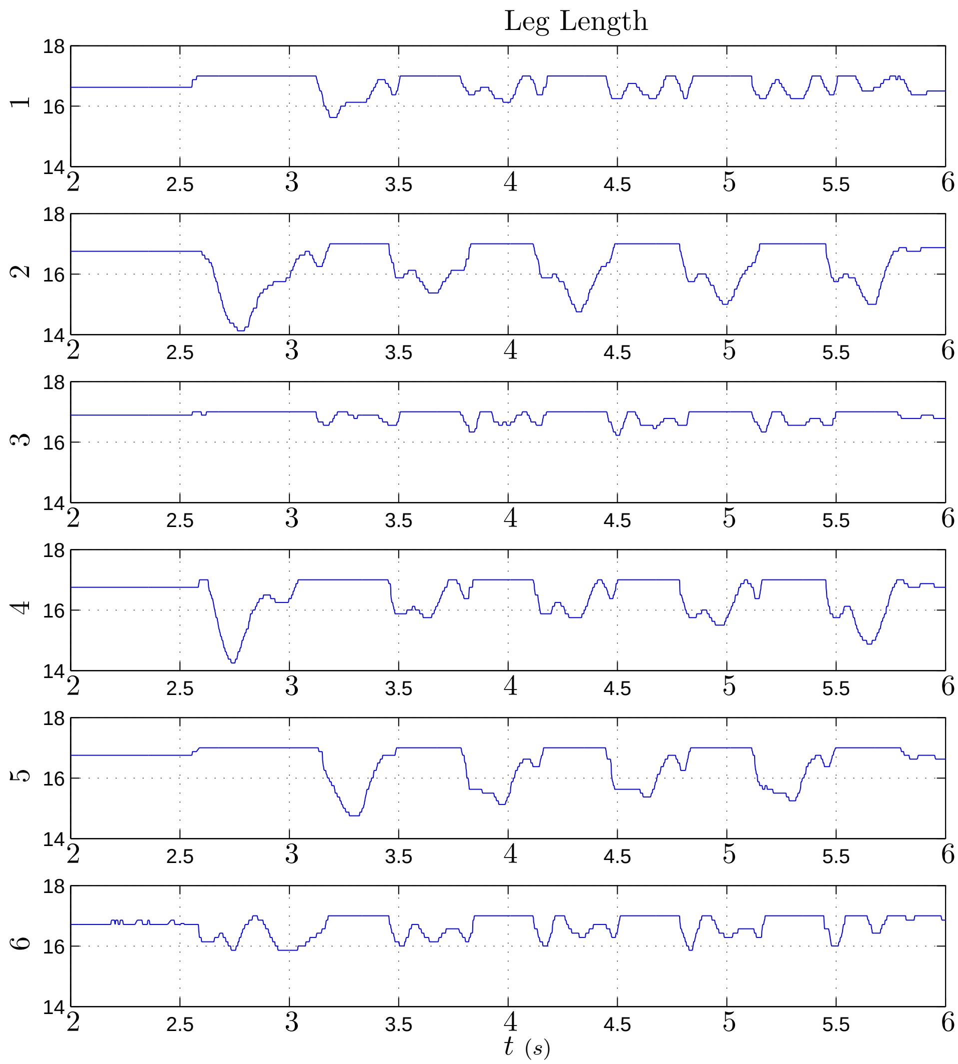

Figure A.11: Experimental data (medium walking gait): leg length; 1: left front leg, 2: left middle leg; 3: left hind leg; 4: right front leg; 5: right middle leg; 6: right hind leg

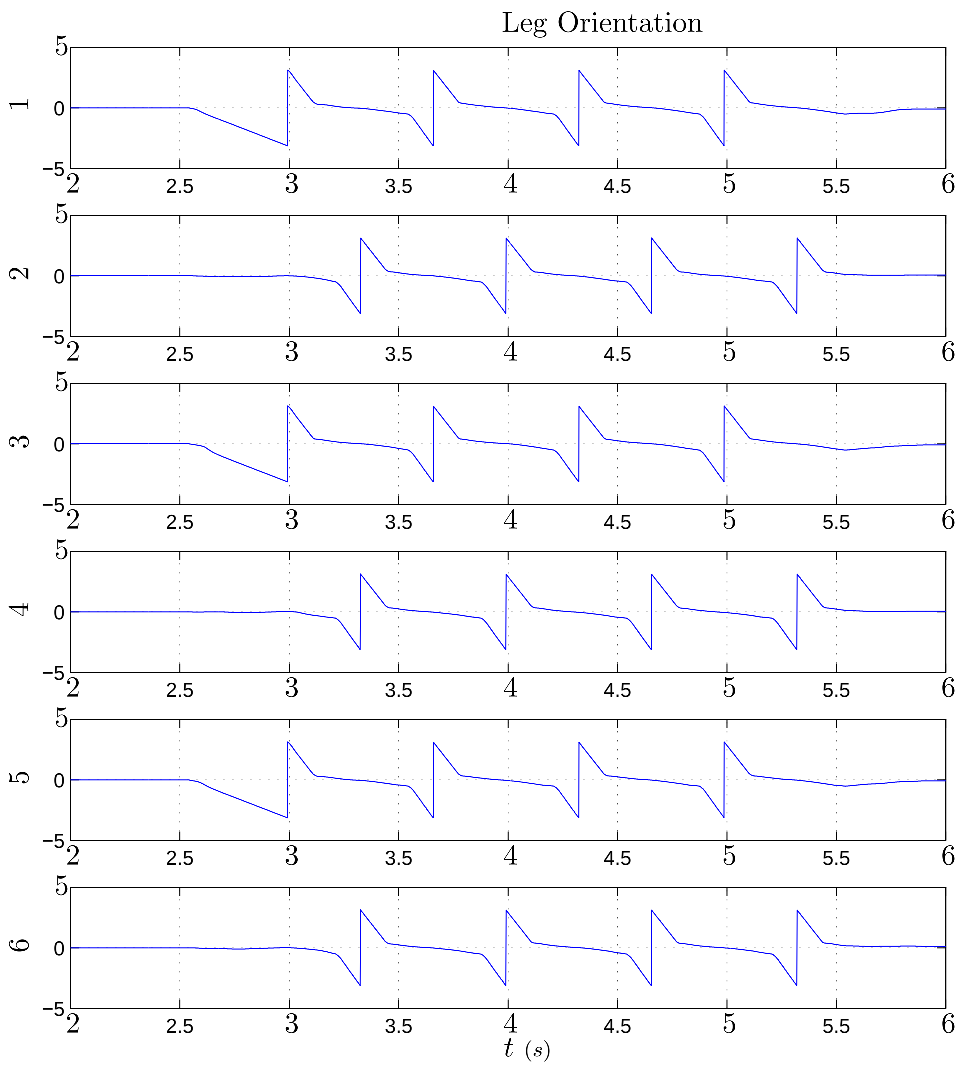

Figure A.12: Experimental data (medium walking gait): leg orientation; 1: left front leg, 2: left middle leg; 3: left hind leg; 4: right front leg; 5: right middle leg; 6: right hind leg

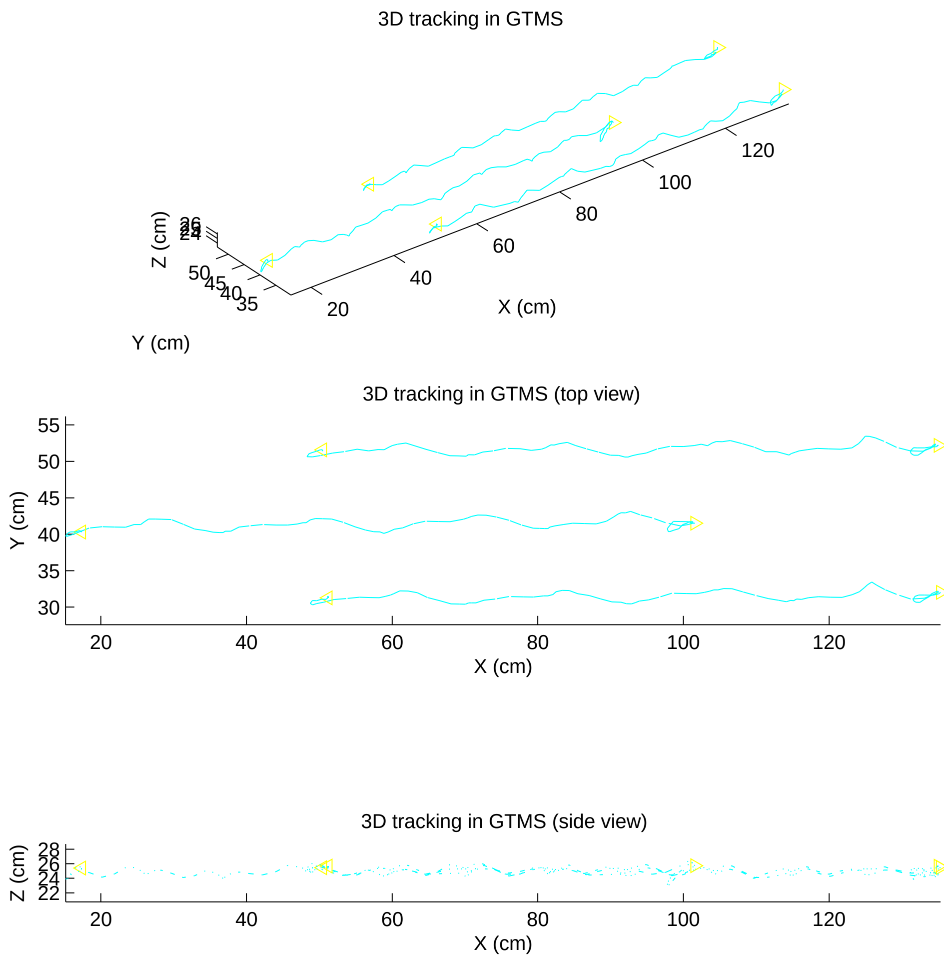

Figure A.13: Experimental data: GTMS tracking (medium walking gait); three curves indicate the trajectories of three markers installed on RHex shown in Figure 4.5; X,Y,Z here indicate the absolute GTMS world frame (not the same as world frame) for RHex, which coincides with the coordinates and uses the orientation of RHex when RHex is standing on the ground before running

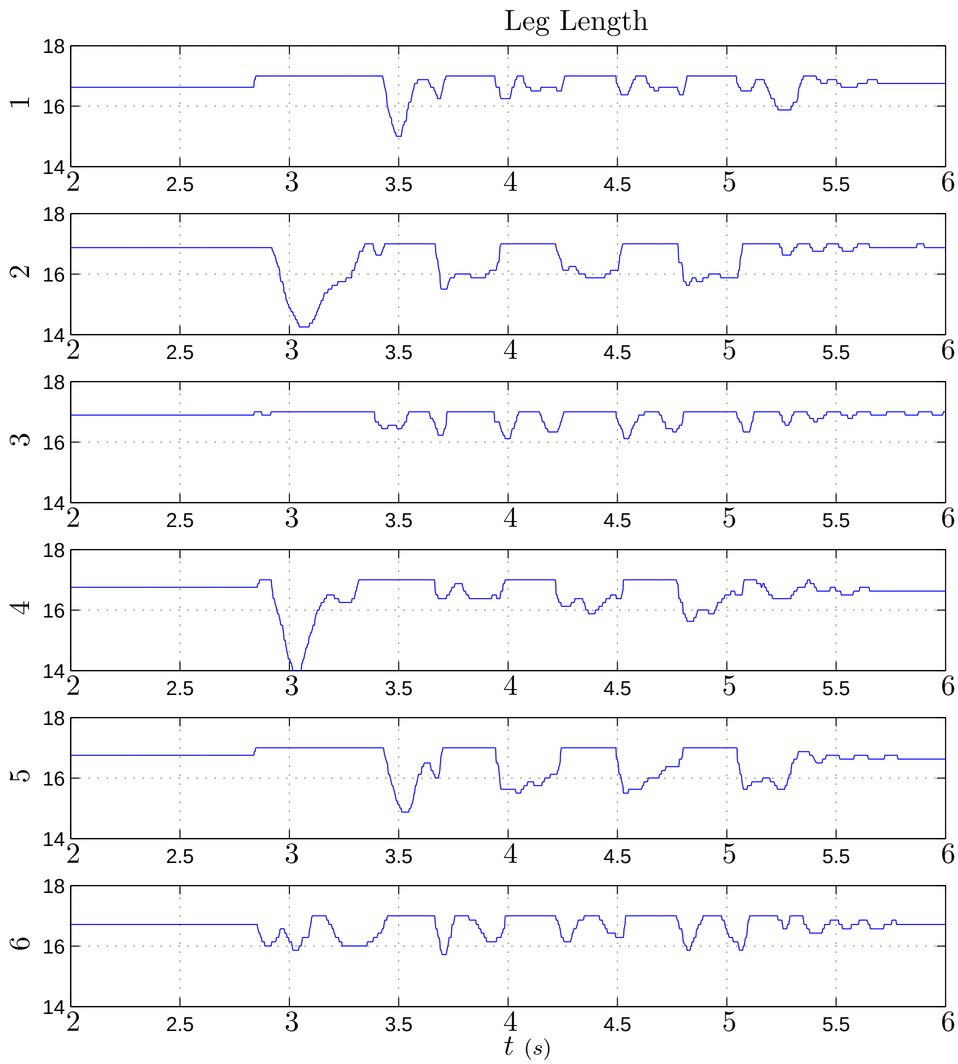

Figure A.14: Experimental data: leg length (fast walking gait); 1: left front leg, 2: left middle leg; 3: left hind leg; 4: right front leg; 5: right middle leg; 6: right hind leg

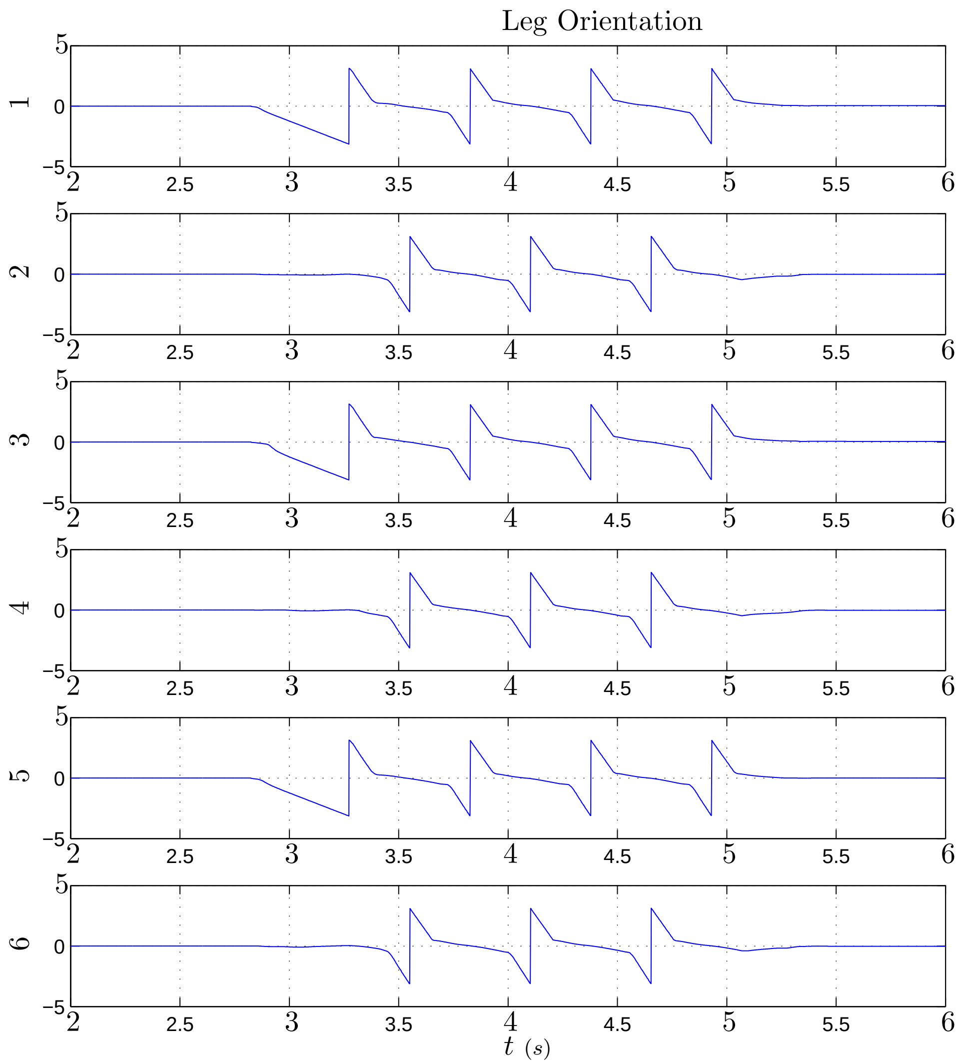

Figure A.15: Experimental data: leg orientation (fast walking gait); 1: left front leg, 2: left middle leg; 3: left hind leg; 4: right front leg; 5: right middle leg; 6: right hind leg

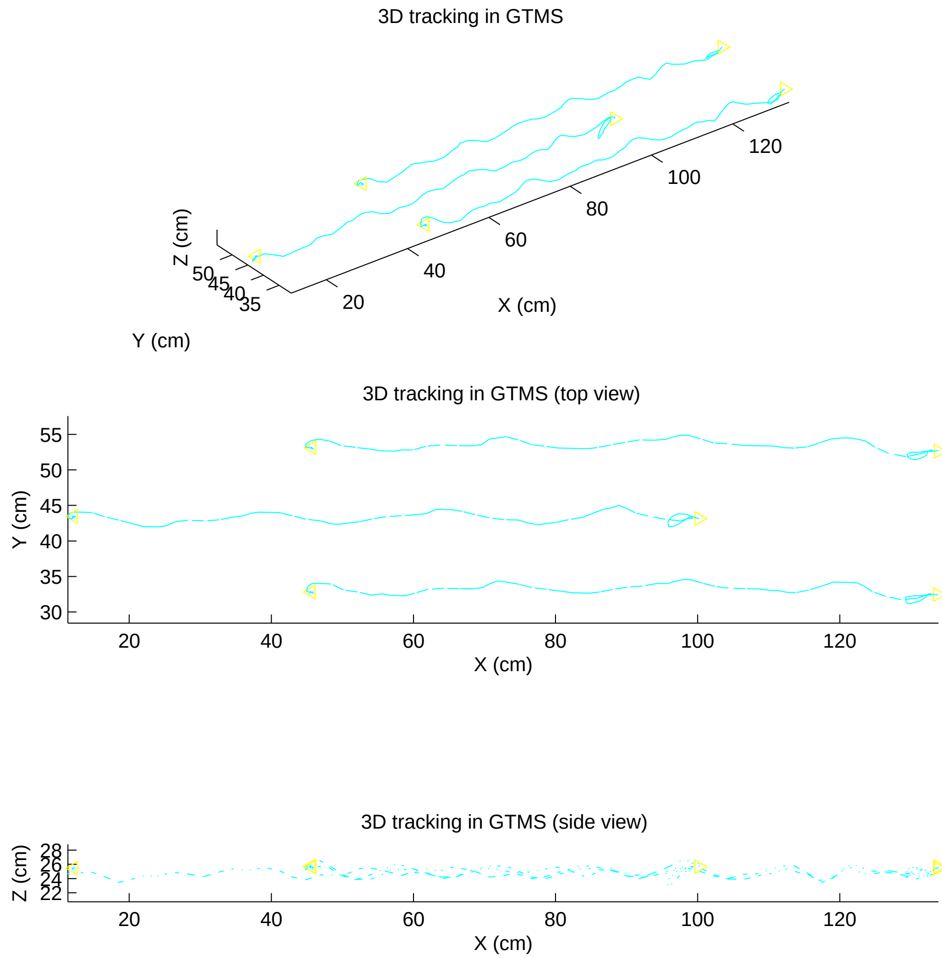

Figure A.16: Experimental data: GTMS tracking (fast walking gait); three curves indicate the trajectories of three markers installed on RHex shown in Figure 4.5; X,Y,Z here indicate the absolute GTMS world frame (not the same as world frame) for RHex, which coincides with the coordinates and uses the orientation of RHex when RHex is standing on the ground before running

APPENDIX B

Ground Compliance Identification by Leg Sensor

In addition to the body pose estimation, one of the applications of the strain-based sensory system is ground compliance identification which is followed by the fundamental idea that a robot with compliant legs performs different ground reaction patterns while running on grounds with different compliances. This capability allows the robot to operate in optimized tuned gaits regarding speed or energy efficiency for each different ground compliant level.

B.1 Basic Idea

Figure B.1 depicts the basic idea how the leg sensor can identify the ground compliance. Consider modeling the robot as a Spring Loaded Inverted Pendulum (SLIP) system where compliant legs shown in (a) acts as the spring shown in (b); by adding the model of ground with spring and damper shown in (c), the stiffness of this "resultant" spring in the final SLIP system varies depending on the spring of the ground, which results in different compression pattern of this resultant system. The leg sensor measures a partial compression pattern of the combined spring within a fixed ratio, so it is able to be scaled to represent the total compression pattern for the estimation.

Different ground conditions in the "resultant" SLIP system yield different compression patterns and causes the robot to operate in different gaits. We observe hexapod RHex yielding different compression patterns in legs even within the same parameterized walking gait but only with a different cycle time, t_c, shown in Appendix D. This increases the ability of identification by crosschecking two different grounds via multi pairs of patterns generated by different gaits. In addition, the different compression patterns in front, middle, and back legs in the actual robot due to a more complicate dynamic response is also helpful for crosschecking. As a result, $3n$ different patterns will be generated for comparison if the robot performs with n different gaits in both kinds of grounds.

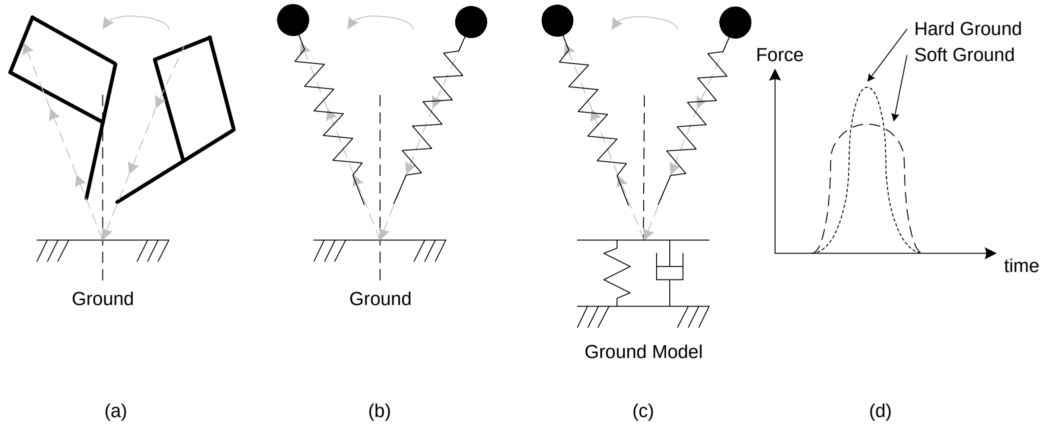

Figure B.1: Sketch describing the idea of ground compliance identification by the leg sensor

B.2 Initial Experiment Results

In order to execute this idea on a physically operating robot, we operate the robot with 4 different kinds of gaits (slow walking, medium walking, fast walking, and jogging gait) on 4 different kinds of grounds (hard ground, carpet, grass, and wood chips), and record the data from the leg sensor. After basic data processing (median filter to filter out outliers and hamming windows to smooth the curve), the initial data is shown in Figure B.2, Figure B.3, Figure B.4, and Figure B.5 according to the grounds listed above. In each experiment trial three different patterns from front, middle, and back legs belonged to the same tripod are depicted. The horizontal axis shows time fixed interval for all graphs, while the vertical axis depicts leg length in unit of centimeter.

It is clear that each plot may have different “leg compression cycles”, while each cycle is usually represented as a single large compression group in graphs. For example, 5 cycles via slow walking gait, 6 cycles via medium walking gait, 8 cycles via fast walking gait, and 9 cycles via jogging gait. The jogging gait has the fastest forward speed among all due to its shortest cycling time as well as its flight phase. Comparing the graphs with the same ground but with different gaits, it’s obvious that every gait has it’s own unique pattern; and even within the same gait, different legs (front, middle, or back) have different patterns. As a result, 12 different patterns can be generated as the comparison basis if the robot is operated robot with 4 gaits.

Comparing the graphs of a specific leg with the same gait but with different grounds does not show straight-forward differences, but reveals subtle changes that serve as the basis for comparison. Among 4 different gaits, it seems that the most significant difference in patterns appears between the slow and medium walking gaits among different grounds. This is because the robot performs multiple small vibrations during locomotion which continuously cause interaction with the surface layer of ground, which determines the shape of the compression curves. For the fast walking gait and jogging gait, the robot motion generates a large single compression curve on legs, which is more like the SLIP model. However, that kind of motion performs a big force interaction (big compression), penetrating into the hard ground under the shallow surface layer of carpet, grass, or wood chips. Meaning that the influence of models of the shallow surface layer may become insignificant. Therefore, we can treat these two gaits as actually working with the similar hard ground so that we are not able to get pattern differences.

B.3 Future Research Procedure

Based on the observation from the graphs shown in Section B.2, extracting special features from the patterns is the first step. A few candidate features are:

- Number of peaks in one compression cycle
- Time for compression in one compression cycle
- Amplitude of maximum compression
- Ratio of compression timing between peaks in the same cycle
- Ratio of compression amplitudes between peaks in the same cycle

The next step is to use the technique of pattern recognition to check if these features are able to distinguish data sets among different ground, appearing in different regions in scatter plots. If the answer is negative, try to extract other features, repeating the process. The sensor noise may deteriorate the whole work if the noise floor of the sensor is close to or larger than the differences among patterns resulting from different ground compliance. This need to be checked after achieving precise experiment results as well as the features from the data of different experiment trials.

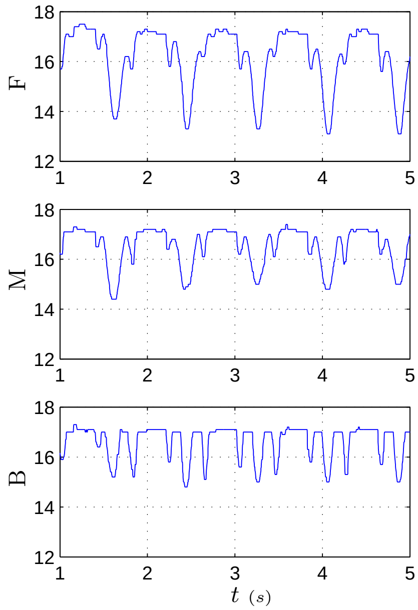

(a)

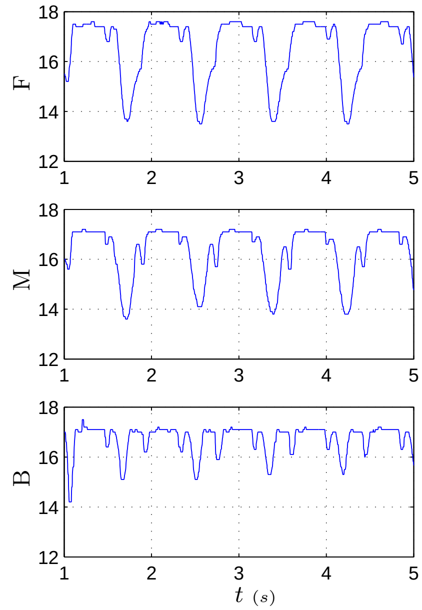

(b)

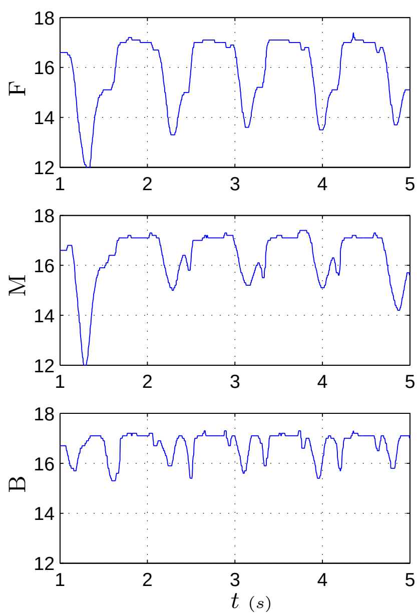

(c)

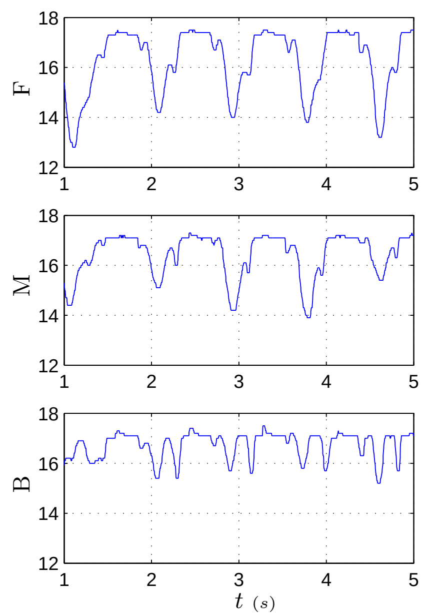

(d)

Figure B.2: Leg compression patterns with different ground conditions (slow walking gait): (a) on hard ground (b) on carpet (c) on grass (d) on wood chips; F: front leg, M: middle leg, B: back leg

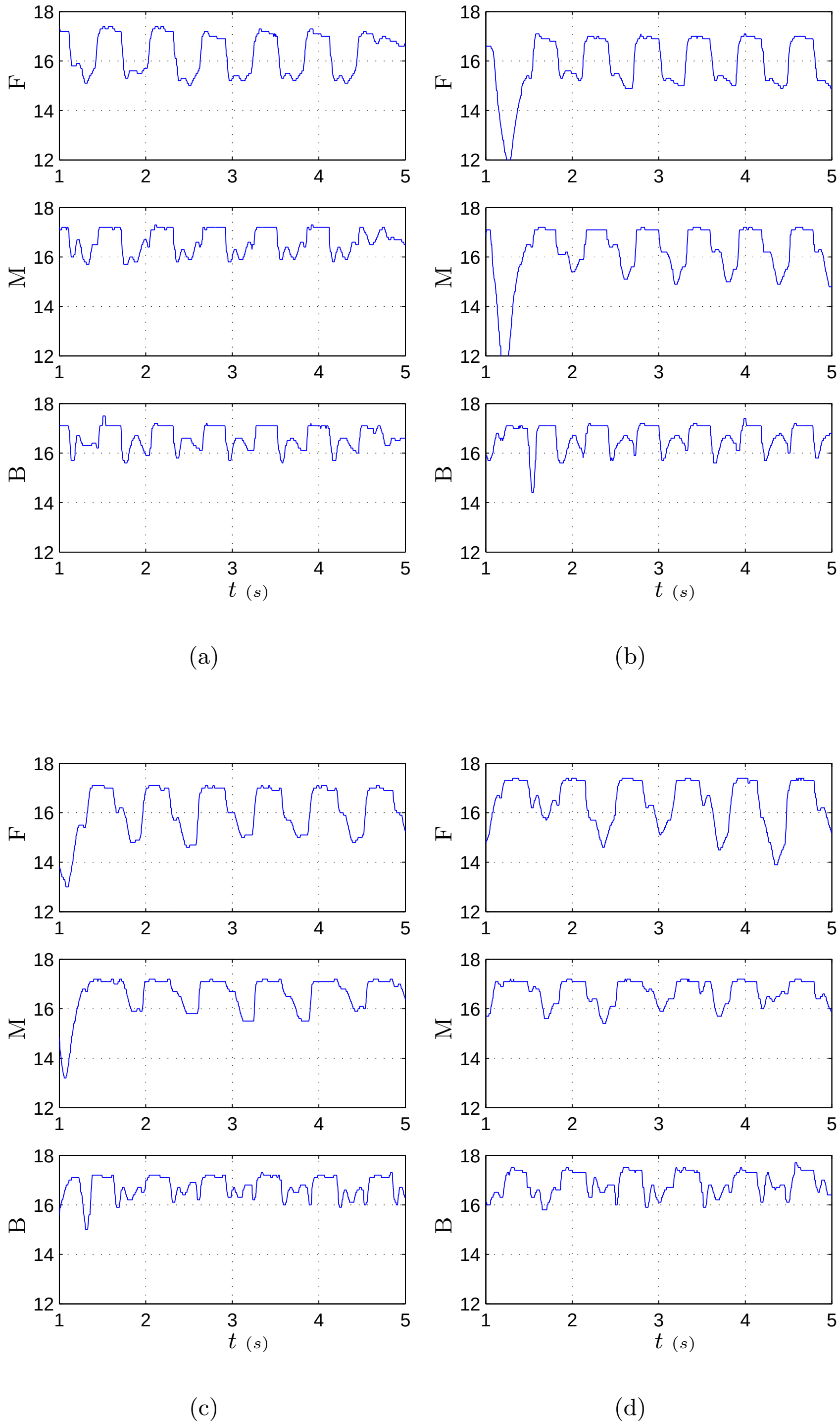

Figure B.3: Leg compression patterns with different ground conditions (medium walking Gait): (a) on hard ground (b) on carpet (c) on grass (d) on wood chips; F: front leg, M: middle leg, B: back leg

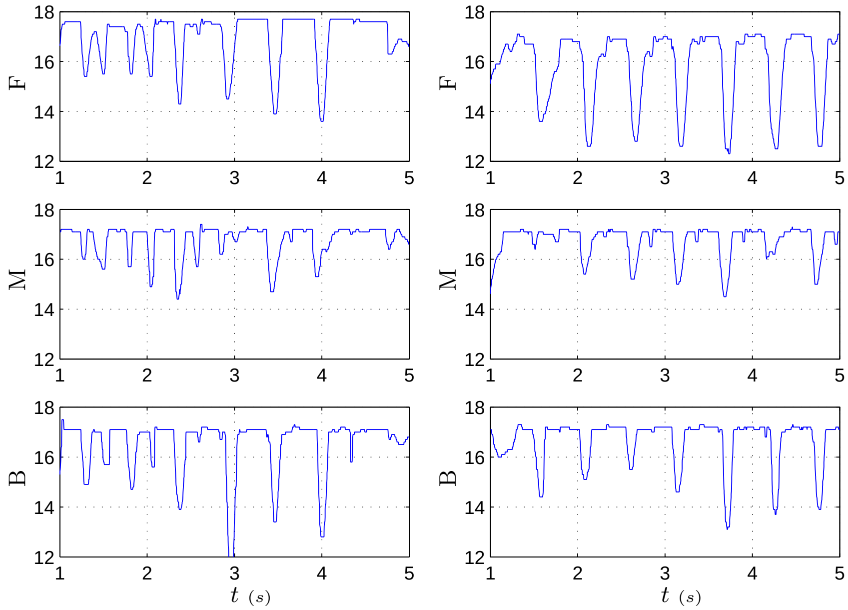

(a) (b)

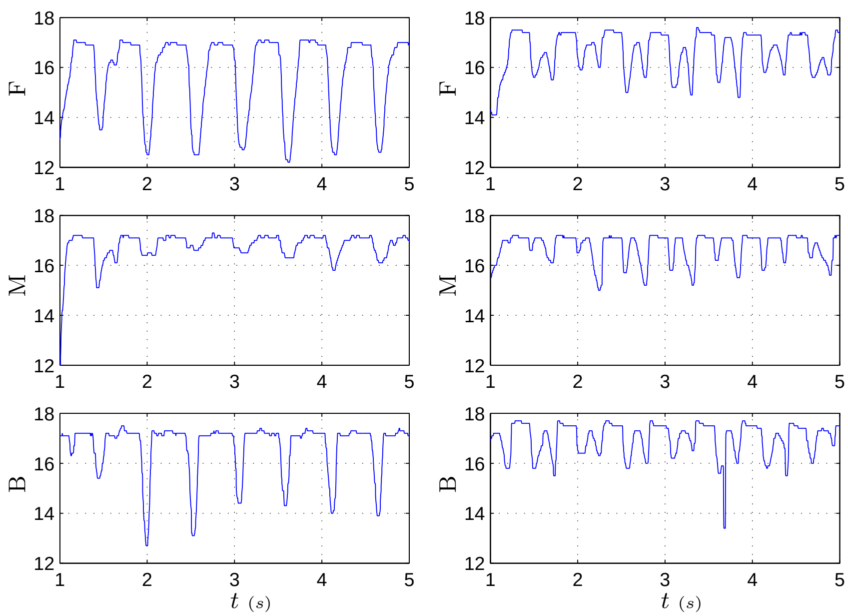

(c) (d)

Figure B.4: Leg compression patterns with different ground conditions (fast walking gait): (a) on hard ground (b) on carpet (c) on grass (d) on wood chips ; F: front leg, M: middle leg, B: back leg

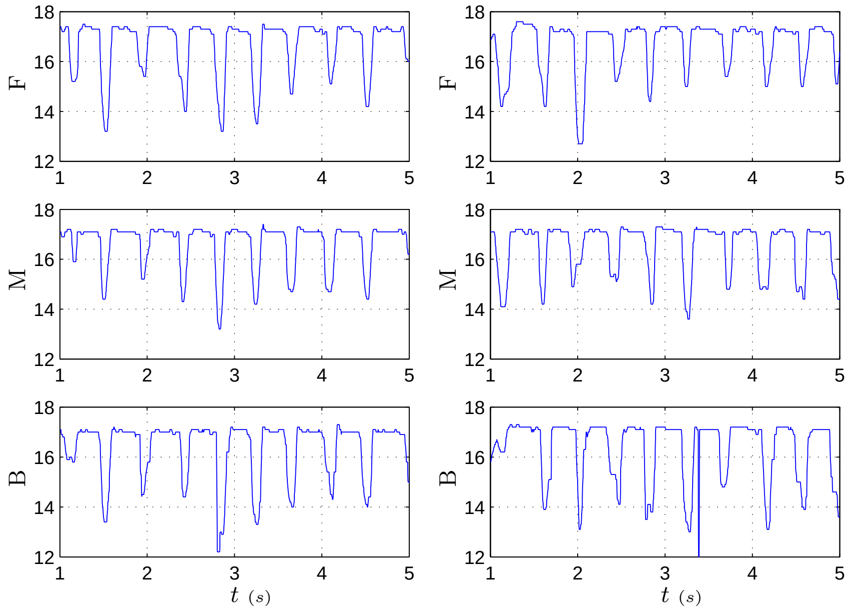

(a) (b)

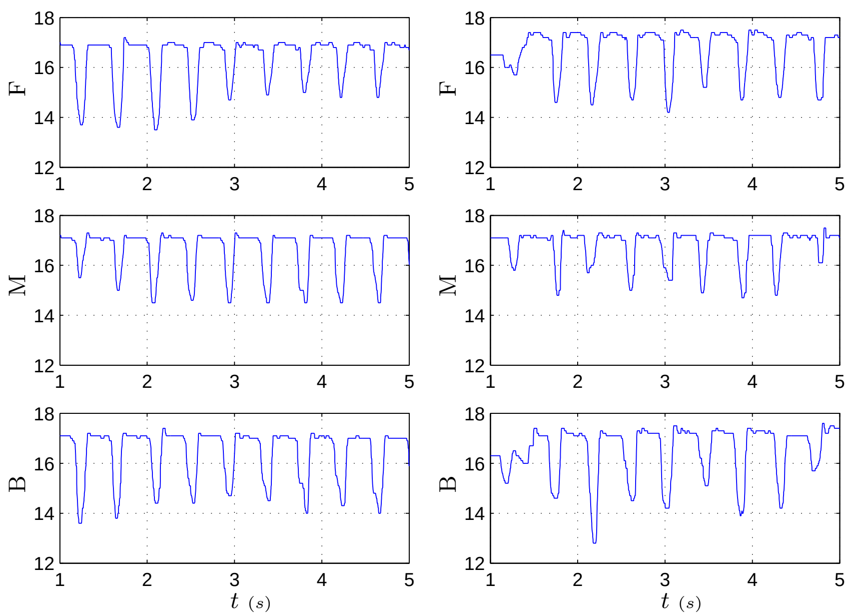

(c) (d)

Figure B.5: Leg compression patterns with different ground conditions (jogging gait): (a) on hard ground (b) on carpet (c) on grass (d) on wood chips ; F: front leg, M: middle leg, B: back leg

APPENDIX C

Evaluation of the Ground Reaction Force Model

The basic method for evaluating the ground reaction force model is to measure the actual ground reaction forces and to compare the force data from the external force sensor to that from the model output of the leg sensor. Figure C.1 proposes an empirical setup for this evaluation. In this setup, we let the robot walk/run on level path so that one of the middle legs strikes on a prepared "force plate" supported by two 3-axis force sensor only, which records the forces transmitted from the leg to the ground. Ideally, the force measured by the force sensor and the force measured between toe and the ground would result in a specific relationship based on the geometrical dimensions. Figure C.2 depicts the free body diagram (FBD) with all of the force components, which indicates the relation between the ground reaction forces and the forces from both force sensors as

$$\begin{aligned} f_n &= f_{n\_1} + f_{n\_2} \\ f_f &= f_{f\_1} + f_{f\_2} \end{aligned} \tag{C.1}$$

which also provides the location of leg touchdown to form the equilibrium equation

$$\frac{r_1}{r_2} = \frac{f_{n\_2}}{f_{n\_1}}. \tag{C.2}$$

Unlike the leg model based on certain assumptions, the measurement by the force plate will not be affected by the region of robot operation (either dynamic or quasistatic) since the measurement is directly taken from the force field.

Data from these two force sensors can be collected by importing raw sensor data into the customized PC104 stack used in the benchtop experiment table described in Section 3.4. The LED on top of the robot signals the start time for the measurement of the robot data with the force plate data.

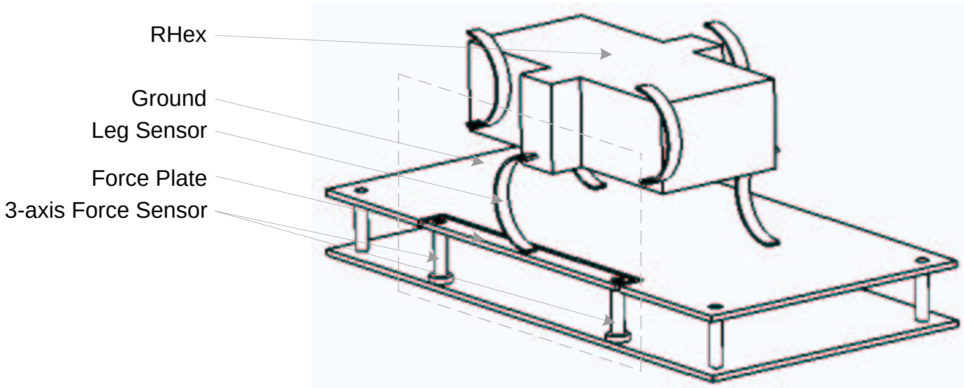

Figure C.1: Force plate experimental test station

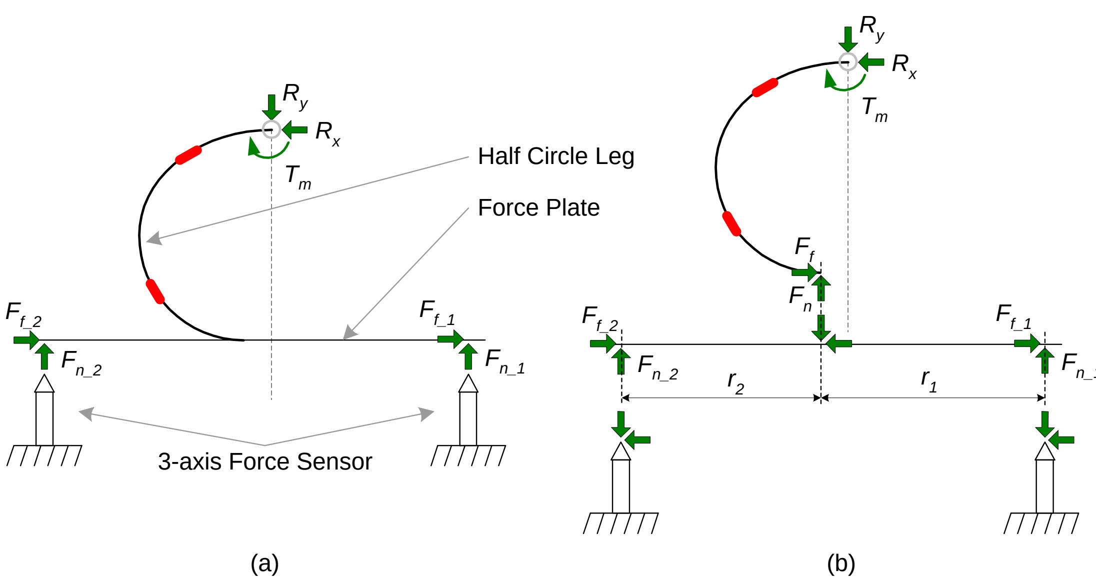

Figure C.2: Free body diagram of the force plate experimental test station: (a) FBD for the whole system (b) decoupled FBD

APPENDIX D

Buehler Clock

The open loop control strategy of RHex's legs for tripod gaits, usually called "Buehler Clock [SBK01]", works using 4 parameters: t_c, t_s, ϕ_s and ϕ_o shown in Figure D.1. This is a periodic function of time composed by slow and fast swing phases, denoted by ϕ_s and $2\pi - \phi_s$ accordingly. The slow swing phase is used for pushing the robot in walking or running, while the fast swing phase is for quick return to support the continuous pushing motion in slow swing phase. Both phases are in constant rotation speeds with a 3 order polynomial as a smoothing function in between. Summed time for both profiles for a single cycle is defined as t_c. In conjunction with t_s, defined as the time for a slow swing phase, it determines the duty factor. Finally, the ϕ_o parameter offsets the motion profile of the slow swing phase with respect to the vertical.

For the walking gait and jogging gait, the six legs have exactly the same parameters in the Buehler Clock, but are grouped as two tripods synchronized with each other, 180^0 out of phase with the opposite tripod for continuous locomotion. The duration of the "ideal" double stand, t_d, when all six legs are in contact with the ground, is determined by the duty factors of both tripods. Even with only 4 parameters, the robot performs significant different behaviors via different parameter settings, from slow walking, to energy efficient jogging, and to high speed running [WLK04].

The gait for turning in place shares the same parameters in the Buehler Clock, having 180^0 out of phase between the two tripods. These two tripods rotate in the opposite direction to initiate toe slippage on some legs to generate the turning motion, which is the only method due to RHex's simple 1 rotational DOF per leg mechanism. Thus, this torque-requiring motion easily results in quick heat-up of motors. Proportional turning is done by offsetting ϕ_0 in different directions on each side of legs, resulting in a big roll angle during motion to redistribute the ground reaction force among legs, so that slippage happens easier on one side of legs. This generates the combination motion of forward and turning similar to the turning method of automobiles.

Though RHex has a total of only 6 active rotational DOF to generate leg motion, it is still unclear to us how to excite the "right" behavior, either by designing the "right"

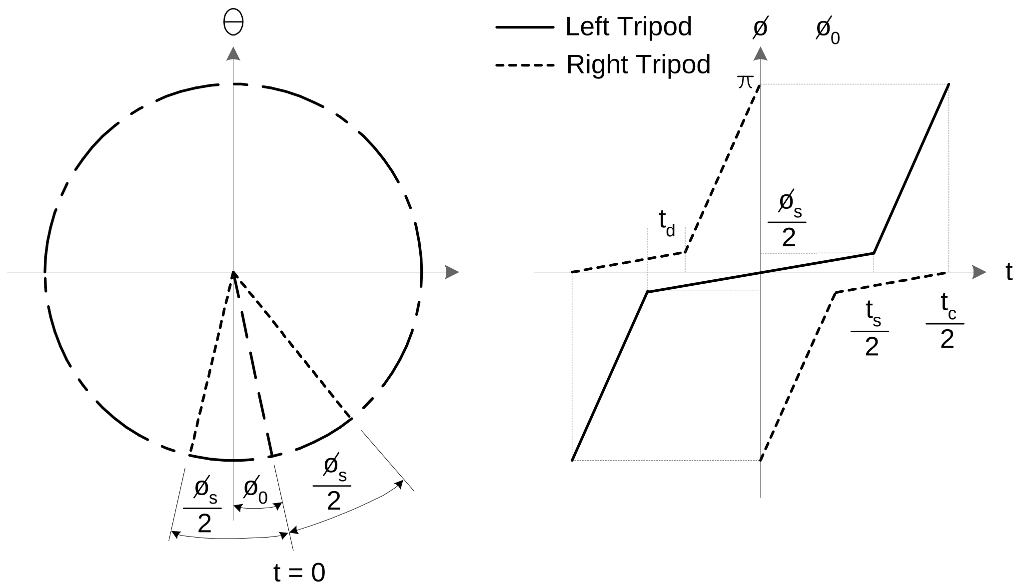

Figure D.1: Buehler Clock: (a) sketch in leg orientation (b) sketch in phase vs. time

trajectory of the legs or assigning the "right" torque to the joints over time. Different leg motions significantly effect the pattern of energy storage/release which plays an important role in determining the dynamic behavior of the robot. Currently most of the gaits are assigned/tuned with certain open loop leg trajectories by intuition or by a mathematical optimization procedure without insight from the physics point of view. This is a challenging problem since this faces a similar situation to my development of state estimation detailed in Chapter 6, where all procedures are linked in a circular path without an obvious start point — requiring good behaviors to find good models, but also good models to generate good behaviors. Another dilemma lies in the question of what the "correct" template is for each behavior and how to anchor it [FK99]. The simpler the template, the easier it is to control, but the harder it is to anchor. There is also the possibility of losing certain advantages inherent to the original more complicate physical system. With these considerations, we are working toward the goal of a feedback controller to operate robots in stable and desired behaviors.

BIBLIOGRAPHY

BIBLIOGRAPHY

[AA02] M. Abdelrahman and P. Abdelrahman, *Integration of multiple sensor fusion in controlled design*, Proc. of the American Control Conference, vol. 4, May 2002, pp. 2609–2614.

[AH96] K. Arikawa and S. Hirose, *Development of quadruped walking robot titan-viii*, Proc. of the IEEE/RSJ International Conference on Intelligent Robots and Systems, Osaka, Japan, vol. 1, 1996, pp. 208–214.

[AKH04] R. Altendorfer, D. E. Koditschek, and P. Holmes, *Stability analysis of a clock-driven rigid-body slip model for RHex*, The International Journal of Robotics Research **23** (2004), no. 11, 1001–1012.

[AKR03] W. T. Ang, P. K. Khosla, and C. N. Riviere, *Design of all-accelerometer inertial measurement unit for tremor sensing in hand-held microsurgical instrument*, Proc. of the IEEE International Conference on Robotics and Automation, Taipei, Taiwan, vol. 2, 2003, pp. 1781–1786.

[AMK+01] R. Altendorfer, N. Moore, H. Komsuoglu, H. B. Brown, D. McMordie, U. Saranli, R. Full, and D. E. Koditschek, *RHex: A biologically inspired hexapod runner*, Autonomous Robots **11** (2001), no. 3, 207–213.

[Ang91] A. Angle, *Design of an artificial creature*, Master's thesis, MIT, 1991.

[AWM+00] J. Ayers, J. Witting, N. McGruer, C. Olcott, and D. Massa, *Lobster robots*, Proc. of the International Symposium on Aqua Biomechanisms, 2000.

[AWW+00] J. Ayers, J. Witting, C. Wilbur, P. Zavracky, N. McGruer, and D. Massa, *Biomimietic robots for shallow water mine countermeasurements*, Proc. of the Autonomous Vehicles in Mine Countermeasures, 2000.

[BA02] G. A. Borges and M.-J. Aldon, *Optimal mobile robot pose estimation using geometrical maps*, IEEE Transactions on Robotics and Automation **18** (2002), no. 1, 87–94.

[BAL00] A. Bonarini, P. Aliverti, and M. Lucioni, *An omnidirectional vision sensor for fast tracking for mobile robots*, IEEE transactions on Instrumentation and Measurement **49** (2000), no. 3, 509–512.

[BCI94] K. Berns, S. Cordes, and W. Ilg, *Adaptive, neural control architecture for the walking machine lauron*, Proc. of the IEEE/RSJ International Conference on Intelligent Robots and Systems, Munich, Germany, 1994, pp. 1172–1177.

[BDW95] B. Barshan and H. F. Durrant-Whyte, *Inertial navigation systems for mobile robots*, IEEE Transactions on Robotics and Automation **11** (1995), no. 3, 328–342.

[BEFW97] J. Borenstein, H. R. Everett, L. Feng, and D. Wehe, *Mobile robot positioning: Sensors and techniques*, Journal of Robotic Systems **14** (1997), no. 4, 231–249.

[Bev04] D. M. Bevly, *Global positioning system (GPS): A low-cost velocity sensor for correcting inertial sensor errors on ground vehicles*, Journal of Dynamic Systems, Measurement and Control, Transactions of the ASME **126** (2004), no. 2, 255–264.

[BF96a] J. Borenstein and L. Feng, *Gyrodometry: A new method for combining data from gyros and odometry in mobile robots*, Proc. of the IEEE International Conference on Robotics and Automation, Minneapolis, MN., vol. 1, 1996, pp. 423–428.

[BF96b] ———, *Measurement and correction of systematic odometry errors in mobile robots*, IEEE Transactions on Robotics and Automation **12** (1996), no. 6, 869–880.

[BG01] D. Bouvet and G. Garcia, *Guaranteed 3-d mobile robot localization using an odometer, an automatic theodolite and indistinguishable landmarks*, Proc. of the IEEE International Conference on Robotics and Automation, Seoul, Korea, vol. 4, 2001, pp. 3612–3617.

[BhFDW95] B. Barshan and h. F. Durrant-Whyte, *Evaluation of a solid-state gyroscope for robotics applications*, IEEE transactions on Instrument and Measurement **44** (1995), no. 1, 61–67.

[BNDW98] M. Bozorq, E. M. Nebot, and H. F. Durrant-Whyte, *Decentralized navigation architecture*, Proc. of the IEEE International Conference on Robotics and Automation, Leuven, Belgium, vol. 4, May 1998, pp. 3413–3418.

[Bre93] Cynhthia Breazeal, *Robust agent control of an autonomous robot with many sensors and actuators*, Master's thesis, MIT, 1993.

[Bro89] R. A. Brooks, *A robot that walks; emergent behaviors from a carefully evolved network*, Tech. report, MIT, 1989.

[BS01] N. Barbour and G. Schmidt, *Inertial sensor technology trends*, IEEE Sensors Journal **1** (2001), no. 4, 332–339.

[BSK02] M. Buehler, U. Saranli, and D. E. Koditschek, *Single actuator per leg robotic hexapod*, McGill University, The Regents of the University of Michigan, USA, Nov 2002, United States Patent, 6,481,513.

[BSW00] P. Buschka, A. Saffiotti, and Z. Wasik, *Fuzzy landmark-based localization for a legged robot*, Proc. of the IEEE/RSJ International Conference on Intelligent Robots and Systems, Takamatsu, Japan, vol. 2, 2000, pp. 1205–1210.

[BZ98] H. B. Brown and G. Z. Zeglin, *The bow leg hopping robot*, Proc. of the IEEE International Conference on Robotics and Automation, Leuven, Belgium, vol. 1, 1998, pp. 781–786.

[CA78] C. B. Chang and M. Athans, *State estimation for discrete systems with switching parameterse*, IEEE Transactions on Aerospace and Electronic Systems **14** (1978), no. 3, 418–425.

[CB03] D. Campbell and M. Buehler, *Stair descent in the simple hexapod 'RHex'*, Proc. of the IEEE International Conference on Robotics and Automation, Taipei, Taiwan, vol. 1, Sep 2003, pp. 1380–1385.

[CBC+02] J. G. Cham, S. A. Bailey, J. E. Clark, R. J. Full, and M. R. Cutkosky, *Fast and robust: Hexapedal robots via shape deposition manufacturing*, The International Journal of Robotics Research **21** (2002), no. 10, 869–882.

[CBL97] S. Cordes, K. Berns, and I. Leppanen, *Sensor components of the six-legged walking machine lauron ii*, Proc. of the International Conference on Advanced Robotics, 1997.

[CKC04] J. G. Cham, J. K. Karpick, and M. R. Cutkosky, *Stride period adaptation for a biomimetric running hexapod*, The International Journal of Robotics Research **23** (2004), no. 2, 141–153.

[CLD94] J. Chen, S. Lee, and Daniel B. DeBra, *Gyroscope free strapdown inertial measurement unit by six linear accelerometers*, Journal of Guidance, Control, and Dynamics **17** (1994), no. 2, 286–290.

[COB01] H. Chung, L. Ojeda, and J. Borenstein, *Accurate mobile robot dead-rockoning with a precision-calibrated fiber-optic gyroscope*, IEEE Transactions on Robotics and Automation **17** (2001), no. 1, 80–84.

[Dez99] J. Dezert, *Improvement of strapdown inertial navigation using pdaf*, IEEE transactions on Aerospace and Electronic Systems **35** (1999), no. 3, 835–856.

[DFF+00] M. H. Dickinson, C. T. Farley, R. J. Full, M. A. R. Koehl, R. Kram, and S. Lehman, *How animals move: An integrative view*, Science **288** (2000), 100–106.

[DMC00] L. Drolet, F. Michaud, and J. Cote, *Adaptable sensor fusion using multiple kalman filters*, Proc. of the IEEE/RSJ International Conference on Intelligent Robots and Systems, Takamatsu, Japan, vol. 2, Oct 2000, pp. 1434–1439.

[DN00] F. Delcomyn and M. E. Nelson, *Architectures for a biomimetic hexapod robot*, Robotics and Autonomous Systems **30** (2000), no. 1, 5–15.

[DSNDW99] G. Dissanayaka, S. Sukkarieh, E. Nebot, and H. F. Durrant-Whyte, *A new algorithm for the alighment of inertial measurement units without external observation for land vehicle application*, Proc. of the IEEE International Conference on Robotics and Automation, Detroit, MI, vol. 3, May 1999, pp. 2274–2279.

[DSNDW01] ______, *The aiding of a low-cost strapdown inertial measurement unit using vehicle model constraints for land vehicle applications*, IEEE Transactions on Robotics and Automation **17** (2001), no. 5, 731–747.

[EAM01] P. J. Escamilla-Ambrosio and N. Mort, *A hybrid kalman filter - fuzzy logic architecture for multisensor data fusion*, Proc. of the IEEE International Symposium on Intelligent Control, Sep 2001, pp. 364–369.

[EETP99] I. Erkmen, A. M. Erkmen, A. E. Tekkaya, and T. Pasinlioglu, *Haptic perception of shape and hollowness of deformable objects using the anthrobot-iii robot hand*, Journal of Robotic Systems **16** (1999), no. 1, 9–24.

[ER02] A. El-Rabbany, *Introduction to gps: The global positioning system*, 1 ed., Artech House Publishers, 2002.

[FAH+95] T. Fukuda, Y. Adachi, H. Hoshino, K. Kosuge, I. Matsunaga, and F. Arai, *Posture control of six-leg walking robot*, Proc. of the IEEE International Conference on Robotics and Automation, Nagoya, Japan, vol. 1, 1995, pp. 1006–1011.

[FGM93] C. T. Farley, J. Glasheen, and T. A. McMahon, *Running springs: Speed and animal size*, Journal of Experimental Biology **185** (1993), 71–86.

[FhKC03] Y. Fukuoka, h. Kimura, and A. H. Cohen, *Adaptive dynamic walking of a quadruped robot on irregular terrain based on biological concepts*, The International Journal of Robotics Research **22** (2003), no. 3-4, 187–202.

[FK99] R. J. Full and D. E. Koditschek, *Templates and anchors - neuromechanical hypotheses of legged locomotion on land*, Journal of Experimental Biology **202** (1999), 3325–3332.

[FT00a] F. A. Faruqi and K. J. Turner, *Extended kalman filter synthesis for integrated global positioning/inertial navigation systems*, Applied Mathematics and Computation **115** (2000), no. 2, 213–227.

[FT00b] ______, *Non-linear mathematical model for integrated global positioning/inertial navigation systems*, Applied Mathematics and Computation **115** (2000), no. 2, 191–212.

[FTPHBB00] E. D. Ferreira, S. Tsai, C. J.J. Paredis, and Jr. H. B. Brown, *Control of the gyrover: A single-wheel gyroscopically stabilized robot*, Advanced Robotics **14** (2000), no. 6, 459–475.

[GASH01] G. Grenon, P. Edgar An, S. M. Smith, and A. J. Healey, *Enhancement of the inertial navigation system for the morpheus autonomous underwater vehicles*, IEEE Journal of Oceanic Engineering **26** (2001), no. 4, 548–560.

[GBPB04] C. Grand, F. Benamar, F. Plumet, and P. Bidaud, *Stability and traction optimization of a reconfigurable wheel-legged robot*, The International Journal of Robotics Research **23** (2004), no. 10-11, 1041–1058.

[GHM91] M. Grewal, V. D. Henderson, and R. S. Miyasako, *Application of kalman filtering to the calibration and alignment of inertial navigation systems*, IEEE Transactions on Automatic Control **36** (1991), no. 1, 4–13.

[GJ02] R. A. Grupen and J. A. Coelho Jr., *Acquiring state from control dynamics to learn grasping policies for robot hands*, Advanced Robotics **16** (2002), no. 5, 427–443.

[GMR01] M. Golfarelli, D. Maio, and S. Rizzi, *Correction of dead-reckoning errors in map building for mobile robots*, IEEE Transactions on Robotics and Automation **17** (2001), no. 1, 37–47.

[Gor99] P. Gorce, *Dynamic postural control method for biped in unknown environment*, IEEE Transactions on Robotics and Automation **29** (1999), no. 6, 616–626.

[Gre95] R. L. Greenspan, *Inervial navigation technology from 1970-1995*, Jounral of the Institute of Navigation **42** (1995), no. 1, 165–185.

[GRS99] P. Goel, S. I. Roumeliotis, and G. S. Sukhatme, *Robust localization using relative and absolute position estimate*, Proc. of the IEEE International Conference on Robotics and Automation, Detroit, MI, vol. 2, 1999, pp. 1134–1140.

[GSB01] B. Gamann, K.-U. Scholl, and K. Berns, *Locomotion of lauron iii in rough terrain*, Proc. of the International Conference on Advanced Mechatronics, 2001.

[GZZD05] B. Gassmann, F. Zacharias, J. M. Zollner, and R. Dillmann, *Localization of walking robots*, Proc. of the IEEE International Conference on Robotics and Automation, Barcelona, Spain, Apr 2005, pp. 1483–1488.

[HKA97] K. Hosoda, M. Kamado, and M. Asada, *Vision-based servoing control for legged robots*, Proc. of the IEEE International Conference on Robotics and Automation, Albuquerque, NM, vol. 4, 1997, pp. 3154–3159.

[HMA03] R. Hoseinnezhad, B. Moshiri, and M. R. Asharif, *Improved pose estimation for mobile robots by fusion of odometry data and environment map*, Journal of Intelligent and Robotic Systems **36** (2003), no. 1, 89–108.

[HR88] D. Halliday and R. Resnick, *Fundamentals of physics*, John Wiley and Sons, Inc, 1988, p104-109.

[HS96] U. D. Hanebeck and G. Schmidt, *Localization of fast mobile robots based on an advanced angle-measurement technique*, Control Engineering Practice **4** (1996), no. 8, 1109–1118.

[IH01] A. Inmann and M. Haugland, *An instrumented object for evaluation of lateral hand grasp during functional tasks*, Journal of Medical Engineering and Technology **25** (2001), no. 5, 207–211.

[JDW03] S. J. Julier and H. F. Durrant-Whyte, *On the role of process models in autonomous land vehicle navigation systems*, IEEE Transactions on Robotics and Automation **19** (2003), no. 1, 1–14.

[JU97] S. J. Julier and J. K. Uhlmann, *A new extension of the kalman filter to nonlinear systems*, Proc. of the SPIE **3068** (1997), 182–193.

[JUDW00] S. Julier, J. Uhlmann, and H. F. Durrant-Whyte, *New method for the nonlinear transformation of means and covariances in filters and estimators*, IEEE Transactions on Automatic Control **45** (2000), no. 3, 477–482.

[Kal60] R. E. Kalman, *A new approach to linear filtering and prediction problems*, Transactions of the ASME – Journal of Basic Engineering **82** (1960), no. Series D, 35–45.

[KAS99] H. Kimura, S. Akiyama, and K. Sakurama, *Realization of dynamic walking and running of the quadruped using neural oscillator*, Autonomous Robots **7** (1999), no. 3, 247–258.

[KBI99] M. Koifman and I. Y. Bar-Itzhack, *Inertial navigation system aided by aircraft dynamics*, IEEE transactions on Control Systems Technology **7** (1999), no. 4, 487–493.

[KCC04] S. Kim, J. E. Clark, and M. R. Cutkosky, *isprawl : Autonomy, and the effects of power transmission*, Proc. of the 7th International Conference on Climbing and Walking Robots, Madrid, Spain, 2004.

[KFK01] H. Kimura, Y. Fukuoka, and K. Konaga, *Adaptive dyanmic walking of a qqadruped robot by using neural system model*, Advanced Robotics **15** (2001), no. 8, 859–878.

[KIJ01] D. C. Kar, K. K. Issac, and K. Jayarajan, *Minimum energy force distribution for a walking robot*, Journal of Robotic Systems **18** (2001), no. 2, 47–54.

[KLSK01] B. Klaassen, R. Linnemann, D. Spenneberg, and F. Kirchner, *Biomimetic walking robot scorpion: Control and modelling*, Proc. of the International Symposium on Intelligent Robotic Systems, 2001.

[KMS$^+$01] H. Komsuoglu, D. McMordie, U. Saranli, N. Moore, M. Buehler, and D. E. Koditschek, *Proprioception based behavioral advances in a hexapod robot*, Proc. of the IEEE International Conference on Robotics and Automation, Seoul, Korea (Seoul, Korea), vol. 4, May 2001, pp. 3650–3655.

[Kni97] D. T. Knight, *Rapid development of tightly-coupled gps/ins systems*, IEEE AES Systems Magazine **12** (1997), no. 2, 14–18.

[Kom05] H. Komsuoglu, *Legnet - a distributed wireless network*, Tech. report, The University of Michigan, 2005, In preparation.

[KQR03] D. A. Kingsley, R. D. Quinn, and R. E. Ritzmann, *A cockroach inspired robot with artificial muscles*, Proc. of the International Symposium on Adaptive Motion of Animals and Machines (Kyoto, Japan), Mar 2003.

[KS92] E. Krotkov and R. Simmons, *Performance of a six-legged plantary rover power, positioning, and autonomous walking*, Proc. of the IEEE International Conference on Robotics and Automation, Nice, France, 1992, pp. 169–174.

[KT94] M. Kaneko and K. Tanie, *Contact point detection for grasping an unknown object using self-posture changeability*, IEEE Transactions on Robotics and Automation **10** (1994), no. 3, 355–367.

[KZK97] M. Kam, X. Zhu, and P. Kalata, *Sensor fusion for mobile robot navigation*, Proc. IEEE **85** (1997), no. 1, 108–119.

[LD98] J. Lobo and J. Dias, *Integration of inertial information with vision*, Proc. of the IEEE Annual Conference on Industrial Electronics Society (IECON), vol. 3, Aug 1998, pp. 1263–1267.

[LDR+99] D. M. Lane, J. B. C. Davies, G. Robinson, D. J. O'Brien, J. Sneddon, E. Seaton, and A. Elfstrom, *Amadeus dextrous subsea hand: Design, modeling, and sensor processing*, IEEE Journal of Oceanic Engineering **24** (1999), no. 1, 96–111.

[LH02] S. Lee and Y. C. Huang, *Innovative estimation method with measurement likelihood for all-accelerometer type inertial navigation system*, IEEE transactions on Aerospace and Electronic Systems **38** (2002), no. 1, 339–346.

[LHQ05] B. G. A. Lambrecht, A. D. Horchler, and R. D. Quinn, *A small, insect-inspired robot that runs and jumps*, Proc. of the IEEE International Conference on Robotics and Automation, Barcelona, Spain, Apr 2005, pp. 1252–1257.

[Lin05] P. Lin, *Benchtop setting for compliant leg test and modeling*, Tech. report, The University of Michigan, 2005, In preperation.

[LK03] G. A.D. Lopes and D. E. Koditschek, *Visual registration and navigation using planar features*, Proc. of the IEEE International Conference on Robotics and Automation, Taipei, Taiwan, vol. 3, Sep 2003, pp. 3935–3940.

[LKK03] P. Lin, H. Komsuoglu, and D. E. Koditschek, *A leg configuration sensory system for dynamical body state estimates in a hexapod robot*, Proc. of the IEEE International Conference on Robotics and Automation, Taipei, Taiwan, vol. 1, Sep 2003, pp. 1391–1396.

[LKK04] ———, *Legged odometry from body pose in a hexapod robot*, Proc. of the 9th International Symposium on Experimental Robotics, Singapore, Jun 2004, to be published.

[LKK05a] ———, *A leg configuration measurement system for full body pose estimates in a hexapod robot*, IEEE Transactions on Robotics **21** (2005), no. 3, 411–422.

[LKK05b] ———, *Sensor data fusion for body state estimation for a hexapod robot with dynamical gaits*, Proc. of the IEEE International Conference on Robotics and Automation, Barcelona, Spain, Apr 2005, pp. 4744–4749.

[LKK05c] ———, *Sensor data fusion for body state estimation in a hexapod robot with dynamical gaits*, IEEE Transactions on Robotics (2005), submitted for review.

[LL99] S. Lee and C. Liu, *An innovative estimation method with own-ship estimator for an all accelerometer-type inertial navigation system*, International Journal of Systems and Science **30** (1999), no. 12, 1259–1266.

[LOS+00] M. Lim, S. Oh, J. Son, B. You, and K. Kim, *Human-like real-time grasp synthesis method for humanoid robot hands*, Robotics and Autonomous Systems **30** (2000), no. 3, 261–271.

[LPP93] J. G. Lee, C.G. Park, and H. W. Park, *Multiposition alignment of strapdown inertial navigation system*, IEEE transactions on Aerospace and Electronic Systems **29** (1993), no. 4, 1323–1328.

[MA01] S. Mascaro and H. H. Asada, *Finger posture and shear force measurement using fingernail sensors: Initial experimentation*, Proc. of the IEEE International Conference on Robotics and Automation, Seoul, Korea, vol. 2, 2001, pp. 1857–1862.

[MAG+02] L. Moreno, J. M. Armingol, S. Garrido, A. De La Escalera, and M. A. Salichs, *A genetic algorithm for mobile robot localization using ultrasonic sensors*, Journal of Intelligent and Robotic Systems **34** (2002), no. 2, 135–154.

[Mar01a] A. Martinelli, *A possible strategy to evaluate the odometry error of a mobile robot*, Proc. of the IEEE/RSJ International Conference on Intelligent Robots and Systems, Maui, HI, vol. 4, 2001, pp. 1946–1951.

[Mar01b] E. Martinez, *Qualitative vision for the guidance of legged robots in unstructured environments*, Pattern Recognition **34** (2001), no. 8, 1585–1599.

[Mar02] A. Martinelli, *The odometry error of a mobile robot with a synchronous drive system*, IEEE Transactions on Robotics and Automation **18** (2002), no. 3, 399–405.

[May79] P. S. Maybeck, *Stochastic models, estimation and control, vol. 1 of mathematics in science and engineerin*, Academic Press, 1979.

[MB01] D. McMordie and M. Buehler, *Towards pronking with a hexapod robot*, Proc. of the 4th International Conference on Climbing and Walking Robots, Karlsruhe, Germany, Sep 2001, pp. 659–666.

[MCGB02] E. Z. Moore, D. Campbell, F. Grimminger, and M. Buehler, *Reliable stair climbing in the simple hexapod 'RHex'*, Proc. of the IEEE International Conference on Robotics and Automation, Washington, D.C., vol. 3, May 2002, pp. 2222–2227.

[MED98] I. M. Mandour and M. M. El-Dakiky, *Inertial navigation system synthesis approach and gravity-induced error sensitivity*, IEEE transactions on Aerospace and Electronic Systems **24** (1998), no. 1, 40–50.

[MHJ94] J. Meyer-Hilberg and T. Jacob, *High accuracy navigation and landing system using gps/imu system integration*, IEEE AES Systems Magazine **9** (1994), no. 7, 11–17.

[MK79] N. K. Mital and A. I. King, *Computation of rigid-body rotation in three-dimensional space from body-fixed linear acceleration measurement*, Transactions of the ASME **46** (1979), no. 4, 925–930.

[MKS99] Y. Ma, J. Kosecka, and S. S. Sastry, *Vision guided navigation for a non-holonomic mobile robot*, IEEE Transactions on Robotics and Automation **15** (1999), no. 3, 521–536.

[MMAI01] Y. Mae, T. Masuda, T Arai, and K. Inoue, *Error analysis of dead reckoning of multi-legged robots*, Proc. of the IEEE/RSJ International Conference on Intelligent Robots and Systems, Maui, HI, vol. 3, Oct 2001, pp. 1558–1563.

[MMB01] E. Z. Moore and r M. Buehle, *Stable stair climbing in a simple hexapod*, Proc. of the 4th International Conference on Climbing and Walking Robots, Karlsruhe, Germany, Sep 2001, pp. 603–610.

[Moo01] E. Z. Moore, *Leg design and stair climbing control for the RHex robotic hexapod*, Master's thesis, McGill University, Nov 2001.

[MSDW01] S. Majumder, S. Scheding, and H. F. Durrant-Whyte, *Multisensor data fusion for underwater navigation*, Robotics and Autonomous Systems **35** (2001), no. 2, 97–108.

[Muy57] E. Muybridge, *Animals in motion*, Dover Publications, 1957.

[MV98] M. K. Martin and D. A. Vause, *New low cost avionics with ins/gps for a variety of vehicles*, IEEE AES Systems Magazine **13** (1998), no. 11, 41–47.

[NB03] N. Neville and M. Buehler, *Towards bipedal running of a six legged robot*, 12th Yale Workshop on Adaptive and Learning Systems, May 2003.

[NBDW99] E. M. Nebot, M. Bozorq, and H. F. Durrant-Whyte, *Decentralized architecture for asynchronous sensors*, Autonomous Robots **6** (1999), no. 2, 147–164.

[NDW99a] E. Nebot and H. F. Durrant-Whyte, *Initial calibration and alignment of low-cost inertial navigation units for land vehicle applications*, Journal of Robotic Systems **16** (1999), no. 2, 81–92.

[NDW99b] E. M. Nebot and H. F. Durrant-Whyte, *A high integrity navigation architecture for outdoor autonomous vehicles*, Robotics and Autonomous Systems **26** (1999), no. 2-3, 81–97.

[NMK+02] K. Nishiwaki, Y. Murakami, S. Kagami, Y. Kuniyoshi, M. Inaba, and H. Inoue, *A six-axis force sensor with parallel support mechanism to measure the ground reaction force of humanoid robot*, Proc. of the IEEE International Conference on Robotics and Automation, Washington, D.C., vol. 3, 2002, pp. 2277–2282.

[NQ98] G. M. Nelson and R. D. Quinn, *Posture control of a cockroach-like robot*, Proc. of the IEEE International Conference on Robotics and Automation, Leuven, Belgium, vol. 1, 1998, pp. 157–162.

[NQ99] ______, *Posture control of a cockroach-like robot*, IEEE Control Systems Magazine **19** (1999), no. 2, 9–14.

[NQB$^+$97] G. M. Nelson, R. D. Quinn, R. J. Bachmann, W. C. Flannigan, R. E. Ritzmann, and J. T. Watson, *Design and simulation of a cockroach-like hexapod robot*, Proc. of the IEEE International Conference on Robotics and Automation, Albuquerque, NM, vol. 2, 1997, pp. 1106–1111.

[OIYH98] Y. Ota, Y. Inagaki, K. Yoneda, and S. Hirose, *Research on a six-legged walking robot with parallel mechanism*, Proc. of the IEEE/RSJ International Conference on Intelligent Robots and Systems, Victoria, B.C., Canada, Oct 1998, pp. 241–248.

[OV98] S. J. Ovaska and S. Valiviita, *Angular acceleration measurement: A review*, IEEE transactions on Instrumentation and Measurement **47** (1998), no. 5, 1211–1217.

[Pau83] R. P. Paul, *Robot manipulators - mathematics, programming, and control*, The MIT Press, 1983.

[PB00] D. Papadopoulos and M. Buehler, *Stable running in a quadruped robot with compliant legs*, Proc. of the IEEE International Conference on Robotics and Automation, San Francisco, CA, 2000, pp. 444–449.

[PCCL97] K. Park, H. Chung, J. Choi, and J. G. Lee, *Dead reckoning navigation for an autonomous mobile robot using a differential encoder and a gyroscope*, Proc. of the IEEE International Conference on Robotics and Automation, Albuquerque, NM, 1997, pp. 441–446.

[PKK75] A. J. Padgaonkar, K. W. Krieger, and A. I. King, *Measurement of angular accelerarion of a rigid body using linear accelerometers*, Transactions of the ASME **42** (1975), 552–556.

[PPU02] S. Panzieri, F. Pascucci, and G. Ulivi, *An outdoor navigation system using gps and inertial platform*, IEEE/ASME transactions on Mechatronics **7** (2002), no. 2, 134–142.

[PRS01] S. H. Phang, R. C. Ren, and K. L. Su, *The development of intelligent control system for animal robot using multisensor fusion*, Proc. of the IEEE International Conference on Multisensor Fusion and Integration for Intelligent Systems, 2001, pp. 1–6.

[PSB03] I. Poulakakis, J.A. Smith, and M. Buehler, *On the dynamics of bounding and extensions towards the half-bound and the gallop gaits*, Proc. of the International Symposium on Adaptive Motion of Animals and Machines, 2003.

[PSB04] I. Poulakakis, J. A. Smith, and M. Buehler, *Experimentally validated bounding models for the scout ii quadrupedal robot*, Proc. of the IEEE International Conference on Robotics and Automation, New Orleans, LA, Apr 2004, pp. 2595–2600.

[QNB01a] R. D. Quinn, G. M. Nelson, and R. J. Bachmann, *Toward mission capable legged robots through biological inspiration*, Autonomous Robots **11** (2001), no. 3, 215–220.

[QNB+01b] R. D. Quinn, G. M. Nelson, R. J. Bachmann, D. A. Kingsley, J. Offi, and R. E. Ritzmann, *Insect designs for improved robot mobility*, Proc. of the 4th International Conference on Climbing and Walking Robots, Karlsruhe, Germany, 2001.

[QNB+03] R. D. Quinn, G. M. Nelson, R. J. Bachmann, D. A. Kingsley, J. T. Offi, and T. J. Allen, *Parallel complementary strategies for implementing biological principles into mobile robots*, The International Journal of Robotics Research **22** (2003), no. 3, 169–186.

[Rai00] M. Raibert, *Legged robots that balance*, MIT Press, 2000.

[RB02] S. I. Roumeliotis and J. W. Burdick, *Stochastic cloning: A general framework for processing relative state measurements*, Proc. of the IEEE International Conference on Robotics and Automation, Washington, D.C., vol. 2, 2002, pp. 1788–1795.

[RH00] H. Rehbinder and X. Hu, *Nonlinear pitch and roll estimation for walking robots*, Proc. of the IEEE International Conference on Robotics and Automation, San Francisco, CA, vol. 3, 2000, pp. 2617–2622.

[RH04] ______, *Drift-free attitude estimation for accelerated rigid bodies*, Automatica **40** (2004), no. 4, 653–659.

[RI01] C. Ridderstrom and J. Ingvast, *Quadruped posture control based on simple force distribution - a notion and trial*, Proc. of the IEEE/RSJ International Conference on Intelligent Robots and Systems, Maui, HI, vol. 4, 2001, pp. 2326–2331.

[RJM02] S. I. Roumeliotis, A. E. Johnson, and J. F. Montgomery, *Augmenting inertial navigation with image-based motion estimation*, Proc. of the IEEE International Conference on Robotics and Automation, Washington, D.C., 2002.

[RPS01] R. C. Ren, S. H. Phang, and K. L. Su, *Multilevel multisensor based decision fusion for intelligent animal robot*, Proc. of the IEEE International Conference on Robotics and Automation, Seoul, Korea, vol. 4, May 2001.

[RSB99] S. I. Roumeliotis, G. S. Sukhatme, and G. A. Bekey, *Circumventing dynamic modeling: Evaluation of the error-state kalman filter applied to mobile robot localization*, Proc. of the IEEE International Conference on Robotics and Automation, Detroit, MI, vol. 2, 1999, pp. 1656–1663.

[Rud03] A. Rudolph, *Quantification and estimation of differential odometry errors in mobile robotics with redundant sensor information*, The International Journal of Robotics Research **22** (2003), no. 2, 117–128.

[RV90] B. A. Roberts and L. C. Vallot, *Vision-aided inertial navigation*, Proc. of the IEEE Position Location and Navigation Symposium (PLANS), Mar 1990, pp. 347–352.

[Sar02] U. Saranli, *Dynamic locomotion in a hexapod robot*, Ph.D. thesis, The University of Michigan, 2002.

[SBK01] U. Saranli, M. Buehler, and D. E. Koditschek, *RHex - a simple and highly mobile hexapod robot*, The International Journal of Robotics Research **20** (2001), no. 7, 616–631.

[SDNDW99] S. Scheding, G. Dissanayake, E. M. Nebot, and H. F. Durrant-Whyte, *An experiment in autonomous navigation of an underground mining vehicle*, IEEE Transactions on Robotics and Automation **15** (1999), no. 1, 85–95.

[SGG+00] S. Sukkarieh, P. Gibbens, B. Grocholsky, K. Willis, and H. F. Durrant-Whyte, *A low-cost, redundant inertial measurement unit for unmanned air vehicles*, The International Journal of Robotics Research **19** (2000), no. 11, 1089–1103.

[Sha03] G. Sharp, *Ground truth measurement system*, Tech. report, The University of Michigan, 2003, http://sourceforge.net/projects/gtms/.

[SHM97] B. M. Scherzinger, J. J. Hutton, and J. C. McMillan, *Low cost inertial/gps integrated position and orientation system fot marine application*, IEEE AES Systems Magazine **12** (1997), no. 5, 15–19.

[SK00] D. Spenneberg and F. Kirchner, *Omnidirectional walking in an eight legged robot*, Proc. Int. Symp. Robotics and Automation, 2000.

[SK02] U. Saranli and D. E. Koditschek, *Back flips with a hexapodal robot*, Proc. of the IEEE International Conference on Robotics and Automation, Washington, D.C., vol. 3, May 2002, pp. 2209–2215.

[SK03] ———, *Template based control of hexapedal running*, Proc. of the IEEE International Conference on Robotics and Automation, Taipei, Taiwan, vol. 1, Sep 2003, pp. 1374–1379.

[SKMR03] S. Skaff, G. A. Kantor, D. Maiwand, and A. Rizzi, *Inertial navigation and visual line following for a dynamical hexapod robot*, Proc. of the IEEE/RSJ International Conference on Intelligent Robots and Systems, Las Vegas, NV, vol. 2, Oct 2003.

[SNDW99] S. Sukkarieh, E. M. Nebot, and H. F. Durrant-Whyte, *A high integrity imu/gps navigation loop for autonomous land vehicle application*, IEEE Trans. Robot. Automat. **15** (1999), no. 3, 572–578.

[SNDW00] S. Scheding, E. Nebot, and H. Durrant-Whyte, *High-integrity navigation: A frequency-domain approach*, IEEE transactions on Control Systems Technology **8** (2000), no. 4, 676–694.

[SP04] J. A. Smith and I. Poulakakis, *Rotary gallop in the untethered quadrupedal robot scout ii*, Proc. of the IEEE/RSJ International Conference on Intelligent Robots and Systems, Sendai, Japan, vol. 3, Sep 2004, pp. 2556–2561.

[SRCL05] S. Skaff, A. Rizzi, H. Choset, and P. Lin, *Context-based state estimation technique for hybrid systems*, Proc. of the IEEE International Conference on Robotics and Automation, Barcelona, Spain, Apr 2005, pp. 3935–3940.

[SRK04] U. Saranli, A. Rizzi, and D.E. Koditschek, *Model-based dynamic self-righting maneuvers for a hexapedal robot*, The International Journal of Robotics Research **23** (2004), no. 9, 903–918.

[SS01] S. Shoval and M. Shoham, *Sensory redundant parallel mobile mechanism*, Proc. of the IEEE International Conference on Robotics and Automation, Seoul, Korea, May 2001, pp. 2273–2278.

[SW99] J. Z. Sasiadek and Q. Wang, *Sensor fusion based on fuzzy kalman filtering for autonomous robot vehicle*, Proc. of the IEEE International Conference on Robotics and Automation, Detroit, MI, vol. 4, 1999, pp. 2970–2975.

[SW03] ———, *Low cost automation using ins/gps data fusion for accurate positioning*, Robotica **21** (2003), no. 3, 255–260.

[Tau00] G. Taubes, *Biologists and engineers create a new generation of robots that imitate life*, Science **288** (2000), no. 5463, 80.

[TPMV01] C. Tan, S. Park, K. Mostov, and P. Varaiya, *Design of gyroscope-free navigation systems*, International Conference on Intelligent Transportation Systems, 2001, pp. 286–291.

[WC00] O. Wijk and H. I. Christensen, *Triangulation-based fusion of sonar data with application in robot pose tracking*, IEEE Transactions on Robotics and Automation **16** (2000), no. 6, 740–752.

[Wei96] J. D. Weiss, *Analysis of an upgraded gps internal kalman filter*, IEEE AES Systems Magazine **11** (1996), no. 1, 23–26.

[WGK04] J. D. Weingarten, Richard E. Groff, and D. E. Koditschek, *A framework for the coordination of legged robot gaits*, Proc. of the IEEE International Conference on Robotics, Automation, and Mechatronics, Singapore, Dec 2004, pp. 679–686.

[WLK04] J. D. Weingarten, G. A.D. Lopes, and D. E. Koditschek, *Automated gait generation and optimization for legged robots*, Proc. of the IEEE International Conference on Robotics and Automation, New Orleans, LA, vol. 3, May 2004, pp. 2153–2158.

[WT00] J. L. Weston and D. H. Titterton, *Modern inertial navigation technology and its application*, Electronics and Communication Engineering Journal (2000), 49–64.

[YBA+01] X. Yun, E. R. Bachmann, S. Arslan, K. Akyol, and R. B. McGhee, *An inertial navigation system for small autonomous underwater vehicles*, Advanced Robotics **15** (2001), no. 5, 521–532.

[YIT03] Y. Yu, T. Ishitsuka, and S. Tsujio, *Torque sensing of finger joint using strain-deformation expansion mechanism*, Proc. of the IEEE International Conference on Robotics and Automation, Taipei, Taiwan, vol. 2, 2003, pp. 1850–1856.

[ZFhK04] Z. G. Zhang, Y. Fukuoka, and h. Kimura, *Stable quadrupedal running based on a spring-loaded two-segment legged model*, Proc. of the IEEE International Conference on Robotics and Automation, New Orleans, LA, vol. 3, Apr 2004, pp. 2601–2606.

[ZFhK05] ———, *Adaptive running of a quadruped robot using delayed feedback control*, Proc. of the IEEE International Conference on Robotics and Automation, Barcelona, Spain, Apr 2005, pp. 3750–3755.